Photocopy and Use Authorization

In presenting this thesis in partial fulfillment of the requirements for an advanced degree at Idaho State University, I agree that the Library shall make it freely available for inspection. I further state that permission for extensive copying of my thesis for scholarly purposes may be granted by the Dean of the Graduate School, Dean of my academic division, or by the University Librarian. It is understood that any copying or publication of this thesis for financial gain shall not be allowed without my written permission.

Signature _____

Date _____

Nonlinear Finite Element Modeling of a Field-Cast Connection Composed of High-Early Strength Concrete with Polypropylene Fibers and Headed Bars for Bridge Prefabricated Elements

by

Utsa Rashique

A thesis

submitted in partial fulfillment

of the requirements for the degree of

Master of Science in the Department of Civil and Environmental Engineering

Idaho State University

Spring 2019

Committee Approval

To the Graduate Faculty:

The members of the committee appointed to examine the thesis of UTSA RASHIQUE find it satisfactory and recommend that it be accepted.

_____

Dr. Arya Ebrahimpour

Major Advisor

_____

Dr. Mustafa Mashal

Committee Member

_____

Dr. Donna Delparte

Graduate Faculty Representative

Acknowledgment

Firstly, I would like to express my gratitude to my thesis supervisor Dr. Arya Ebrahimpour, who helped me immensely in every step along the way. Without his patience, guidance, and knowledge, I could not have done this. I am also grateful to my co-supervisor Dr. Mustafa Mashal for his vital support, insights, and encouragement. I thank both of them for expecting nothing less than excellence from me.

I would also like to thank David Unobe and Christopher Clauson for their help in various stages of the project. I am also thankful to my fellow students who provided their feedback and cooperation from time to time.

I am grateful to the Idaho Transportation Department for funding this project. However, the contents of this thesis reflect the views of the author, who is responsible for the facts and accuracy of the data presented herein. The contents do not necessarily reflect the official views or policies of the Idaho Transportation Department or the Federal Highway Administration. This thesis does not constitute a standard, specification, or regulation.

Last but not the least, I could not have done this without my parents, who encourage and motivate me every day from the other side of the ocean, eight thousand miles away, to follow my dreams.

Table of Content

List of Figures

List of Tables

Nonlinear Finite Element Modeling of a Field-Cast Connection Composed of High-Early Strength Concrete with Polypropylene Fibers and Headed Bars for Bridge Prefabricated Elements

Thesis Abstract – Idaho State University (2019)

An alternative mix design using polypropylene fiber-reinforced High Early Strength (HES) concrete was proposed by the Idaho Transportation Department (ITD) for connection between precast bridge girders in Accelerated Bridge Construction (ABC). In this thesis, finite element models of the pullout behavior of headed reinforcing bars in the closure pour and bending tests of beams representing a 1-foot strip of the bridge deck were developed. The "smeared crack" along with the William-Warnke failure criteria was used for concrete, while Cohesive Zone Modeling (CZM) showed good results in representing the interface between the closure pour and precast concrete. Steel-concrete bond-slip behavior was observed to be one of the biggest factors affecting the results. A scheme to simulate this behavior using zero-length nonlinear spring elements was designed. The finite element models were able to produce results similar to the experimental findings, especially in the linear region.

Key Words: Bridge, deck, connections, precast elements, accelerated bridge construction, ABC, finite element modeling, nonlinear.

Chapter 1: Introduction

1.1 Preamble

Accelerated Bridge Construction (ABC), a relatively new method in the U.S.A, has been undergoing an accelerated advancement in terms of implementation. This advancement has been facilitated by the various research projects initiated by the State Departments of Transportation (DOTs). The DOTs have developed their own standards and guidelines for ABC. One particular area of interest in ABC is the connection design between the precast bridge elements. Currently, the most popular option for the closure pour material in the connection between two neighboring precast deck elements is Ultra High-Performance Concrete (UHPC). Although UHPC is an excellent material in terms of strength (compressive strength reaching up to 30 ksi), it is a proprietary material with some other disadvantages like high installation cost, rigorous quality control requirements, fast setting time and being more labor-intensive (Ebrahimpour et al. 2018). As an alternative, the Idaho Transportation Department is proposing the use of High Early Strength (HES) concrete reinforced with polypropylene fibers as the closure pour material between the girders. This study is a part of the project to investigate the proposed closure pour material, which specifically focuses on the development of Finite Element models based on experimental studies.

1.2 Problem Statement

There have been several experimental tests showing that precast bridge deck panels or girders may be effectively connected by placing UHPC in 6 inches wide closure pours between the precast elements. UHPC allows full strength development of #6 bars extended from precast elements into the narrow 6 inches closure pours. Casanova 2018 tested polypropylene fiber-reinforced HES in 10 inches closure pour between precast girders. Casanova 2018 used #5 headed rebars protruding out from the precast elements. A typical closure pour section between

two girders, and the reinforcing details in one girder proposed by the ITD are shown in Figure 1.1.

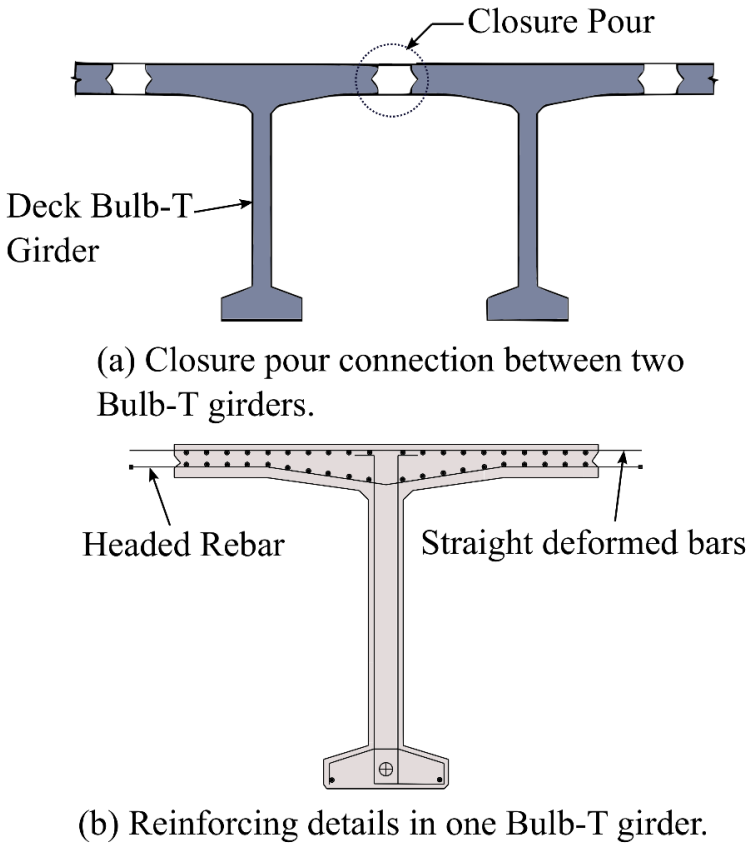

Figure 1.1: Example of closure pour between deck bulb-T girders with reinforcing details.

The purpose of this thesis is to develop finite element models based on the experimental data obtained using the optimum HES concrete mix developed by Casanova 2018. Finite element models will be developed to study the behavior of the proposed design to study its performance in element level and assembly level.

1.3 Objectives and Deliverables

The objectives and deliverable for this study are:

- Study the pullout behavior of #5 headed rebars embedded in the proposed concrete connection design. A finite element model will be developed based on the pullout tests and validated using the results obtained from the experiments.
- Investigate the cracking moment and the ultimate strength of a beam representing a 1-foot strip of the bridge deck that includes the proposed closure pour connection details. Finite elements models will be developed for the beams and validated using the results of three-point and four-point bending test results.

1.4 Thesis Outline

This thesis is divided into 6 chapters.

- **Chapter 1** gives a brief outline of the problem statement and the objectives.
- **Chapter 2** contains the literature review of experimental studies on concrete connections and bond-slip behavior of rebars in concrete
- **Chapter 3** contains the literature review and background information on finite element modeling of concrete and bond-slip behavior of rebars in concrete.
- **Chapter 4** describes the methodology used in developing the models for the pullout test, and the beam bending tests.
- **Chapter 5** discusses the results obtained from the models developed in chapter 4.
- **Chapter 6** presents the summary, conclusion and recommendations based on the results discussed in chapter 5.

Furthermore, this thesis contains 4 appendices.

- **Appendix A** describes a verification scheme for the concrete model used in the finite element models.
- **Appendix B** contains the verification of the techniques used for modeling the concrete-concrete bonds and the bond-slip phenomenon between steel and concrete.

- **Appendix C** describes the procedure for preparing the 3D model of the flexural beam tests to be used in the FE modeling using Onshape- a cloud-based 3D CAD program.
- **Appendix D** contains detailed step-by-step procedures for the development of the finite element models for the 3-point and 4-point flexural beam tests.

Chapter 2: Experimental Background

2.1 Introduction

Reinforced concrete construction is mostly based on the assumption that steel and concrete are perfectly bonded together. However, the issue with the steel-concrete bond has been identified and has been extensively researched since the nineteenth century. As a result, deformed, bent, twisted and headed bars were introduced for better bond strength. These geometric variations resulted in complicated bond analyses. With the introduction of newer construction materials like FRP bars, fiber reinforced concrete and alkali activated concrete variations in the bond strength were observed. Many other parameters like mix proportion, bar spacing, casting direction, concrete cover and concrete confinement also play significant roles in bond strength. Much research over the variation of bond strength with the change of these parameters has been conducted over the years. In this chapter, prior studies on steel-concrete bond mechanism will be explored. Studies on cast-in-place concrete connections will also be reviewed. A suitable cast-in-place concrete connection method that can draw a balance between serviceability and cost-efficiency, is a key component to achieve the maximum benefit of the Accelerated Bridge Construction (ABC) method. The advancement of ABC implementation in the US has been experiencing a significant acceleration in recent years. Finally, this chapter will briefly describe the experimental procedures performed by Casanova 2018. Most of this study is based on these experiments and the obtained results.

2.2 Literature Review

In this study, two types of bond play important roles. Firstly, the bond between steel rebars and concrete. The second type of bond is the interface bond between the closure pour and the

precast concrete. Numerous studies have been carried out to determine the nature and importance of these two types of bonds in reinforced concrete structures.

2.2.1 Steel- Concrete Bond Mechanism

A simple definition of bond is the transfer of stress between steel and concrete. This transfer has three components (Lutz and Gergely 1967):

1. Chemical adhesion,
2. Friction,
3. Mechanical interlocking between concrete and steel.

The bond in plain bars is mainly dependent on the first two components. Deformed bars primarily depend on mechanical interlocking. However, the effect of the other two factors is not absent in deformed bars.

2.2.1.1 Bond in Plain Bars

Although many concrete structures were constructed with plain reinforcing bars before the 1970s (Hertanto 2005), the majority of the literature deal with deformed bars. The data on the anchorage and pullout behavior of plain bars are not adequate.

Plain bars do not have ribs or any surface irregularity. Therefore, bond force cannot be transferred through mechanical interlocking. Abrams 1913, found that chemical adhesion and friction do not act simultaneously on a given point. The adhesive resistance has to be overcome before the sliding resistance becomes effective. According to Abrams 1913, the irregularities on the bar surface, section and alignment, and the wedging action of small particles that break free from the concrete upon slip.

Feldman and Bartlett 2005, studied a total of 252 pullout specimens with plain reinforcing bars and investigated various parameters like concrete compressive strength, bar size, bar shape,

concrete cover and bar surface roughness. The coefficient of variation of maximum average bond stress normalized by the square root of the concrete compressive strength decreases with increasing embedment length and bar roughness but has no correlation with concrete cover or bar size.

Xing et al. 2015, studied the comparative bond behavior in pullout specimens with plain and deformed bars. Adhesive stress was found to be about 2 to 5% of the total bond stress in deformed bars, while 11% of the bond stress in plain bars were attributed to adhesion. Figure 2.1 shows the components of bond strengths in plain and deformed bars where *x* represents the percentage contribution due to adhesion force.

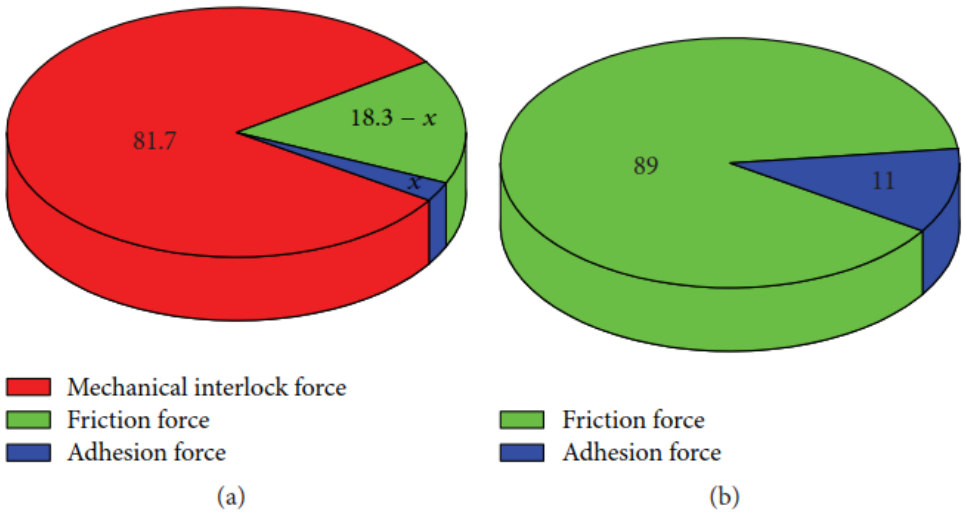

Figure 2.1: Components of bond strength in (a) deformed bar and (b) plain bar (Xing et al. 2015).

2.2.1.2 Bond in Deformed Bars

In comparison to plain bars, the literature related to the study of anchorage and pullout behavior of deformed bars is abounding. Many studies have been conducted to investigate the bond response mechanism of deformed bars in concrete in the scales of the structural elements, the reinforcement, and the reinforcement ribs. In addition to the bar geometry, other parameters like the concrete constitution, loading pattern, embedment length, concrete confinement etc.

were also thoroughly studied. Mathey and Watstein 1961, conducted experiments on 18 beams and 18 pullout specimens with deformed reinforcing bars and reported that the bond strength, expressed as force per unit bar surface area, decreases with the increase of embedment length. The bond strength also decreases with the increase of bar diameter. Bond stress was defined by Equation (2.1):

Where,

$$u = \frac{f_s A_s}{\Sigma_0 L} \qquad (2.1)$$

u = bond stress,

f_s = bar stress computed by straight line theory,

A_s = cross-sectional area of the bar,

Σ_0 = bar perimeter,

L = embedment length.

The maximum bond stress, u_m, corresponding to the maximum bar stress calculated, indicates a nearly complete state of collapse i.e., no bond between steel and concrete. The critical bond stress, u_c, corresponds to the condition that indicates an impending bond failure. A measurement of both the slips at the loaded and the free end showed that a loaded-end slip alone cannot indicate the impending bond failure in a beam. Therefore, Mathey and Watstein 1961, used two criteria to define critical bond stress: a loaded-end slip of 0.01 inch and a free-end slip of 0.002 inch, whichever occurs first. A linear relationship between the critical bond stresses and the ratio of the bar diameter to length of embedment was observed. Equation (2.1) can be rearranged as $u = (f_s \pi D^2)/(4\pi DL)$. Thus, in Figure 2.2, $u_c/(f_s)_c$ is equal to $D/4L$, where *D*= bar diameter and *L*= embedment length. Also, the adjusted values of u_c is obtained

by multiplying the observed values by the factor $\bar{f}_c'/f_c'$ where $\bar{f}_c'$ is the average value obtained for each group of specimens containing bars of a given size.

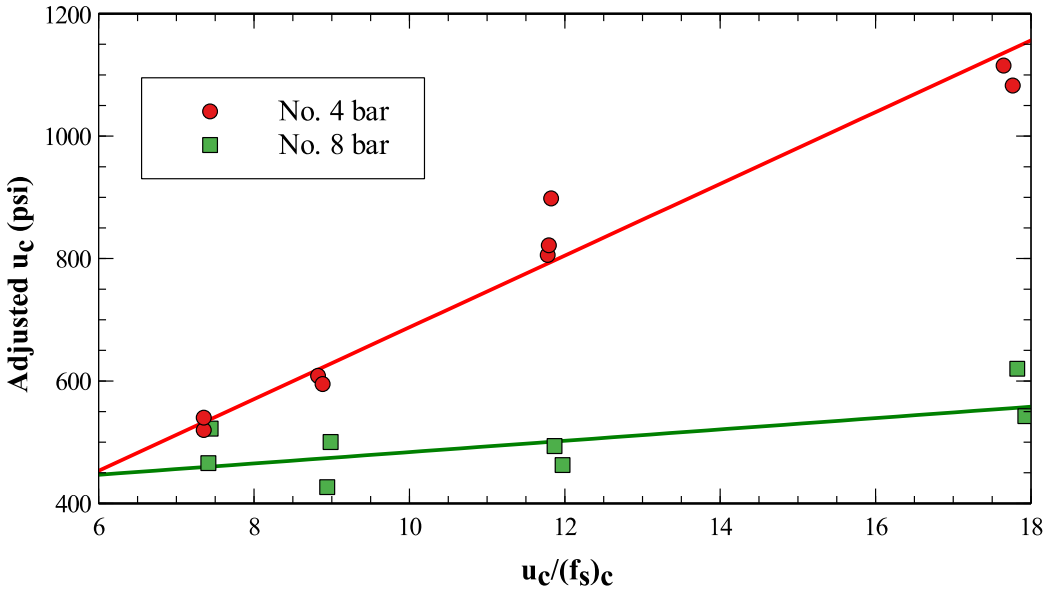

Figure 2.2: Adjusted critical bond stress, u_c vs the ratio $u_c/(f_s)_c$ for beams, where $(f_s)_c$ is the stress in the reinforcing bar (Mathey and Watstein 1961)

Lutz and Gergely 1967, reported that, if the rib face angle of the reinforcing bar is greater than 40°, the slip occurs almost entirely due to crushing of the concrete in front of the ribs. On the other hand, when the rib face angle is less than 30°, the slip is due primarily to the relative movement between concrete and steel along the face of the rib, where the rib pushes the concrete away from the bar (wedging action). After the formation of surface flexural cracks, a separation of bar and concrete occurs near the vicinity of a crack. While this separation results in a complete loss of bond in the case of plain bars (Mathey and Watstein 1961), the ribs in a deformed bar prevent much of the crack opening near the bar. Thus, a large variation in crack width from bar to surface is observed in deformed bars (Lutz and Gergely 1967) as shown in Figure 2.3.

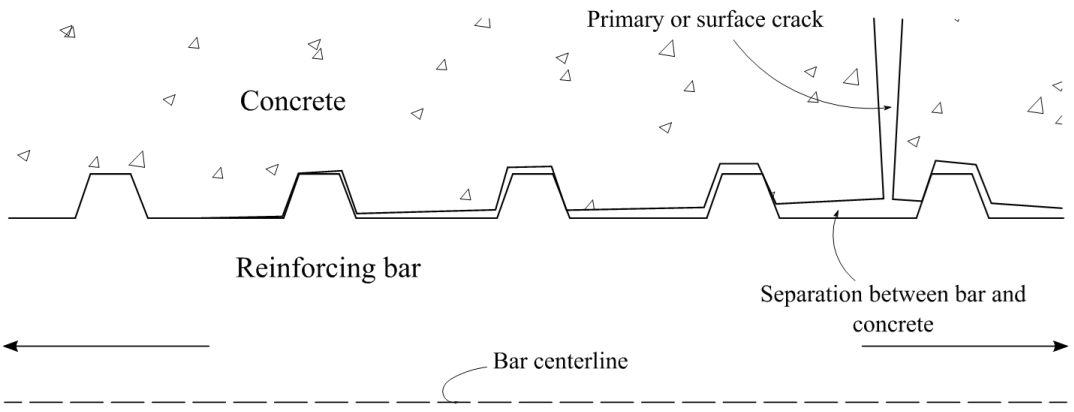

Figure 2.3: Section through reinforcing bar and concrete showing separation that occurs near a primary crack (Lutz and Gergely 1967)

At a high level of stress, internal cracks around the deformed bar form besides external flexural cracks. These internal cracks also influence and define the bond mechanism between concrete and bar. Goto 1971, studied the internal cracks by injecting ink into the tension specimens in axially-loaded tests. The internal cracks form near the lugs and approach the nearest primary crack by compressive forces transferred by the bar lugs, at an angle of about 60° with the bar axis. This inclination of the internal cracks tightens the concrete around the bar and thus increases the friction between the concrete and the deformed bar (Figure 2.4).

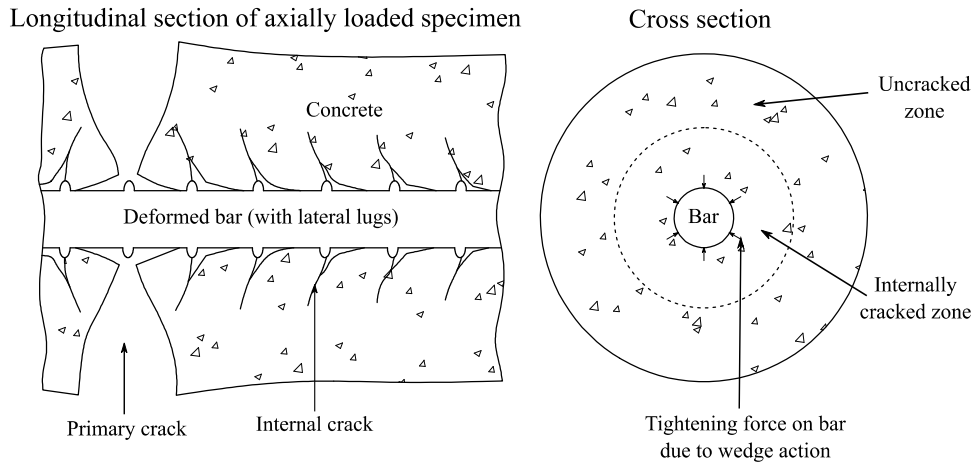

Figure 2.4: Internal cracks around the reinforcing bar embedded in concrete (Goto 1971)

For the constant moment region between two flexural cracks in a beam, the average unit bond stress (in units of shear force per unit interface area) is given by Equations (2.2) and (2.3).

$$u = \frac{dT}{\Sigma_0 dx} \tag{2.2}$$

Or,

$$u = \frac{A_s df_s}{\Sigma_0 dx} \tag{2.3}$$

Where,

$u =$ average bond stress at a location,

$dT =$ change in bar tension over the length of dx,

$\Sigma_0 =$ bar perimeter,

$A_s =$ cross-sectional area of the bar,

$df_s =$ change in steel tensile stress over the length of dx

Equation (2.3) can be expressed as:

$$u = \frac{A_s E_s}{\Sigma_0} \frac{d\varepsilon_s}{dx} \tag{2.4}$$

Where, E_s= elastic modulus of steel and $d\varepsilon_s$= steel strain corresponding to a change of bar stress equal to df_s. Thus, bond stress at a particular point for a given load is proportional to the

slope of the steel strain curve at that point. Nilson 1972, from there, proposed a displacement function for steel and concrete with respect to a reference plane of known slip.

$$S_b = S_a + \int_a^b \varepsilon_s dx - \int_a^b \varepsilon_c dx \qquad (2.5)$$

Where,

S_a = known slip at point a,

S_b = desired slip at point b,

ε_s = steel strain,

ε_c = concrete strain.

From the works of Lutz and Gergely 1967 and Goto 1971, Tepfers 1979, showed that the radial components of the bond forces are balanced against rings of tensile stress in the concrete. According to the model proposed by Tepfers, the concrete surrounding a single reinforcing bar is characterized as a thick-walled cylinder subjected to internal pressure and shear. The internal shear and pressure correspond to the bond and radial stresses developed at the bar-concrete interface respectively. Thus, the transfer of radial force at the bond determines the tensile hoop stress in the concrete surrounding the bar. The critical load is hereby controlled by the capacity of the concrete to carry the hoop stress.

To sum up, the ribs of the bar can split the concrete without crushing it when the resistance of the surrounding concrete is moderate. For example, in the case of ordinary concrete cover. This statement is also true for high-strength concrete, as confirmed by Rao et al. 2007. They tested forty pullout specimens for bond strength and its variation. It was observed that ideal pullout failure occurred in all the specimens with confinement (Figure 2.5a), while the unconfined

specimens failed by longitudinal splitting of concrete (Figure 2.5b). In the case of unconfined specimens, the failure was caused by the formation of a concrete cone from the concrete block due to bond forces acting on the concrete in front of rebar lugs. Splitting cracks developed in confined specimens, but their growth was impeded by the confinement. The maximum bond strength of unconfined concrete was found to be between 50% and 60% of that with confinement.

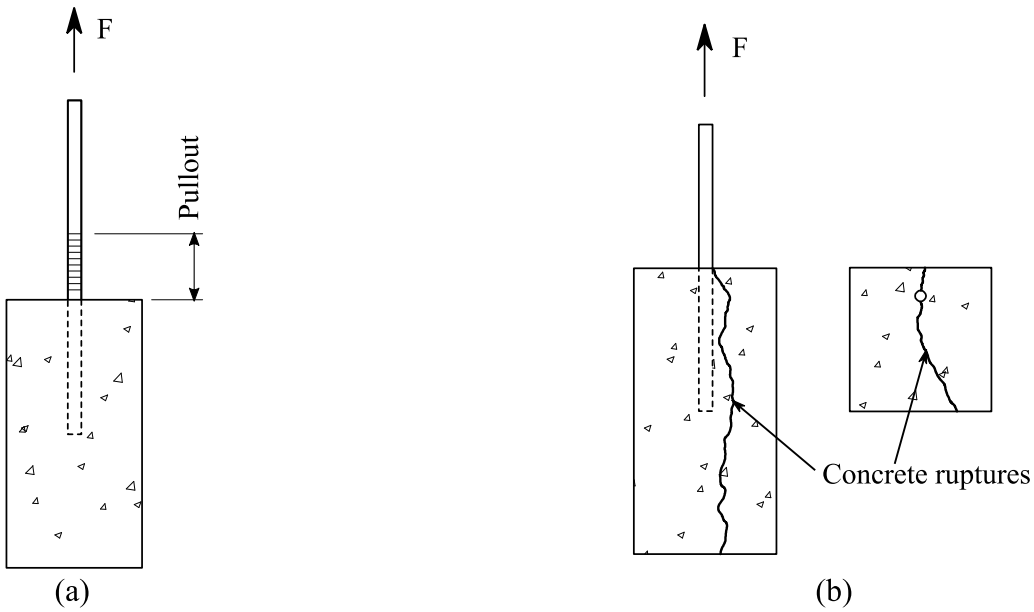

Figure 2.5: (a) Pullout failure and (b) Splitting failure (Rao et al. 2017)

2.2.1.3 Bond in Headed Bars

In reinforced concrete construction, a sufficient amount of bar surface area is needed to be exposed to the concrete to develop anchorage so that the bar can reach its yield stress. For this purpose, bends and hooks are used in plain and deformed straight bars to provide the required development length. This development length can become quite long, especially in concrete with low confinement. This problem becomes more severe particularly in the design of structures for blast loads and in areas of high seismic activities. Due to high levels of steel

congestion, the reinforcement detailing can become very complicated in these cases. The use of headed bars can substantially reduce this congestion and make the construction procedure easier.

Headed reinforcing bar is a relatively new technology. Recent advances in welding have made it cost-efficient to attach steel plates (heads) to the ends of smooth or deformed bars. This head on the bar provides a separate load path, as shown in Figure 2.6. According to Dahl 1995 (as cited in Wright and McCabe 1997), a minimum of 75% of the load is taken by the head, and the remaining 25% load is carried by the conventional bond strength.

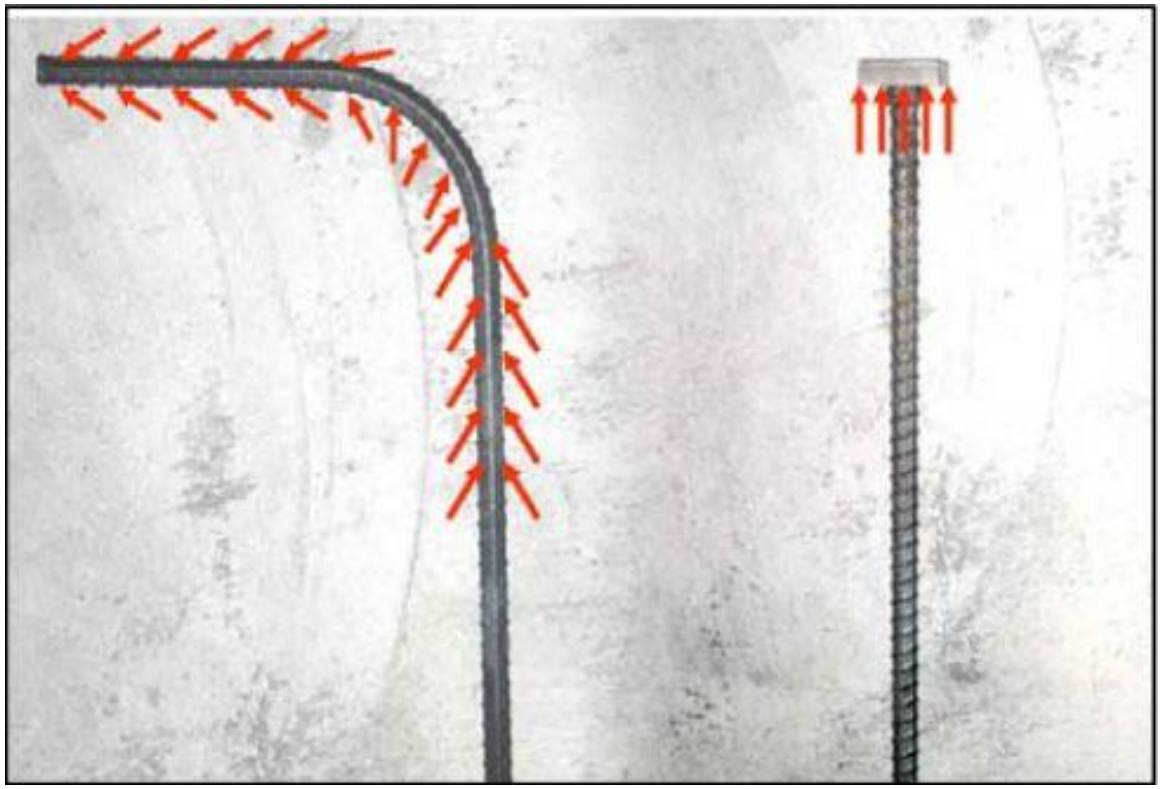

Figure 2.6: Bond force transfer in hooked and headed bars (Courtesy: Headed Reinforcement Corp., CA)

A relatively small amount of literature on the bond behavior of headed bars is available. Most of the early research on headed bars were conducted in Norway, sponsored by Metalock Industries, the producer of headed bars in Norway, or by various oil companies and contractors.

Eventually, much of the early works are proprietary and not published. Later, research works have been carried out in many countries to investigate the effectiveness of headed bars in various types of structures and structural elements. It has been found that in many cases, headed bars can provide better confinement of joints, anchor larger bars, and show a better response to cyclic loading. Figure 2.7 indicates the comparison between the bond stress-strain characteristics in headed bars and hooked bars.

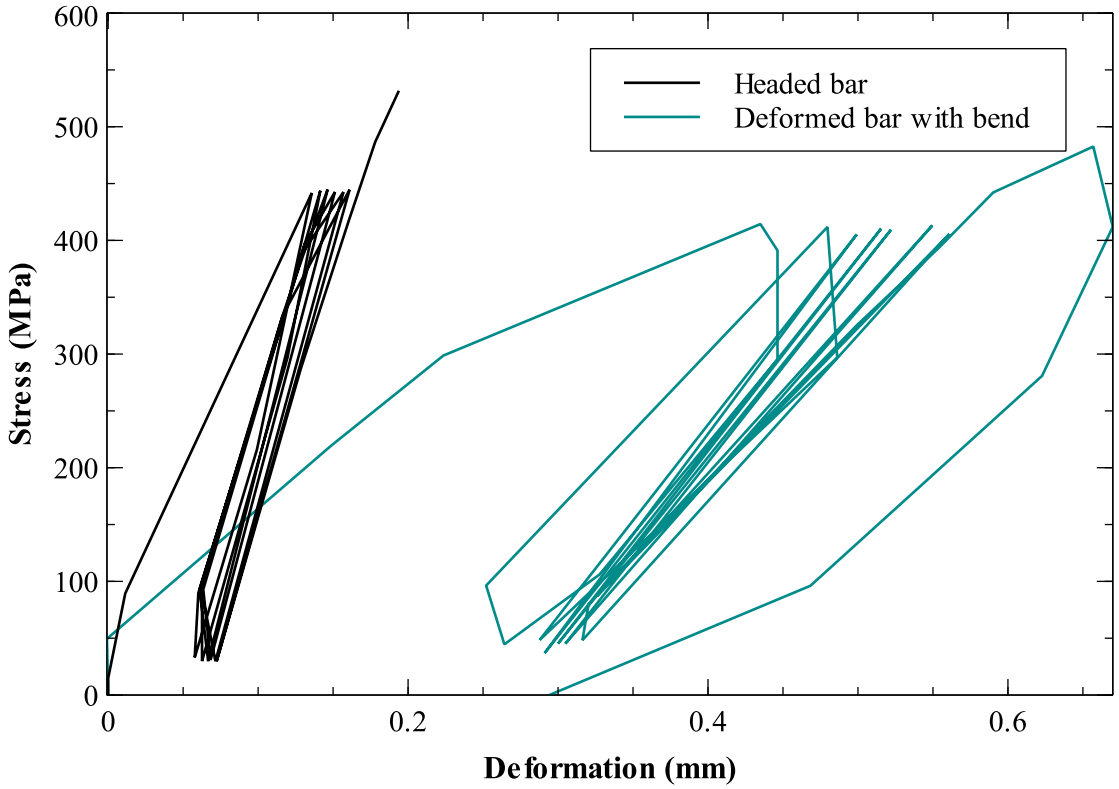

Figure 2.7: Stress-strain behavior of anchorage by headed bar and bent bar under repeated loading. (Fynboe and Thorenfeldt 1986)

Headed bars also show better bond-slip response than hooked and bent bars under monotonic loading conditions. In hooked bar, a radial force of T/R per unit length is exerted on the concrete inside the bend, where T is the tensile force developed in the hook and R is the inner radius of the bend. Thus, the average bearing stress on the concrete is T/Rd_b, where d_b is the

diameter of the bar. According to the ACI 318 Code (ACI Committee 318 2008), $R \geq 2d_b$ for $d_b \leq {}^{5}/_{8}$ in. (16 mm). Using the value of $R = 2d_b$, the average bearing stress on concrete becomes $(\sigma_s \pi d_b^2)/(4)(2d_b^2) = 0.4\sigma_s$; where σ_s is the stress developed in the hook. When σ_s approaches the yield strength f_y of the bar, the bearing stress can damage (split or crush) the concrete inside the bend. This results in bond slip, preventing the hook to develop the stress f_y in the bar. Leonhardt and Walther 1965 (as cited in Ghali and Youakim 2005) measured the slip at the bends of 90-, 135- and 180-degrees of hooks, with heavier bars lodged inside the bends. Eligehausen 1996, carried out similar experiments with headed studs. The comparison between the results obtained by Leonhardt & Walther 1965 and Eligenhausen 1996 is given in Table 1.1.

Table 2.1: Comparison of slips of hooked bars (Leonhardt & Walther 1965) and headed studs (Eligenhausen 1996) anchored in 3.6 ksi concrete.

Stress (ksi)	Slip in Hooked Bars (in)	Slip in Headed Studs (in)
58	0.004 to 0.01	0.0005 to 0.001
72.5	0.008 to 0.035	0.0009 to 0.002

Another advantage of the headed bar is the risk of spalling of concrete cover by straightening bend can be eliminated (Figure 2.8). It can also be seen from Figure 2.8 that, headed bars can still develop the full tensile strength if the cover is lost.

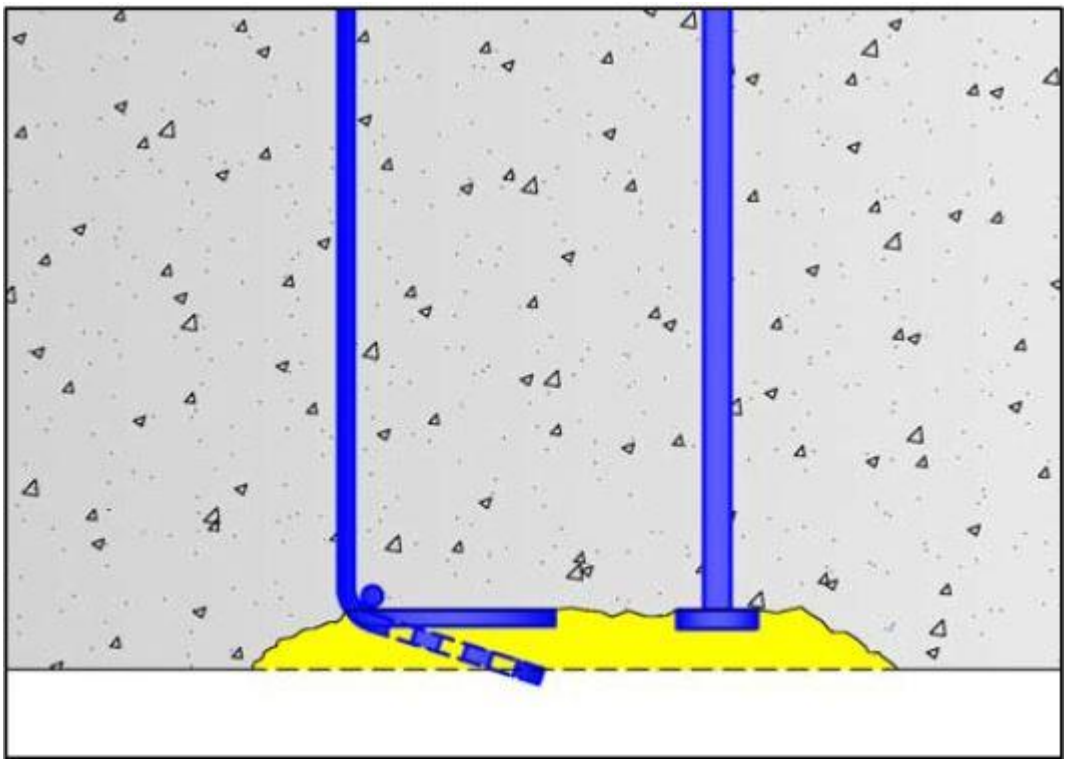

Figure 2.8: Spalling of concrete cover by straightening bend

2.2.1.4 Failure Modes in Headed Bars

The headed bar can fail by yielding or fracturing if the total yield stress or ultimate stress is allowed to develop. Other than that, two failure modes govern the design of concrete members using headed bars- pullout cone failure, and side blowout failure (Figure 2.9). Pullout cone failure is more likely when the ratio of embedment depth to the side cover (distance to the nearest edge of concrete) is small. When this ratio is large, side blowout failure is more probable. The size of the failure cone depends on the embedment length of the headed bar. DeVries 1996, conducted pullout tests on 140 samples and investigated the effect of variables like embedment depth, clear cover over the bar, spacing of adjacent bars and orientation of the heads on bond properties of headed bars.

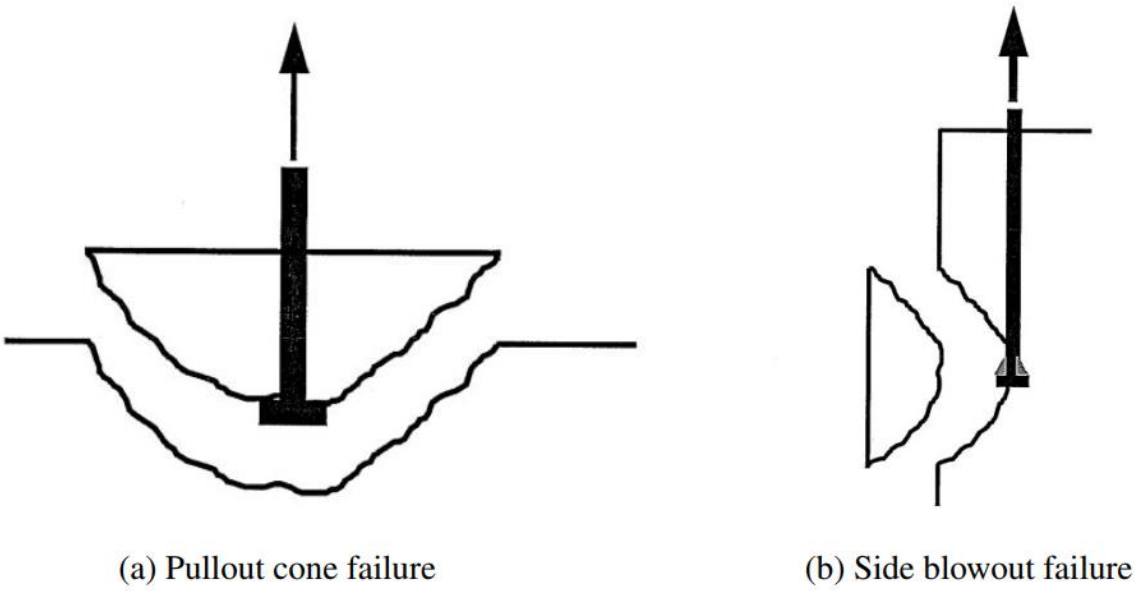

Figure 2.9: Failure modes in headed bars (DeVries 1996)

The tests were done for both shallow and deep embedments. Shallow embedment was defined as the ratio of embedment length to side cover less than five. When the ratio was greater than five, it was considered as deep embedment sample. Various bar sizes with various yield strengths were used. In shallow embedment test, some bars reached the yield stress plateau and went into strain hardening. But in general, bar yielding did not have a dramatic effect on the ultimate pullout load, as shown in Figure 2.10. Also, the observed result showed a trend that the bars with development length had higher pullout loads than the bars with no development length. The no development length condition was achieved by covering the bars with PVC pipes, thus not allowing the bar to bond with concrete. While the edge distance was found to be a factor controlling the size of the pullout failure cone, it was also found that the bars closer to the corner had lower pullout load capacity, as shown in Table 2.2.

.

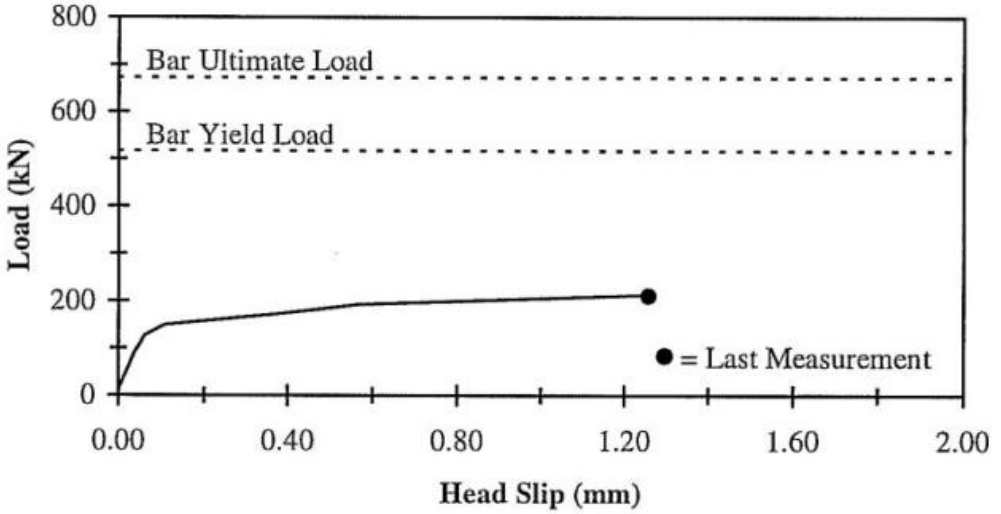

(a) Bar did not reach yield stress

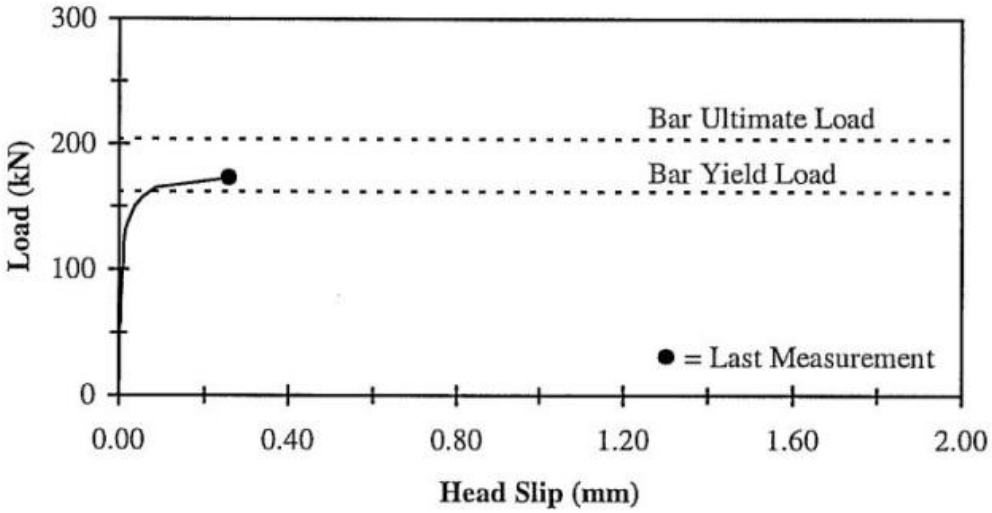

(b) Bar reached yield stress

Figure 2.10: Pullout loads in bars with and without reaching the yield stress (DeVries 1996)

Table 2.2: Effect of bar to concrete edge distance on pullout capacity of headed bars (DeVries 1996)

D_b (in)	Head Dimensions (in)	C_1 (in)	C_2 (in)	L_e (in)	L_d (in)	*T.R.*	f_c' (ksi)	P_U (kips)
0.79	2 x 2 x 0.5	2	2	9	0	None	4.8	19.8
0.79	2 x 2 x 0.5	2	18	9	0	None	4.8	41.4
0.79	2 x 2 x 0.5	18	18	9	0	None	3.9	47.7

The parameters in Table 2.2 are defined as follows:

D_b=bar diameter,

C_1= near edge distance,

C_2= far edge distance,

L_e= embedment length,

L_d= development length,

T.R.= transverse reinforcement,

f_c'= concrete compressive strength,

P_U= ultimate pullout load.

For deep embedments, the samples with no development length or transverse reinforcement failed rapidly with the side cover spalling in a brittle fashion, with no cracking until the failure was imminent. Although in some samples, small cracks appeared near the head region just before failure. For bars with development length, a crack formed at the start of the development length and propagated down to the head as the load increased (Figure 2.11).

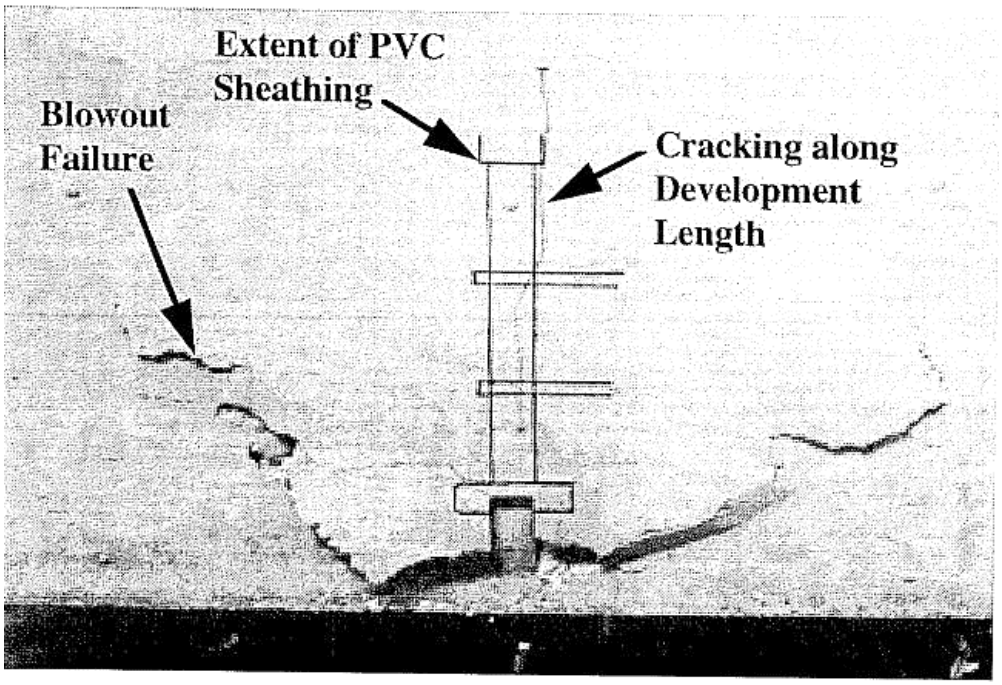

Figure 2.11: Crack along the development length of a headed bar sample. (DeVries 1996)

A wedge of concrete was observed to be formed at the head. The size of the wedge varied with size and aspect ratio of the head. A similar phenomenon was observed by Thompson et al. 2006. 27 lap-slice specimens with headed bars were tested by Thompson et al. A typical specimen is shown in Figure 2.12. It was found that internal cracks always tend to propagate from the head of one bar towards the opposing bar at an angle of 55 degrees measured from the bar axis. On the other end, a well-defined, concrete wedge forms at the head of the opposing bar. This behavior indicates that the actual bond length that propagates the bond force is shorter than the provided splice length (Figure 2.13).

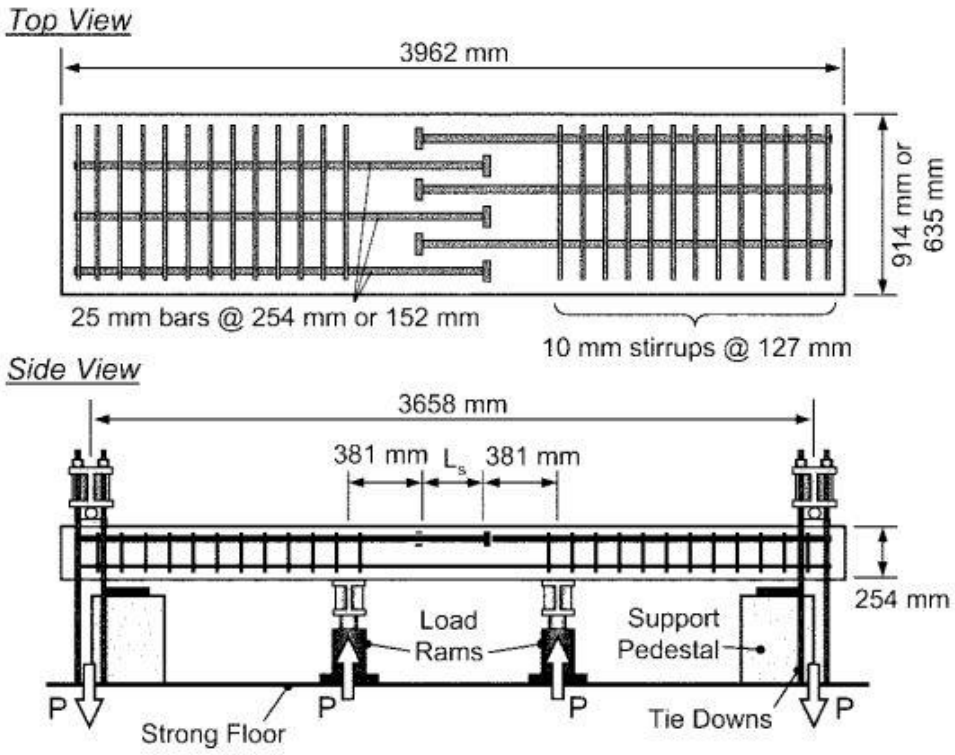

Figure 2.12: Typical lap-splice specimen used by Thompson et al. 2006

Wright and McCabe 1997, observed a 26 to 50% increase in the bond strength using transverse confining reinforcement. This increase of bond capacity depends on the positioning and spacing of the transverse bars, as described by Thompson et al. 2006. Two types of confinements: hairpin and transverse & tie-down confinements (Figure 2.14) were used. The hairpin-confined specimens failed in a much similar fashion to the unconfined specimens. Rapid loss of bond stress (shear force per unit surface area of the interface) and surface cracks over the lap zone was observed. The transverse & tie-down specimens failed more gradually and spalling of cover concrete was largely prevented. Figure 2.14 shows that much of the potential benefits of the hairpins were lost due to their placement outside the bond length. These results indicate that confining reinforcement is not effective if not properly placed.

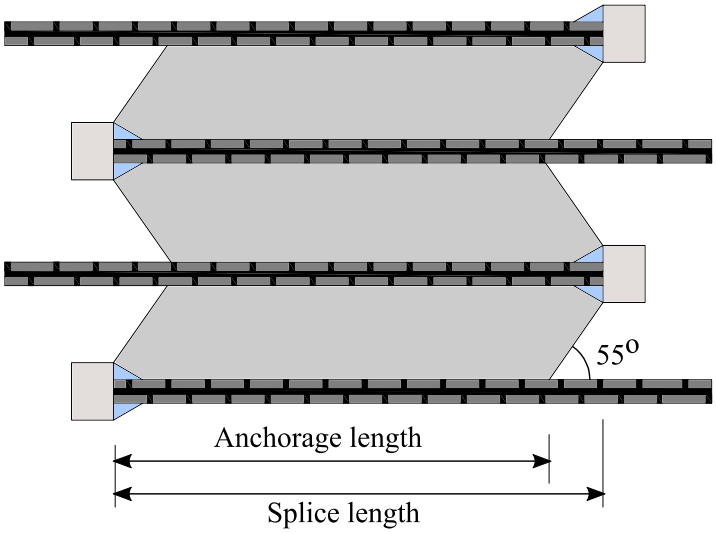

Figure 2.13: Mechanism of force transfer between opposing lapped bars (Thompson et al. 2006)

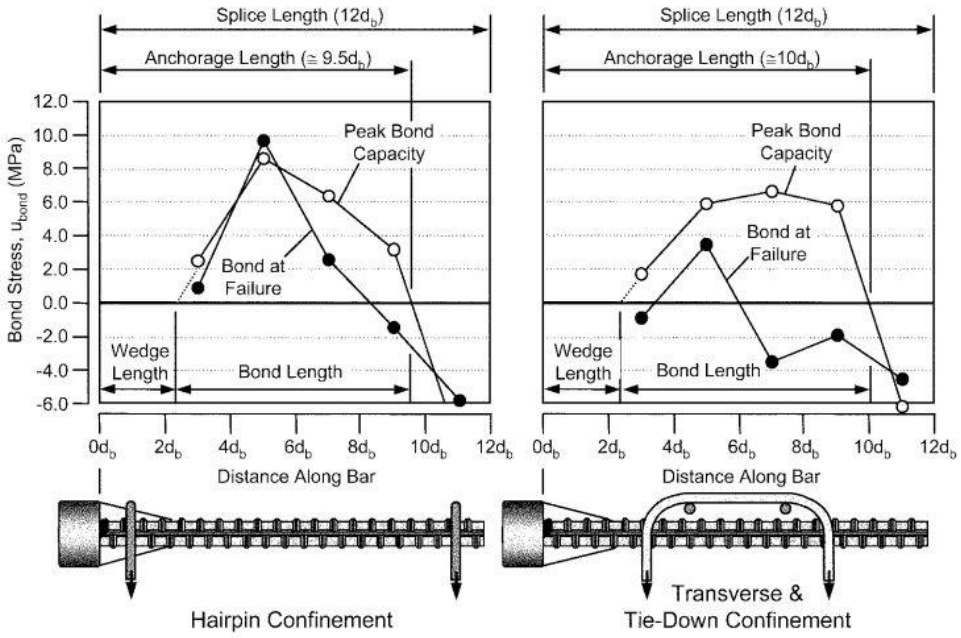

Figure 2.14: Bond stress profiles for confined lap splices (Thompson et al. 2006). The bond stress, u_{bond} is the shear force per unit bond interface area.

2.2.2 Cast-in-place Concrete Connections and Interface Bonding

Cast-in-place or field-cast concrete closure pour is one of the simplest types of connections between two prefabricated concrete elements in Accelerated Bridge Construction (ABC). This is typically created by leaving a small gap between two precast concrete elements and the connection is achieved by using simple lap splices and pouring grout-type concrete material in the gap. This connection method can be used to connect various types of concrete elements. In this study, we will look at the longitudinal connection between the deck bulb-T girders. Various types of grout materials are used as closure pour e.g., regular grout, magnesium phosphate grout, epoxy grout, cable grout, Ultra-High Performance Concrete (UHPC) etc. (Swenty and Graybeal 2013). As a highly suitable closure pour material, UHPC has gained wide popularity in ABC. UHPC's suitability as a closure pour material stems from its high strength values (compressive strength of 24 ksi, splitting tensile strength of 1.3 ksi) and long term drying shrinkage of 550 microstrain (Graybeal 2014). But the downside of UHPC is that, its high material cost and installation cost make the construction more expensive. While the material cost of UHPC lies between $2,000 to $4,000 per cubic yard (Graybeal 2014; De la Varga and Graybeal 2016), according to ITD, its installation cost is around $15000 per cubic yard (Casanova 2018).

In this study, HES concrete with fibers is considered as a proposed alternative to UHPC. The cost of using HES being comparable to that of conventional concrete ($600-$700 per cubic yard), the estimated saving in construction by using HES instead of UHPC can range from $50,000 to $100,000 (Casanova 2018). The figures mentioned here are based on actual ITD bids. This offers a significant economic advantage over the use of UHPC in exchange for a reduction in strength values. This study investigates if this reduced strength is sufficient for ABC in accordance with the design codes.

2.3 Interface Bond Tests (Casanova 2018)

Casanova 2018, performed interface bond tests similar to tests performed by De la Varga et al. 2016 and Graybeal 2017. The tests were performed according to the ASTM C78 testing method. Figure 2.15 shows a schematic diagram of the interface bond test setup. A loading rate of 30 lb/sec was maintained until beam failure occurred.

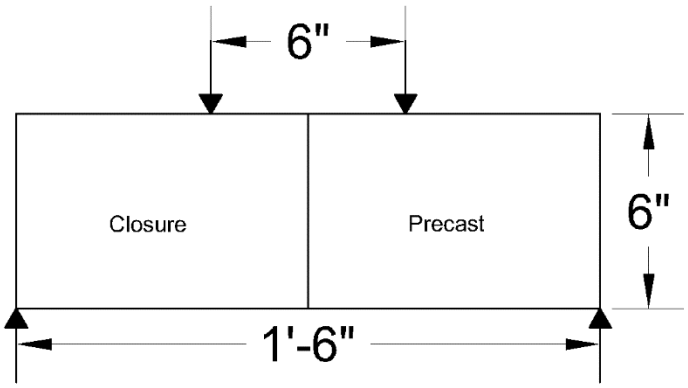

Figure 2.15: Setup for the ASTM C78 flexural bond test (Casanova 2018).

A total of 8 samples for the selected mix D were tested. Bonding agent was used in four of them and the rest four were without any bonding agent. Samples with no bonding agent showed higher interface strength. All the samples failed along the interface and the average modulus of rupture for the interface failure was found to be 612 psi (no bonding agent).

2.4 Headed Bar Pullout Test (Casanova 2018)

Six headed bar pullout samples were tested to study the behavior of the lower portion of a closure pour deck connection between Deck Bulb-T girders. Each specimen was composed of a closure pour concrete section in the middle, sandwiched between two precast concrete sections. Three headed rebars were arranged in the configuration shown in Figure 2.16. Each bar was a #5 bar and the diameter of the head was 1.5 inches.

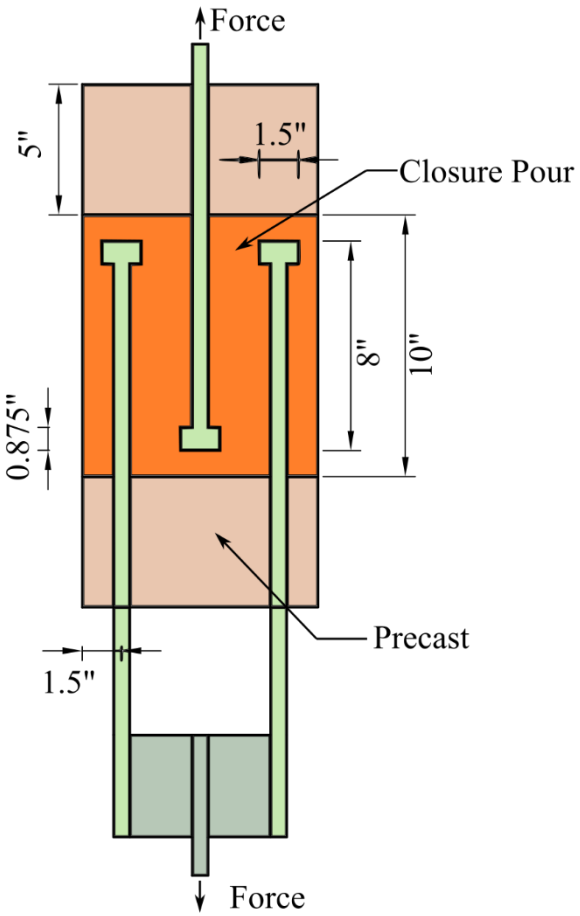

Figure 2.16: Headed bar pullout specimen schematic (Casanova 2018).

A constant loading of 0.01 in/min was applied until failure occurred. In all specimens, the failure of the top interface was the first failure to occur. After reaching the ultimate load, the specimens fractured suddenly and failed. The major cracks in the specimens were observed to be in line with the findings of DeVries 1996. All the specimens showed major cracks along the development length of the rebar and many of the specimens also showed conical cracks that formed near the head of the rebar and propagated at an angle of about 55° with the bar axis.

2.5 Flexural Beam Test (Casanova 2018)

Large beam specimens were tested under three-point and four-point bending. Each beam was 78 inches in length, 12 inches in width and 8 inches in height. The closure pour section was 10

inches long with shear keys on both sides. A total of four headed bars, two from each side, created a lap splice inside the closure at the bottom. Regular reinforcing bars were used in a similar fashion at the top as shown in Figure 2.17. Three of the beams were tested for three-point bending, and the rest three for four-point bending. For three-point bending, the point load was applied on a 1-inch thick steel plate of a dimension of 20 in x10 in sitting on the top of the beam. This was done to simulate a truck wheel load more realistically as prescribed by the American Association of State Highway and Transportation Officials (AASHTO). Loadings for all beam tests were applied at a rate of 0.1 in./min until failure. The schematic diagrams for three-point and four-point bending tests are shown in Figure 2.17.

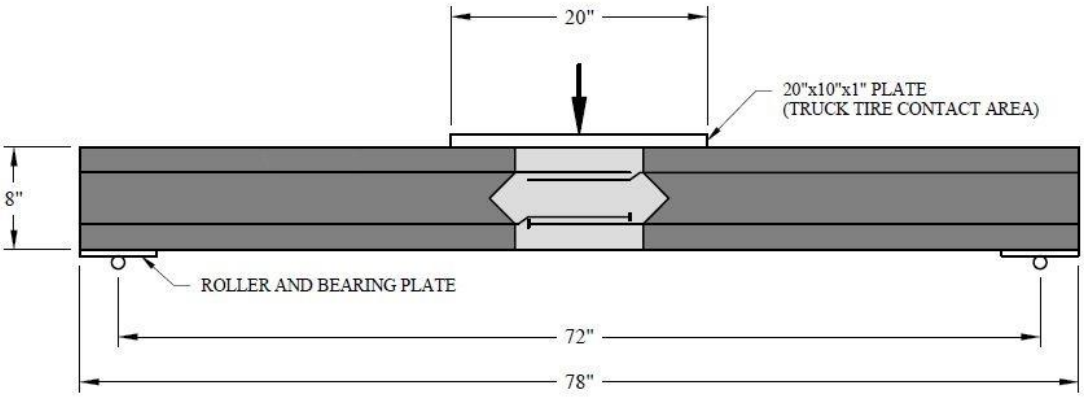

(a) Three-point flexural test.

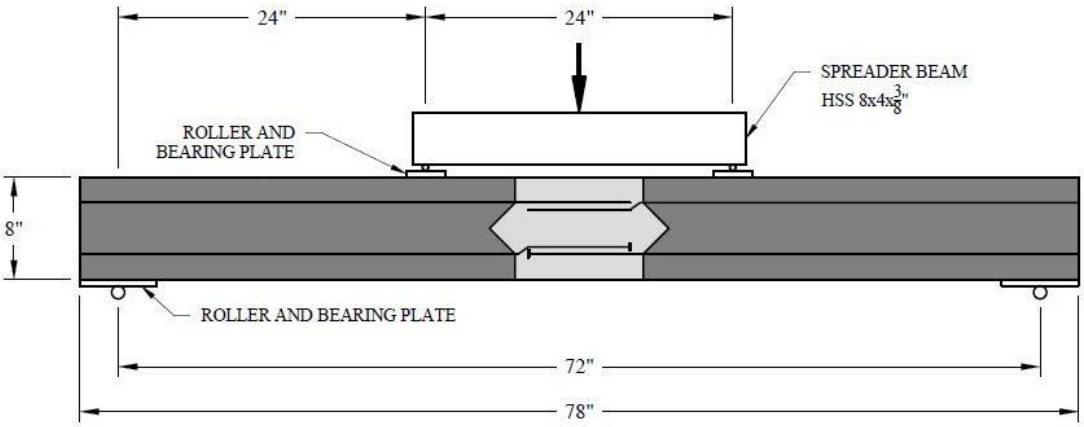

(b) Four-point flexural test.

Figure 2.17: Beam flexural test schematics (Casanova 2018).

In all six cases, the first crack was observed to be formed at the interface- the right interface to be more specific. When the interface failure reached the shear key, the crack started to propagate inside the closure pour section until complete failure of the beam.

Chapter 3: Background on Finite Element Modeling

3.1 Introduction

The highly nonlinear and inelastic behavior of concrete splitting and bar slip makes the analytical study of bond and bond-slip behavior difficult. Over the years, a variety of techniques were used to develop finite element model of steel and bar slip. Various modes of fracture mechanics, continuous damage mechanics and smeared crack approaches were adapted with the use of link, contact or interface elements. In this chapter, one of the most popular and useful analytical approach, Finite Element Analysis (FEA) will be discussed. Previous studies to develop FEA models pertinent to this project will also be reviewed.

3.2 Importance of Finite Element Modeling

Finite Element Modeling, since its conception in the 1940s, has been deemed as a useful tool in various branches of engineering to find approximate solutions to boundary value problems. The demand for developing finite element models for various engineering problems has increased over time. It allows for studying probable behavior of an engineering problem without actually setting up experiments, thus saving cost, time and manpower. In this report, various approaches have been evaluated to model pullout tests of headed rebars in concrete. To test the accuracy of the developed models, test results from previous experimental studies have been compared with the FE results.

3.3 Literature Review

Many approaches have been designed to numerically model the steel-concrete bond behavior and its application in FEA. The modeling of this bond behavior offers several complexities. Firstly, the bond properties depend on a lot of parameters. Also, the bond-slip relationship is a highly nonlinear phenomenon. Generally, the “bond stress” obtained from experiments is an averaged value. Bond-slip is a localized phenomenon and the distribution of bond stress is not

uniform throughout the anchorage length. This distribution cannot be obtained exactly as it is virtually impossible to measure the steel stress at every point in the bar inside the anchorage length. In this case, strain gauges are placed in the reinforcement in regular intervals, and an average bond stress is calculated by dividing the difference of steel stresses at two points, obtained from the strain measurements at those points, by the total bond surface area between those points. Additionally, measuring strains just at the bond surface is very difficult. In most of the literature, the strain gauges are placed at the center of the steel bar, some distance away from the surface.

Several studies have been carried out to model the distribution of bond stress along the anchorage length. Perry and Thompson 1966 studied the distribution of bond stress in eccentric pullout test specimens and in beams with flexural cracks. In eccentric pullout test, the bar at the loaded end was subjected to tensile loads of 2,000 lb, 6,000 lb and 9,000 lb. It was observed that, with the increase of the pullout load, the maximum bond stress point gradually shifts towards the unloaded end (Figure 3.1).

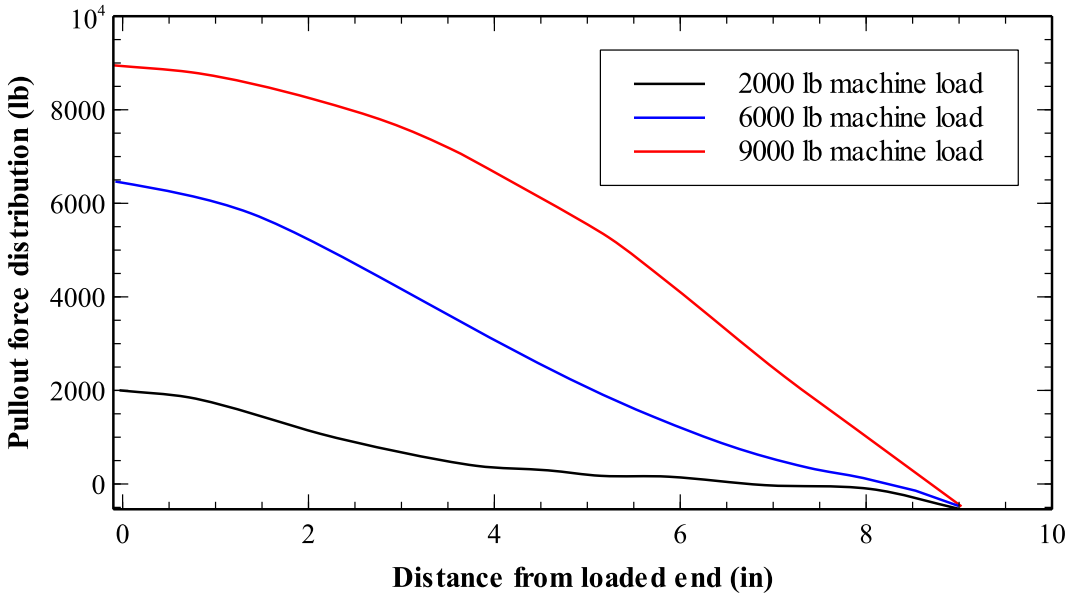

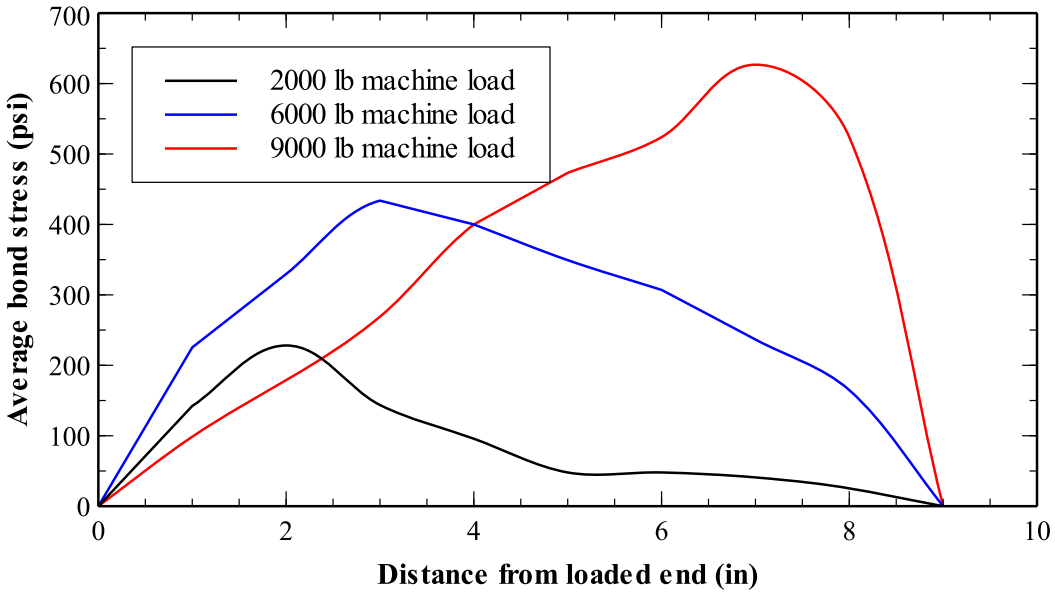

Figure 3.1: Pullout load and bond stress distribution in eccentric pullout test (Perry & Thompson, 1966).

In cracked beam tests, a crack was introduced by means of placing a thin steel sheet, greased on both surfaced in the framework during casting. The test results showed that, the peak bond stress occurs near the crack and always at a distance of about 1.5 in from the crack (Figure 3.2).

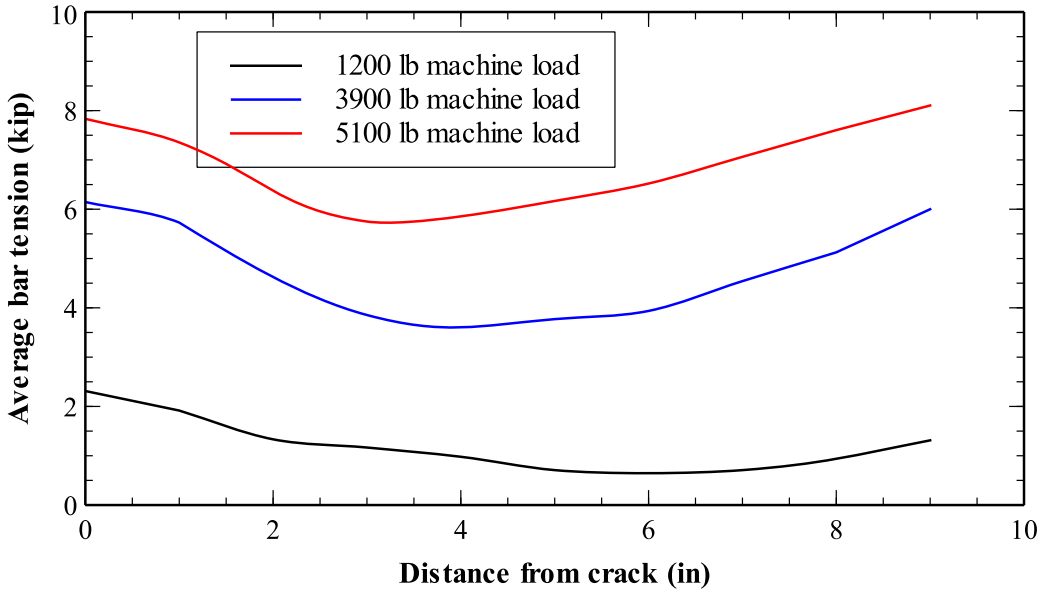

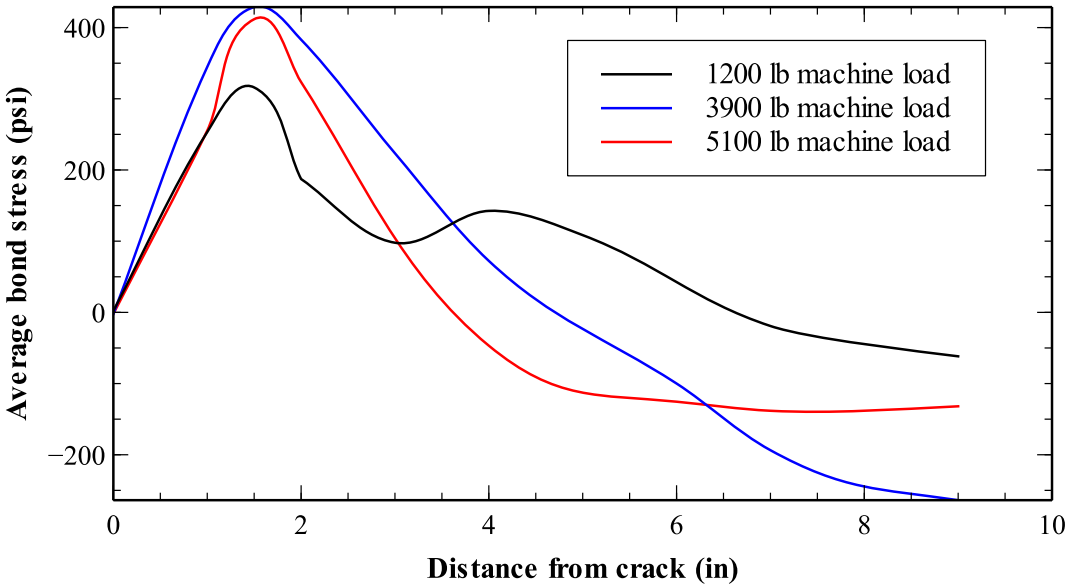

Figure 3.2: Bar tension and bond stress distributions in beam at a crack (Perry & Thompson, 1966).

It is evident that, numerical modeling of the steel-concrete bond needs to accommodate the nonlinearity in bond stress distribution and the bond-slip behavior. However, the first finite element bond elements developed had linear stiffness values. Among those early models, Ngo and Scordelis 1967, proposed a simple two-dimensional bond element. Two orthogonal spring elements connected the adjacent steel and concrete node pair. The springs had no physical dimension which means the adjacent steel and concrete node could occupy the same location. Figure 3.3 is a schematic diagram of the spring element proposed by Ngo & Scordelis 1967.

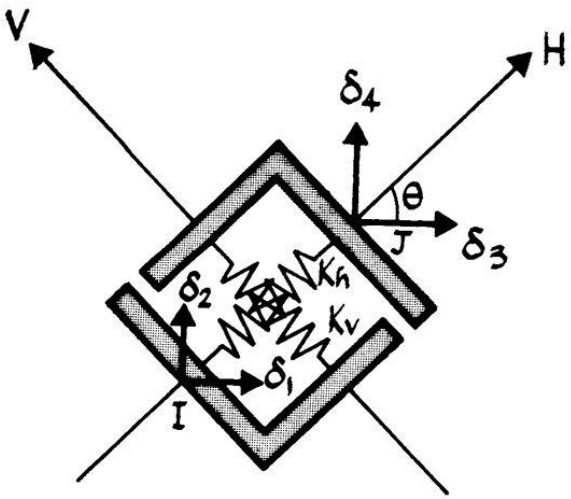

Figure 3.3: Linkage element developed by Ngo & Scordelis, 1967

The two springs are parallel to a set of two orthogonal axes H and V. The local H axis of the spring element can be oriented at an arbitrary angle θ with the horizontal axis of the beam. The spring stiffness K_H and K_V of the two elements parallel to H and V axes respectively, defines the bond stiffness in horizontal and vertical directions. If σ_h and σ_v are the element stresses along the H and V directions, then the stress-strain relationship can be given by

$$\begin{Bmatrix} \sigma_h \\ \sigma_v \end{Bmatrix} = \begin{bmatrix} K_H & 0 \\ 0 & K_v \end{bmatrix} \begin{Bmatrix} \varepsilon_H \\ \varepsilon_V \end{Bmatrix} \quad \textbf{(3.1)}$$

Where ε_H and ε_V are the relative displacements between points I and J in H and V directions respectively. If δ_1, δ_2 and δ_3, δ_4 are the displacements of nodes I and J in global horizontal and vertical directions respectively, then

$$\begin{Bmatrix} \varepsilon_H \\ \varepsilon_V \end{Bmatrix} = \begin{bmatrix} -c & -s & c & s \\ s & c & -s & -c \end{bmatrix} \begin{Bmatrix} \delta_1 \\ \delta_2 \\ \delta_3 \\ \delta_4 \end{Bmatrix} \quad \textbf{(3.2)}$$

Where, $c = cos\theta$ and $s = sin\theta$. This is a linear displacement model and cannot represent the highly nonlinear bond-slip behavior accurately. However, this model could represent the general trend of bond stress distribution. The force in the horizontal spring element could be taken as the bond. Studies with this model showed the peak bond stresses occur near the cracks, which conforms to the experimental studies.

Later, contact elements were developed to model a continuous connection between steel and concrete elements. For example, contact elements proposed by Hoshino 1974 and Schäfer 1975 can be mentioned. Dinges 1983 (as cited in Keuser and Mehlhorn 1988) proposed a generalized contact element. Figure 3.4 shows the contact element with two double nodes and a linear shape function.

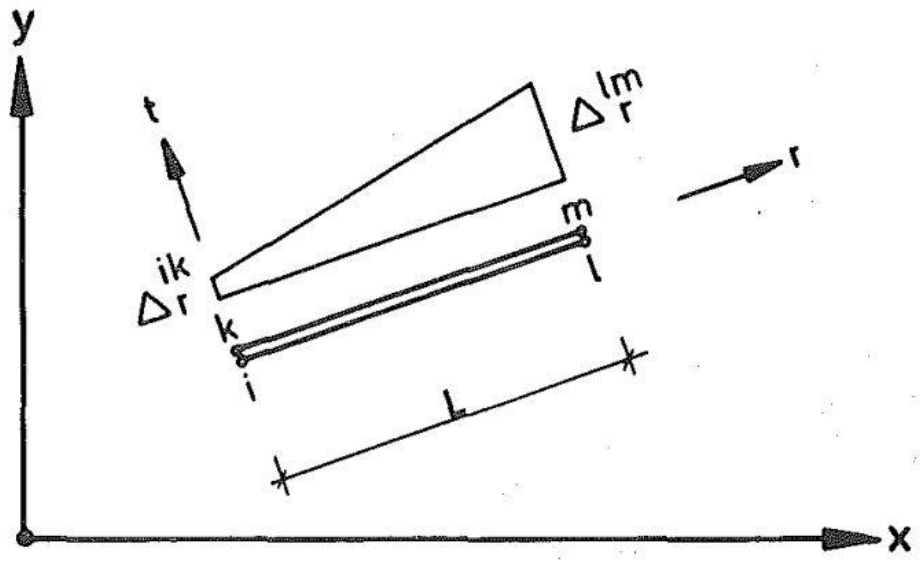

Figure 3.4: Contact element developed by Dinges 1985

i, k and l, m represents two double nodes of the contact element of length L, parallel to an arbitrary local axis r. t is an axis orthogonal to r. Δ^{ik}_r , Δ^{lm}_r , Δ^{ik}_t and Δ^{lm}_t are the relative displacement between the double nodes in r and t directions respectively. If the bar diameter is d_s, the nodal forces R in the local coordinates can be expressed as:

$$\begin{Bmatrix} R_r^{ik} \\ R_r^{lm} \\ R_t^{ik} \\ R_t^{lm} \end{Bmatrix} = \frac{\pi}{6}.d_s.L \begin{bmatrix} 2G_r & G_r & 0 & 0 \\ G_r & 2G_r & 0 & 0 \\ 0 & 0 & 2G_t & G_t \\ 0 & 0 & G_t & 2G_t \end{bmatrix} \begin{Bmatrix} \Delta_r^{ik} \\ \Delta_r^{lm} \\ \Delta_t^{ik} \\ \Delta_t^{lm} \end{Bmatrix} \quad \textbf{(3.3)}$$

Where, G_r and G_t are the bond moduli in *r* and *t* directions respectively. Keuser and Mehlhorn 1988, analyzed the aforementioned bond-link element (Ngo & Scordelis 1967) and contact element (Dinges 1985) behavior with five shape functions. Among them, one was a constant slip function, two linear functions, one quadratic function and one cubic function (Figure 3.5).

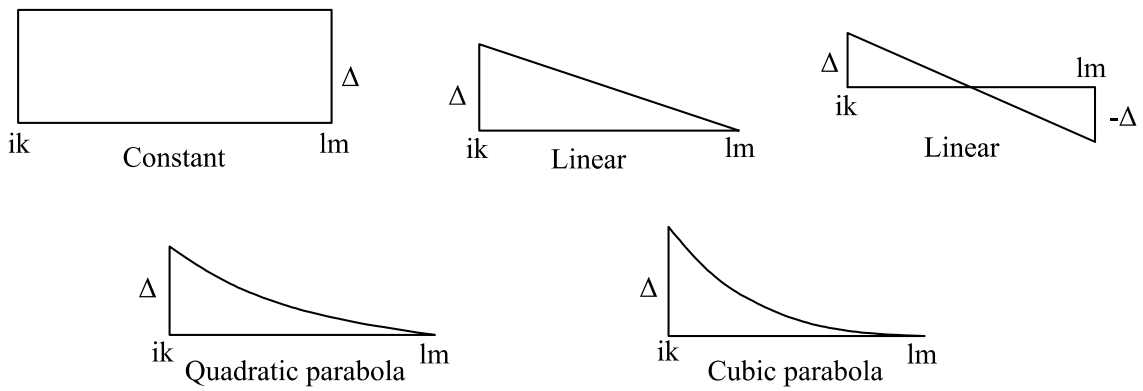

Figure 3.5: Shape functions analyzed by Keuser & Mehlhorn 1988.

Keuser & Mehlhorn concluded that, the contact element a linear displacement function can predict the bond-slip behavior more accurately than the bond-link element with constant displacement function. It was observed that, the accuracy of the result produced by the contact element can be increased further by using quadratic or higher order displacement functions.

Another important aspect that influences the accuracy of the FE model is the material property of the bond element. The material property defines the stress-strain relationship (in this case, the bond stress-slip relationship) in the formulation of the stiffness matrix. From experiments on axially loaded cylinders, Doerr 1980 derived the following bond stress-slip relationship:

$$\frac{\tau_b}{f_{ct}} = 3.28 \times 10^2 \Delta - 1.953 \times 10^4 \Delta^2 + 3.95 \times 10^5 \Delta^3 \quad \textbf{(3.4)}$$

Where, τ_b is the bond stress, f_{ct} is the concrete tensile strength and Δ is the slip, all in inch-pound unit system. Martin 1973, derived a bond model from the studies conducted by Rehm 1961. In the formulation of the bond stress- slip equation, Martin 1973, used three

dimensionless calibration parameters a_0, b_0 and β that depend on compressive strength of concrete and bar rib geometry:

$$\frac{\tau_b}{f'_{c,cube}} = a_0 + b_0.\Delta^{1/\beta} \tag{3.5}$$

Keuser & Mehlhorn 1988, used the equations proposed by Doerr 1980 and Martin 1973, and compared them to the results obtained by FEA using the bond-link element with constant stiffness developed by Ngo & Scordelis 1967 (Figure 3.6). It is evident that, bond elements with constant shape function and linear elastic material properties cannot model the steel-concrete bond-slip behavior with sufficient accuracy.

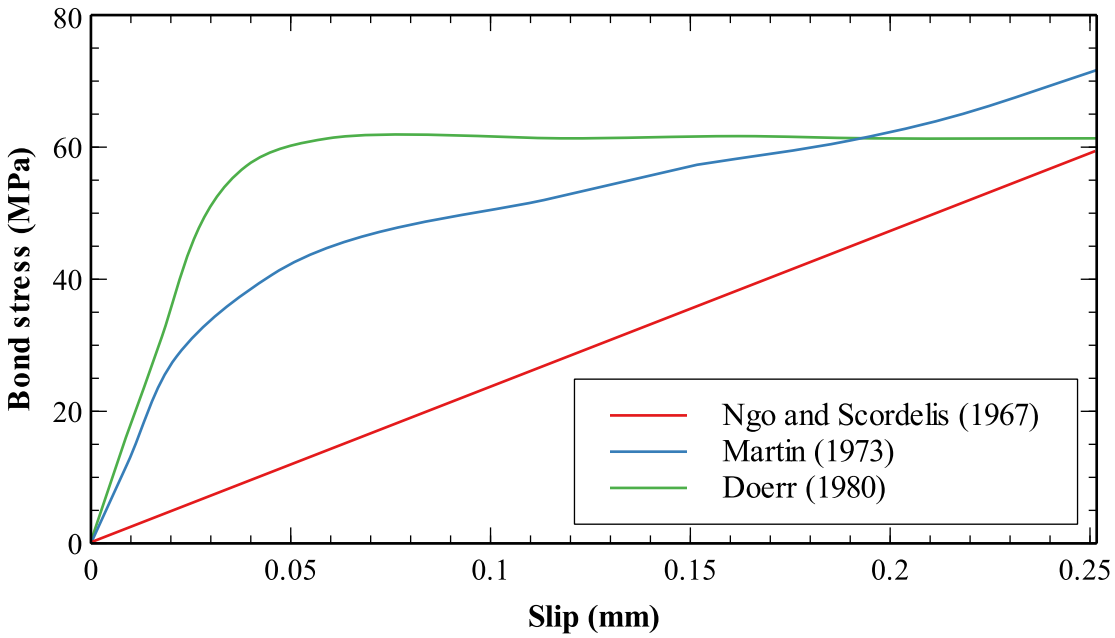

Figure 3.6: Bond stress-slip relations (Keuser & Mehlhorn 1988).

A large portion of the bond-slip nonlinearity arises from the primary and secondary cracks. As a consequence, research works have been carried out to develop Linear Elastic Fracture Mechanics (LEFM) model for steel-concrete bond. Ingraffea et al. 1984, studied the efficacy of LEFM models in FE analysis of steel-concrete bond. Ingraffea et al. argued that, while LEFM works well for metals and many rocks, it is not accurate in case of concrete. The secondary cracks formed near the ribs make LEFM unreliable for reinforced concrete. In LEFM, no stress transfer is assumed between the two faces of a crack after its formation. But in concrete, the secondary cracks are short in length and a significant amount of stress transfer takes place between the faces of the crack until a particular crack opening of about 0.001 in (0.025 mm) is obtained (Catalano 1983; Petersson 1981). This transfer of stress takes place due to aggregate interlocking and frictional force.

Primary studies done by Ingraffea et al. showed the shapes and positions of the secondary cracks. The cracks formed near the ribs and were slanted towards the nearest free concrete surface i.e. the face of primary crack (assuming the concrete cover was large enough). Secondary cracks were more prominent in the region near the primary cracks. The formation of these secondary cracks gradually reduces the stiffness of the concrete; thus the bond stress shows peaks near the primary cracks. Ingraffea et al. studied the nonlinear behavior of load vs loaded end displacement and proposed a "tension softening interface" element that has a nonlinear material property. The nonlinear stiffness of the element was obtained from the curve in Figure 3.7 that has two components- $\Delta_{elastic}$, the elastic displacement, and Δ_{slip}, the displacement due to secondary cracking. E_n is the stiffness of the tension softening element. The mathematical relationship between σ, Δ_{slip}, and E_n is given in Figure 3.7. The element was used wherever the reinforcement crossed a primary crack orthogonally.

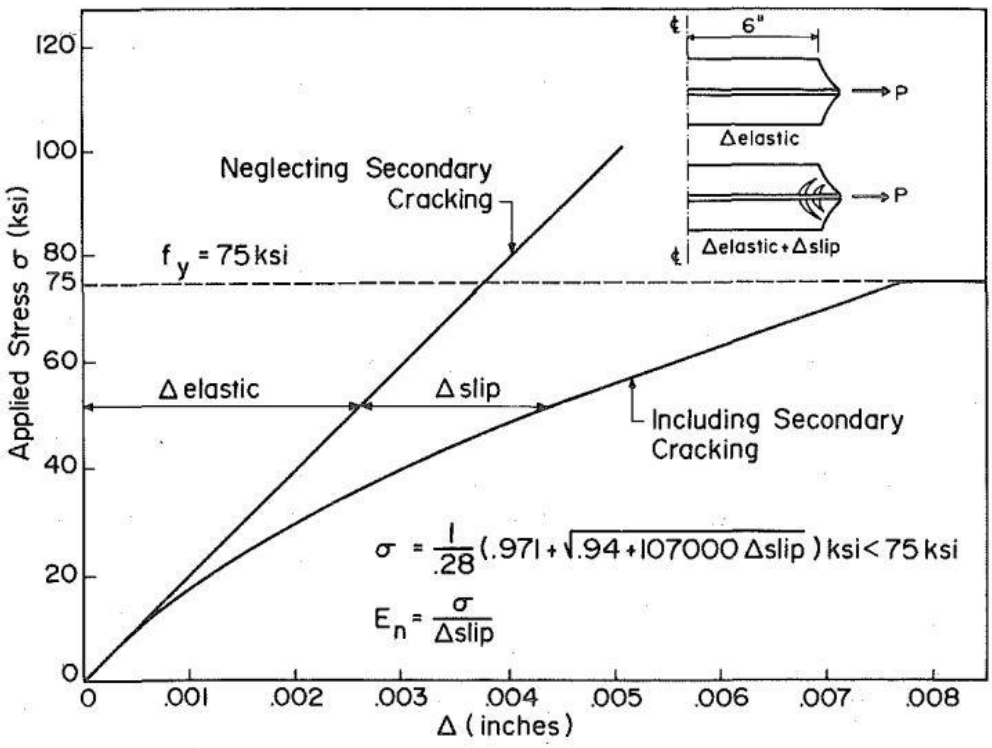

Figure 3.7: Applied load, σ vs end displacement, Δ in tension pullout specimen (Ingraffea et al. 1984).

However, the model proposed by Ingraffea et al. did not take the effects of mechanical interaction between steel and concrete and radial stress in consideration. A bond model using plasticity theory incorporating the effects of mechanical interaction and secondary cracks was developed by Cox and Herrmann 1998. This was a two-dimensional axisymmetric model in "bar scale" i.e. the concrete and the bar were modeled separately, but for simplification, the ribs in the bar were not modeled. This elimination of bar ribs led to two idealizations regarding the general stress-strain response of the bond model. First, the homogenization of the bar-concrete interface traction in the ribs. The traction force exerted by the rib face on the neighboring concrete key was distributed as uniform shear stress τ along the interface element (Figure 3.8).

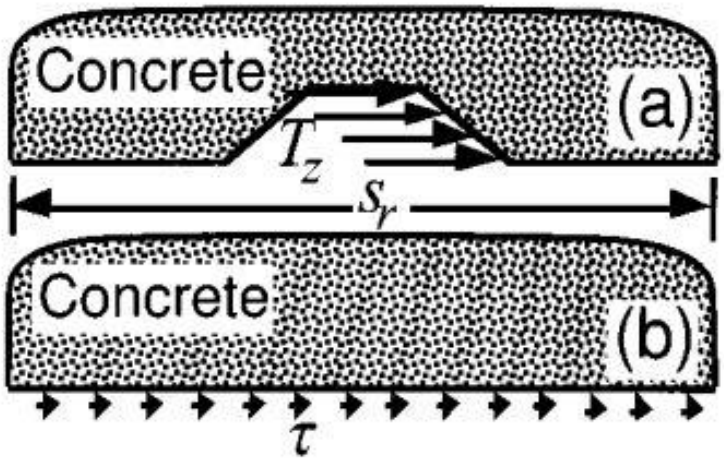

Figure 3.8: Idealized distribution of the horizontal traction component over the unit surface element: (a) actual, and (b) bar-scale model (Cox & Hermann 1998).

A unit surface element representing a complete bar surface for one cycle of rib geometry is shown in Figure 3.8. S_r is the rib spacing. If T_z is the traction force of the rib, then in the idealized model, considering a cylindrical coordinate system with z-axis parallel to the bar axis, the relationship developed by Cox & Hermann 1998 is:

$$2\pi r \int_0^{S_r} \tau(z)dz = -\int_A T_z(z,\theta)dA \qquad \textbf{(3.6)}$$

Where A denotes the unit surface area and r is the radius of the bar. The second idealization is the effect of secondary cracking near the ribs. While Ingraffea et al. 1984, considered the effect of cracking on horizontal displacement of the bar, Cox & Hermann 1998 considered the relative movement of concrete in bond zone in both the horizontal direction and the normal direction (bond zone dilation). Thus, the strain matrix was considered as a function of tangential

(direction of the bar axis) and normal displacements (δ_t and δ_n respectively) of concrete relative to the bar surface, normalized by the bar diameter D_b. That is,

$$\{u\} = \frac{1}{D_b}\begin{Bmatrix}\delta_t \\ \delta_n\end{Bmatrix} \tag{3.7}$$

Figure 3.9 depicts an idealized deformation where $\delta_t < 0$ and $\delta_n > 0$.

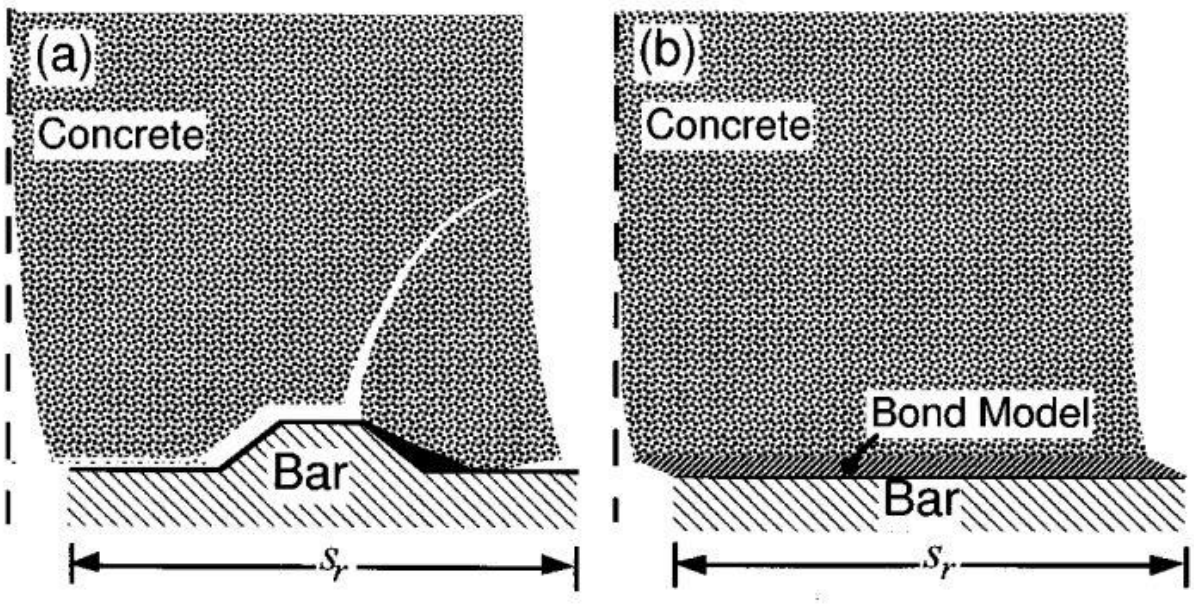

Figure 3.9: Idealized deformation of the bond zone: (a) actual, and (b) bar-scale model (Cox & Hermann 1998).

For the yield surface model, various linear combinations of the following two criteria (the "exponential" criterion and the "power" criterion respectively) were considered:

$$\left|\frac{\tau}{f_t}\right| = C_e(d)[1 - e^{-\alpha_e(-\sigma/f_t + \sigma'(d))}] \tag{3.8}$$

$$\left|\frac{\tau}{f_t}\right| = C_p(d)\left|\frac{-\sigma}{f_t} + \sigma'(d)\right|^{\alpha_p} sgn\left(\frac{-\sigma}{f_t} + \sigma'(d)\right) \quad \textbf{(3.9)}$$

Where, f_t is the concrete tensile strength, α_e and α_p are two calibration parameters, σ' is the kinematic softening function and C_p and C_e are the isotropic hardening and softening functions. σ', C_p and C_e were considered as the functions of a single parameter d for simplification. d is the "damage factor" proposed by Eligehausen et al. 1982. As the slip progresses the length of a unit cell, s_r, the concrete key between the ribs fails by the combined action of crushing and shear or gets wedged radially outwards by the ribs. Thus, the effect of mechanical interlock diminishes, and only the effect of friction remains. The "damage factor", d represents the monotonic envelope of this phenomenon. Based on experimental observations, Cox & Hermann 1998 defined the value of d as:

$$d = min\left(\frac{\delta_t}{s_r}, 1\right) \quad \textbf{(3.10)}$$

This bond model developed by Cox & Hermann 1998, reproduced the bond vs slip relation well. Although, it only considered the bond phenomena inside the "bond radius" zone (Goto 1971). This zone does not contain the primary cracks and the transverse cracks that cause pullout cone. Additionally, the effects of non-axisymmetric rib patterns and cracks were averaged in this model.

3.4 Introduction to ANSYS

In this study, ANSYS 18.1, a general-purpose FEA software was used. ANSYS was first developed by the ANSYS Inc.® in 1970. Since then, it was developed to solve FE models related to structural analysis, fluid mechanics, thermodynamic and electromagnetic problems. It can solve both static and dynamic problems as well as linear and nonlinear models. For its diverse problem-solving capacity, ANSYS is one of the most popular FE software used in both industry and academic research. In this study, only the nonlinear static structural module of the ANSYS 18.1 suite was used.

3.5 Modeling Options in ANSYS

ANSYS offers a variety of options in terms of element and material selection. Some of the options that were considered in this study are discussed in the following sections.

3.5.1 Concrete

3.5.1.1 Smeared Crack (SOLID65)

SOLID65, also known as CONCRETE65, is an 8-node brick element to model 3D solids with or without reinforcing bars (ANSYS Inc. 2016). The reinforcing bars can be modeled using the native "smeared rebar" option where the rebars can be defined to be smeared throughout the element in three different directions. This can be input as three real constants each having four parameters named MAT, VR, THETA, and PHI. MAT and VR are the material properties and the volumetric ratio of rebars with respect to concrete in a particular direction respectively. THETA and PHI are the directions in terms of angels from the x-axis towards the y and z-axes in the global coordinate system. Moreover, the SOLID65 element has a unique capability of crushing and cracking in compression and tension respectively. The crack at an integration point is represented by introducing a plane of weakness in the direction of cracking i.e. the material turns from isotropic to orthotropic (ANSYS Inc. 2013). When the element crushed

due to compression at an integration point, it is defined as the complete deterioration of the structural integrity of the material and the structural stiffness at the integration point in question can be ignored. To determine the failure in tension and compression, the William-Warnke failure criterion is employed (Willam and Warnke 1975). These features make it a very suitable element to model concrete. But it is also to be noted that, these features introduce a lot of nonlinearities in the FE model and often create convergence problems.

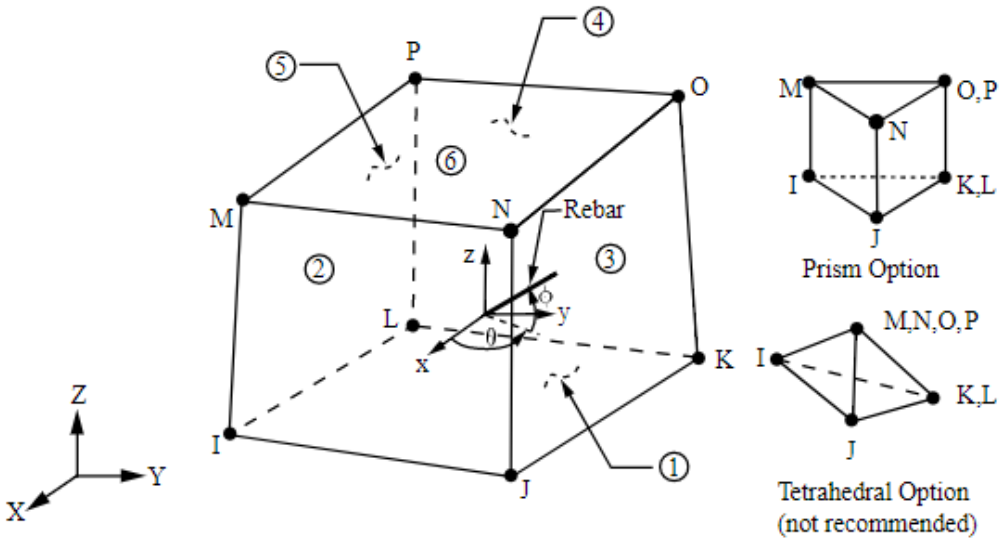

Figure 3.10: Geometry of SOLID65 element (ANSYS Inc. 2016).

3.5.1.2 Cast Iron Model

With the default material specification option in ANSYS, the plasticity curve is mirrored in both tension and compression. But this is not suitable for materials like concrete that have different compressive and tensile strengths. To model different tensile and compressive properties, the Cast Iron material model in ANSYS can be used. it was originally developed to model grey cast iron which is a two-phase material with different compressive and tensile behavior (Hjelm 1994). There are three input parameters- plastic Poisson's ratio, uniaxial compression and uniaxial tension. The latter two are input as sets of stress-strain points

representing multi-linear isotropic hardening behavior. These points are obtained from the uni-axial compression and tension tests of the material respectively. Plastic Poisson's Ratio is a FEM concept to address plasticity problems with a changing Poisson's ratio. The actual, elastic Poisson's ratio has to be defined with the elastic properties of the material.

3.5.1.3 Drucker-Prager Concrete

The classic Drucker-Prager law (Drucker and Prager 1952) is applicable for granular materials like soil and concrete. However, the single-surface classic Drucker-Prager model cannot often represent the large difference in the tensile and compressive strengths of concrete (ANSYS Inc. 2013). The Drucker-Prager concrete model combines two yield surfaces to represent concrete behavior more realistically. The basic Drucker-Prager concrete requires three inputs- uniaxial tensile strength, uniaxial compressive strength, and biaxial compressive strength. However, the Drucker-Prager concrete can also model the post-failure softening behavior. In that case, it requires six additional parameters. These parameters are explained in Table 3.1 and also graphically represented in Figure 3.11.

Table 3.1: Linear Softening Model parameters for Drucker-Prager concrete (ANSYS Inc. 2013)

Parameter	Property	Range
K_{cm}	Plastic strain at uniaxial compressive strength	$0< K_{cm}< K_{cr}$
K_{cr}	Ultimate effective plastic strain in compression	$K_{cr}> K_{cm}$
Ω_{ci}	Relative stress at onset of nonlinear hardening	$0\leq \Omega_{ci}\leq 1$
Ω_{cr}	Residual compressive relative stress	$0\leq \Omega_{cr}\leq 1$
K_{tr}	Plastic strain limit in tension	$K_{tr}\geq 0$
Ω_{tr}	Residual tensile relative stress	$0\leq \Omega_{tr}\leq 1$

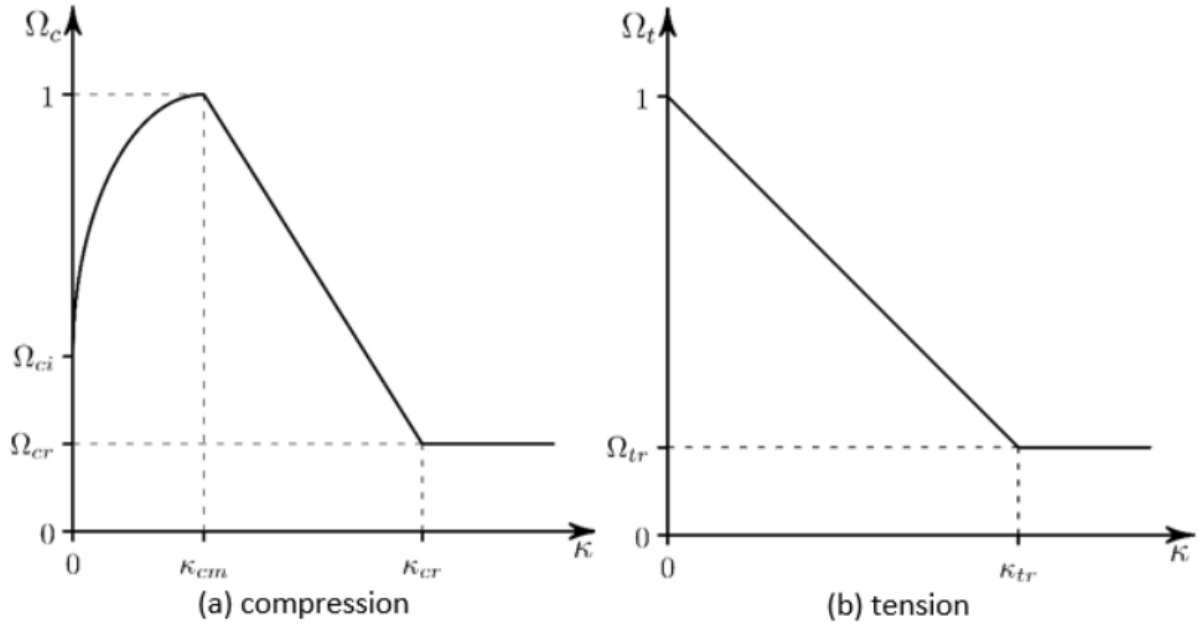

Figure 3.11: Softening in Compression and Tension for Drucker-Prager concrete (ANSYS Inc. 2013).

3.5.2 Concrete-Concrete and Steel-Concrete Bond

3.5.2.1 Nonlinear Spring (COMBIN39)

COMBIN39 is a nonlinear spring model that can be used in 1-D, 2-D or 3-D simulations. It can have a zero or non-zero length. The non-zero length spring elements are generated between two coincident nodes and have 1-D application only. The spring stiffness is input as points in a Force-Displacement curve. This element can be used as an interface element between steel and concrete similar to that proposed by Ngo and Scordelis 1971.

3.5.2.2 Contact Debonding and Interface Delamination

Contact debonding and interface delamination are two techniques in ANSYS that can simulate progressive separation of a bond. Both methods overlap and are essentially the same in most of the aspects. The difference is that debonding is associated with contact elements and delamination is associated with interface elements. Contact elements are used to define other

contact features (friction, perfect bond, friction-less sliding etc.) too but the interface elements do not have these capabilities. Debonding and delamination can be modeled using two methods- Cohesive Zone Model (CZM) method and the Virtual Crack Closure Technique (VCCT) method. The CZM method is bond shear-separation distance based, while the VCCT method is based on fracture energy. The CZM method is simpler and more suitable for modeling the steel-concrete bond. There are two methods of formulation for the CZM method- bilinear and exponential. They are essentially the bond traction (τ) and relative displacement of the two surfaces (δ). Both the curves have two arms, one that reaches to the maximum bond stress and the other one represents the subsequent softening of the bond (Figure 3.12).

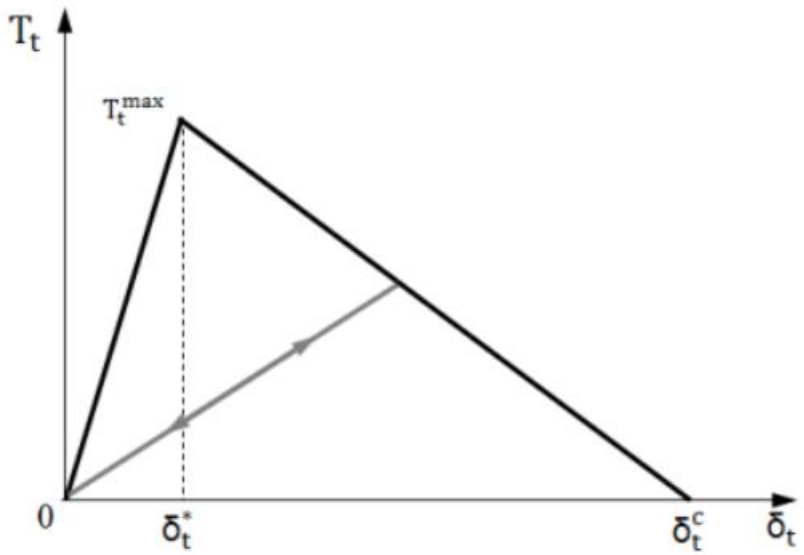

Figure 3.12: Bilinear CZM method graph (ANSYS Inc. 2013).

Chapter 4: Methodology

4.1 Introduction

Finite element models for the experimental pullout tests and the beam bending tests done by Casanova 2018 were developed. Issues arose regarding the finite element modeling of the steel-concrete bond, concrete-concrete bond in both the tests and the loading pattern in the three-point bending test. Various options were explored to overcome the issues and to obtain the most accurate results in the nonlinear region of the simulations.

4.2 Development of FE Models

4.2.1 Pullout Tests

Pullout tests can give the nature of the bond developed between the reinforcing bar and the concrete matrix surrounding the bar. In this case, it can also provide insight about how much anchorage the head of the rebar is providing. As a part of the experimental phase of the project, several pullout tests were carried out by Casanova 2018. In this chapter, finite element model will be developed to represent the pullout tests. Before developing the models for experiments by Casanova 2018, a simple pullout test based on the studies by Delhomme et al. 2016 was modeled for calibration and verification purpose.

4.2.1.1 Pullout Test by Delhomme et al. 2016

Delhomme et al. 2016 conducted several experiments on pullout behavior of headed anchor bolts in concrete at University of Lyon, France. The specimen T3-80-U was chosen to be modeled in ANSYS. A 60 mm diameter anchor head was attached to the end of an 80 mm long plain bar with 20 mm diameter. The depth of the head was 20 mm. Due to the use of plain bar, the sides of the bar was not bonded to the concrete. The specimen was embedded in a 600 mm deep concrete block. Figure 4.1 shows the experimental setup.

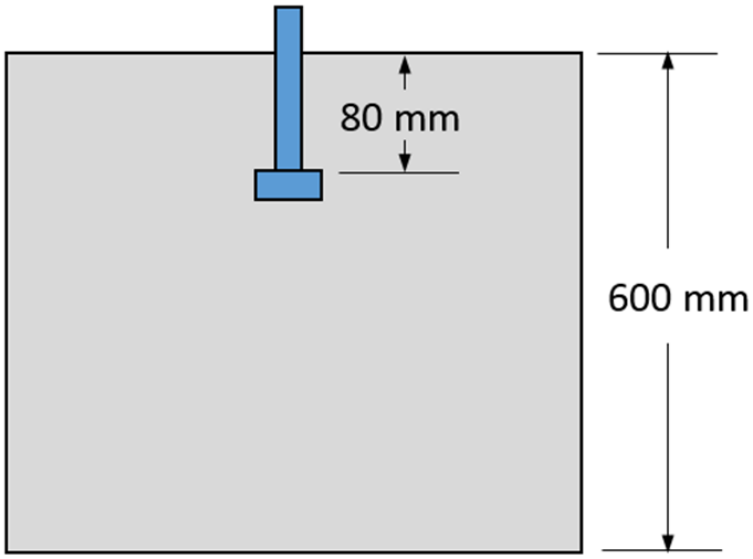

Figure 4.1: Experimental setup of the pullout test (Delhomme et al. 2016).

The free end of the bar was pulled and the displacement at the free end was monitored with two Linear Variable Differential Transformers (LVDT). In ANSYS 18.1, elements SOLID65 and SOLID185 were used to model the concrete and steel respectively. The reason behind using SOLID185 is that it is also an 8-node brick element that has a geometry similar to SOLID65. The parameters for the material properties were taken from the experimental data. The parameters are given in Table 4.1.

Table 4.1: Parameters for the FE Model of Experiments by Delhomme et al. 2016

Parameter	Concrete	Steel
E (MPa)	35,300	200 x 10^3
Poisson's Ratio	0.2	0.3
f'_c (Mpa)	55.2	415
f_t (MPa)	4.5	415

The compressive crushing was turned off in the concrete model, while it could crack in tension. The edges of the upper face of the concrete block were constrained in all direction. The upper surface of the bar was given an outward displacement of 3 mm. The "Large Deflection" option was turned on to account for the geometric nonlinearities due to deflection. The sides of the bar were not bonded; i.e., they could slide freely over the neighboring concrete surfaces. But the upper portion of the head was bonded to the concrete for allowing complete activation of the head. Chapter 5 presents a summary of the results.

4.2.1.2 Pullout Test by Casanova 2018

Two finite element models for the pullout tests done by Casanova 2018 were created- one with assuming perfect bonding between the sides of the rebar and the upper surface of the head and the concrete, one with using nonlinear spring element COMBIN39 between steel and concrete to simulate bond-slip response. A chronological overview of the modeling attempts is given below-

- A quarter and a half model of the pullout specimen were modeled in ANSYS. In both cases, all the parts (the precast, the closure pour and the headed bars) were perfectly bonded. SOLID65 elements were used to model the concrete parts, and the steel rebars were modeled using SOLID186, another 8-noded 3D solid element. Obviously, these models showed stiff responses and produced much conservative results. The ultimate force was found to be 9,500 lb. But the force versus stress in the steel graph was much steeper than the experimental results. Also, these models failed to display the behavior in the nonlinear region.
- In the second attempt, the interface between the closure pour and the precast section was introduced as a thin layer of SOLID65 element that had the same tensile strength

as the flexural interface strength found from the flexural bond test. The value of the interface bond strength found experimentally was 612 psi. All other parameters of the model were the same as before. The interface layer was 0.5 inch thick. Up to this point, in the material properties definition, the tensile strengths for precast and closure pour concrete were considered to be 614 psi and 784 psi respectively. These values were found experimentally from splitting tensile test. This model could imitate the experimental results in the linear region very accurately but encountered convergence issues once it reached the nonlinear region. Moreover, it overestimated the ultimate strength by about 20%.

- To compensate for the overestimation of the ultimate strength, the tensile strengths for the closure, precast and interface sections were reduced to 556 psi, 435 psi and 256 psi respectively. The justification for this reduction will be discussed later in this chapter. Like the previous model, this model also showed a very good agreement with the experimental results in the linear region, and the ultimate strength came down to a reasonable value of 11,600 lb. But it still could not avoid the convergence issues in the nonlinear region.
- Another model, which was same was the previous model, was developed. But this time, the Arc-Length method was activated in the solution phase. The Arc-Length method, also known as the Modified Riks Method, is a geometric expansion to the Newton-Raphson method and a very powerful tool for highly nonlinear finite element problems (Riks 1979). This model showed better results than the previous ones. But still, it could not give enough data points in the nonlinear region.
- At this point, it was evident that, the bond-slip between rebar and concrete plays a significant role in the results. However, from the literature also manifested that, FE modeling of bond-slip is a complicated task. New ways to better model the closure pour

to precast interface were also explored. For these purposes, two options namely nonlinear spring interface element and Cohesive Zone Modeling (CZM) were explored and a final model was prepared using these options. The details of this model will be discussed in this chapter. A schematic diagram of the FE model is shown in Figure 4.2.

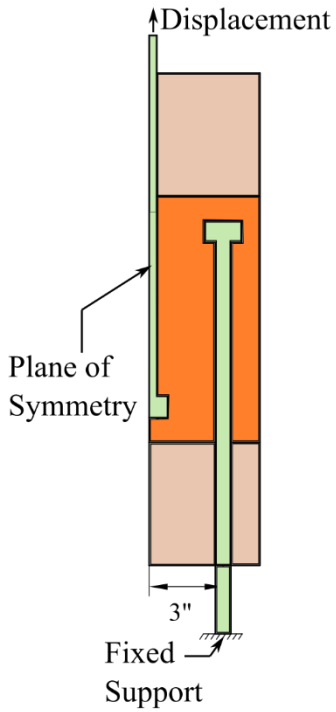

(b)

Figure 4.2: Schematic diagram of the pullout test FE model.

Cohesive Zones were defined in the two closure-to-interface regions. Mode I Cohesive Zone Model was used which debonds only due to normal stress. The maximum normal stress for debonding was defined as 256 psi, and the contact gap at the completion of debonding was defined as 0.1 inch. The interface strength was determined from the modulus of rupture determined from 6 four-point bending tests which was found to be 612 psi. The reduced value

of 438 psi was based on the studies conducted by Kim and Reda Taha 2014. They studied the relationship between the modulus of rupture, splitting tensile strength and direct tensile strength of concrete. The relationships are given by the following equations:

$$f_r = 0.85\sqrt{f'_c} \quad \textbf{(4.1)}$$

$$f_{sp} = 0.49\sqrt{f'_c} \quad \textbf{(4.2)}$$

$$f_t = 0.35\sqrt{f'_c} \quad \textbf{(4.3)}$$

Where, f_r, f_{sp}, f_t and f'_c are the modulus of rupture, splitting tensile strength, direct tensile strength and compressive strength of the concrete respectively in terms of MPa. The value of 438 psi is found from the relation between f_r and f_{sp}. The tensile strengths of the closure pour, and precast concretes used in the model (Table 4.2) were obtained from the experiments of Casanova 2018, which were the splitting tensile strength. To be consistent, the rupture modulus of the interface was used to obtain its splitting tensile strength. The steel was modeled as a linear isotropic material with a modulus of elasticity of 29×10^6 psi and Poisson's ratio of 0.3.

Table 4.2: Parameters for the FE Model of pullout test by Casanova 2018.

Parameter	Closure Pour	Precast
E (psi)	4.33×10^6	3.3×10^6
Poisson's Ratio	0.194	0.191
f'_c (psi)	8,453	5,258
f_t (psi)	778	614

From the previous attempts, it was evident that, the meshing of the model plays a very important role in the speed and accuracy of the simulation. The brick elements created by "sweep meshing" have a greater tendency of convergence than its tetrahedral counterparts. Also, brick meshes have better aspect ratio in general and also reduce the total number of nodes and elements to a great extent. This is especially important for SOLID65 elements, as they are highly nonlinear and often unstable due to their cracking and crushing capabilities. But, manual meshing, especially sweep meshing is a complicated task. It requires experience and patience from the person creating the mesh. A body cannot be swept, if (ANSYS Inc. 2016):

- There is a completely contained internal void in the body.
- A source and target pair cannot be found. That is, the sweeper cannot find at least one path from a source surface to a target surface connected by edges or closed surfaces.
- If a "Sizing control" is used on a body with hard edge sizing and the source and target faces contain hard divisions which are not the same for each respective edge.

To make a body "sweepable", it is often required to divide the body into several parts until each part satisfies the requirements to be swept. But, too many divisions can make the setup of the FE model very complicated, especially in terms of contact definitions. So, a compromise must be found based on the particular model. A model can perform in a satisfying manner if the number of tetrahedral SOLID65 elements is below 10% of the total number of elements (ANSYS Inc. 2016). So, a 3D quarter model was created and divided in such a way so that more than 90% of it can be meshed using brick elements. Also, the sizing of the meshes had to be defined carefully so that the steel elements and the neighboring concrete elements have coincidental nodes that will be used for defining the spring elements. The final meshing is shown in Figure 4.3.

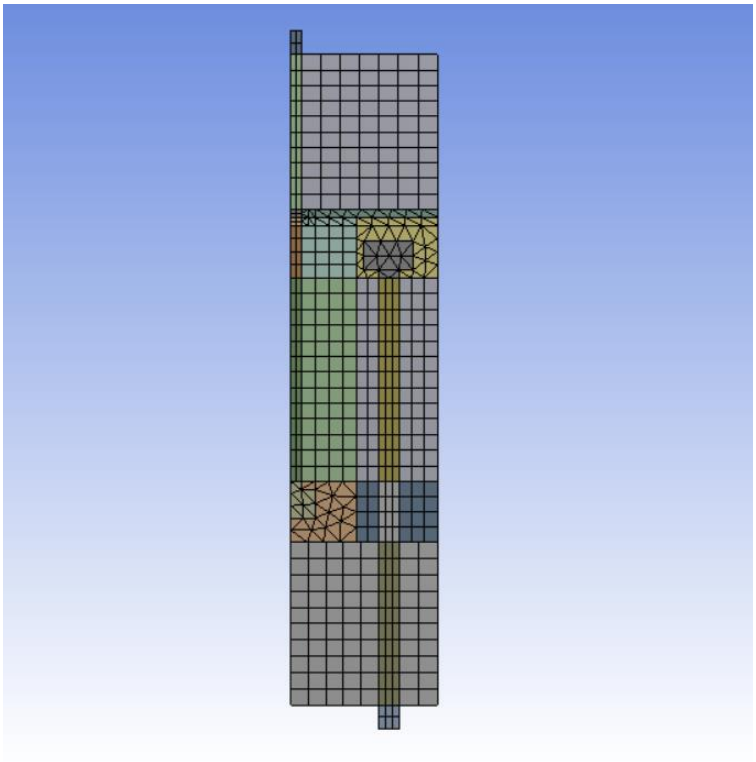

Figure 4.3: Meshing of the quarter scale pullout model.

Frictionless supports were provided at the surfaces at the planes of symmetry. This allowed the nodes at those surfaces to move in the plane of symmetry but restricted their movement normal to the symmetry planes. Constraint equations were used between the coincidental nodes of the steel and the concrete elements to restrict their movement in the normal direction. To control the movement in the tangential direction, i.e., to define the bond-slip relationship, single degree of freedom (DOF) in the tangential direction COMBIN39 elements were introduced between the coincidental nodes. At every 1-inch interval along the length, the quarter of the circumference of the middle rebar had three spring elements attached to it (Figure 4.4). The force versus displacement curve for each spring element was calibrated using the method described in Appendix B (Figure 4.5). For the calibration, bond-slip relations described by Hong et al. 2008 was used, and a simple pullout test was modeled. The results of this pullout test were verified against the experimental values found in the literature. Two nodes on the

middle rebar near the head were monitored for displacement to get the strain at that point. Total force was obtained from the support reactions. From the strain data, force in the head was calculated using the following equation:

$$F_H = A\varepsilon E \tag{4.4}$$

Where F_H = Force in the head, A= cross-section area of the bar, ε= strain and E= modulus of elasticity of the steel. An average total force versus force in the head curve was calculated from the results of the six experiments and the FE model results were compared to that curve. The summary of the results is given in Chapter 5.

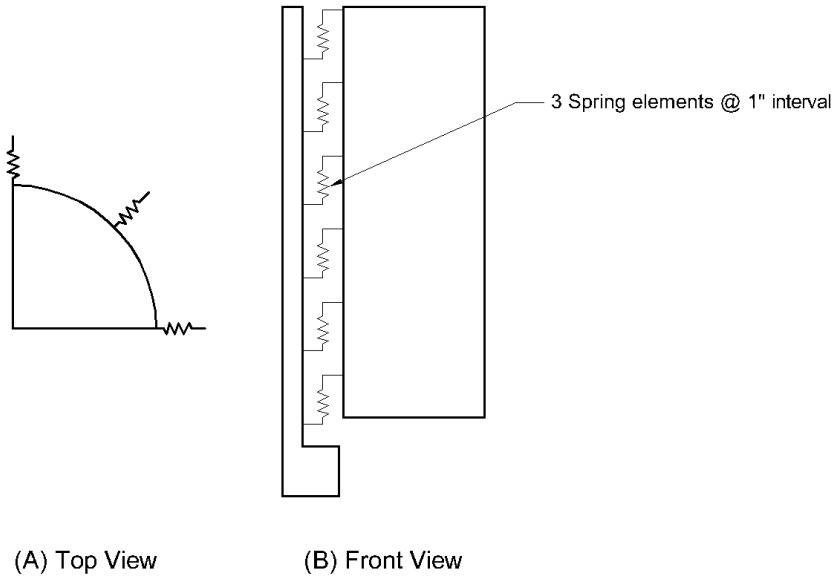

Figure 4.4: Schematic diagram of the placement of COMBIN39 elements.

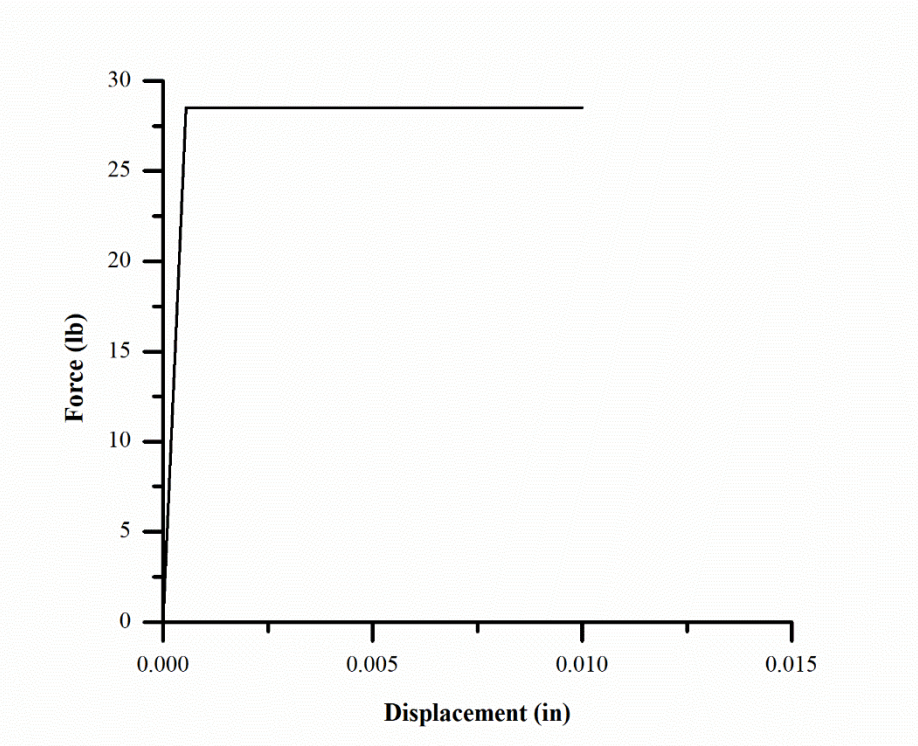

Figure 4.5: Force-Displacement curve used for each spring element.

4.2.2 Beam Tests by Casanova 2018

Some simplifications and modifications to the beam geometry and load placement were done in the FE model for the beam tests. In the experiments, the supports were provided by two 1-inch diameter solid steel rods beneath the beam. Each circular rod was 3 inches inside from the outer face, thus rendering the effective length of the beam to 72 inches. Therefore, the 3D model had a length of 72 inches. Another issue was that, in the three-point bending, the steel plate on the top of the beam has a frictional contact with the beam. That is, the plate and the beam can slide against each other, making different deflections in the beam and the plate possible. In the FE model, the simplest approach would be to assume a perfect bond between the plate and the beam. But in that case, the middle 20 inches of the beam acts as a rigid section, with no noticeable variation of deflection within that region. Using a frictional contact model creates too much nonlinearity in the model and gives birth to convergence issues. A 4-inch

diameter load cell was used on top of the plate in the tests. Considering all these, for the modeling of the three-point bending test, several load placements were modeled:

1. The load was evenly distributed on the steel plate and the steel plate was-
    a. perfectly bonded to the beam
    b. in frictional contact with the beam
    c. in frictionless contact with the beam.
2. The load was at the center of the steel plate over a 4-inch diameter circular area and the steel plate was-
    a. perfectly bonded to the beam
    b. in frictional contact with the beam
    c. in frictionless contact with the beam.
3. There was no steel plate on the beam. The load was defined at the middle on a 4-inch diameter circular area.
4. The load was placed as a concentrated "line load" right at the midspan.

It was found that the third option gave results closest to the experimental values in terms of cracking and ultimate loads. For the other two options, the perfectly bonded ones responded in a very rigid manner; and the other two models of load placements 1 and 2 showed contact instability. On the other hand, placing the load at the midspan produced a more accurate moment versus rebar stress diagram than option 3. However, the ultimate force was lower than the experimental values as the moment arm was longer. The fourth option was preferred because in this case, the moment values are more critical in bridge design than the load values. Figure 4.6 shows the simplified geometry and the loading scheme used in the FE models. All the other components were modeled as the experimental setup.

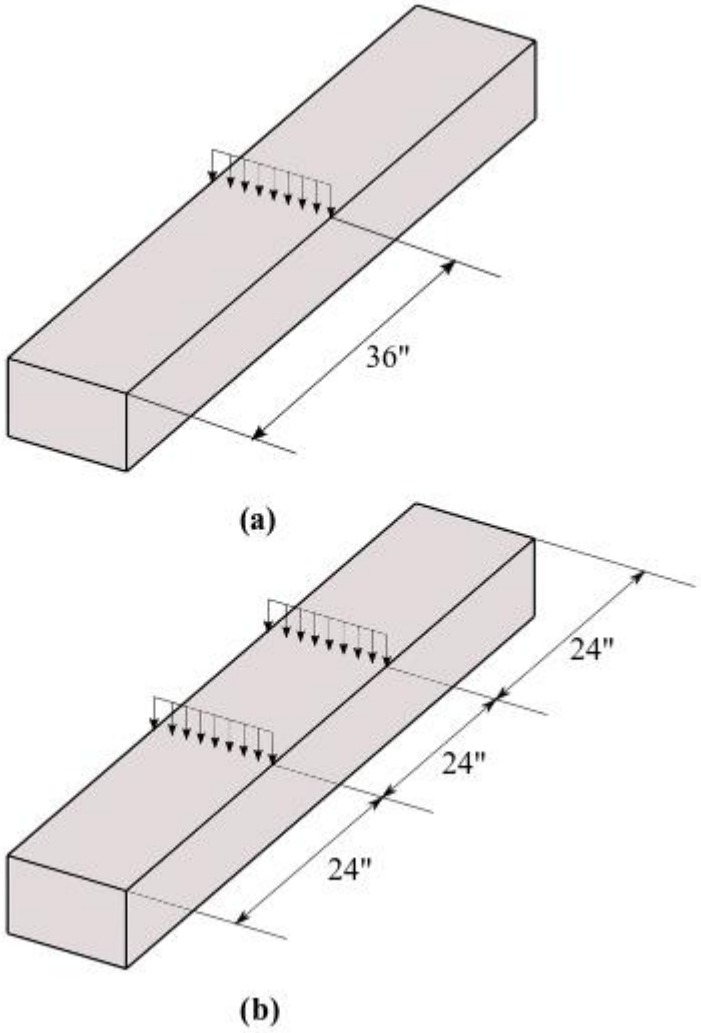

Figure 4.6: Load placements in the FE models of the (a) three-point, and (b) four-point flexural beam tests.

An overview of the modeling attempts is given below:

- The first model consisted of tetrahedral SOLID65 elements and a thin layer of 0.25-inch thickness at the interface. The steel was modeled using SOLID186 elements. This model showed a much stiffer response than the experiments as the SOLID65 elements do not truly open up after cracking.
- The next model also had tetrahedral SOLID65 elements and the thin interface layer. But the steel was modeled using link and beam elements instead of 3D elements. On

two separate cases, the steel rebars were modeled with LINK180 and BEAM188 elements respectively. LINK180 is a 2-node spar element capable of tension and compression. On the other hand, BEAM188 is a 2-node beam element with 6 degrees of freedom at each node (ANSYS Inc., 2016). However, the link and beam elements cannot imitate the anchoring behavior of the headed bars. So, the results were inaccurate.

- In the next model, both the steel and concrete were modeled using SOLID187, a quadratic brick element that has a tetrahedral variation. As the concrete parts were not "sweepable", tetrahedral elements were used and cast-iron material properties were defined for concrete. A bilinear Mode I Cohesive Zone Model was used and the debonding stress was set at 438 psi. The reasoning behind choosing this value is discussed in Appendix B. All other material properties remained the same. The steel bars were perfectly bonded with the concrete. The results obtained from this model will be discussed later in the next chapter.
- Finally, instead of SOLID187, the concrete was modeled with SOLID65 using the smeared crack technique. Bond-slip model between the concrete and the bottom rebars was introduced using the nonlinear spring COMBIN39 elements. Later in this chapter, the details of this model will be discussed.

4.2.2.1 FE Model with No Bond-Slip

As described earlier, this model was built using SOLID187 elements. Cast Iron model was used for concrete. Concrete material properties were the same as the values given in Table 4.2. For the steel, the elastic modulus was 29×10^6 psi, Poisson's ratio was 0.3 and the yield strength was 60 ksi. Simple supports were provided at the two outer edges (pinned at one edge, roller at the other). A ramped load of 15 kips was placed at the locations shown in Figure 4.6. For the three-point bending test, a pressure of 1.193 kips was provided at the center on a circular area

of 4 inches diameter. For the four-point test, 7.5 kips of force was exerted on each of the two indicated locations. Figure 4.7 shows the different parts of the 3D model used for the analyses.

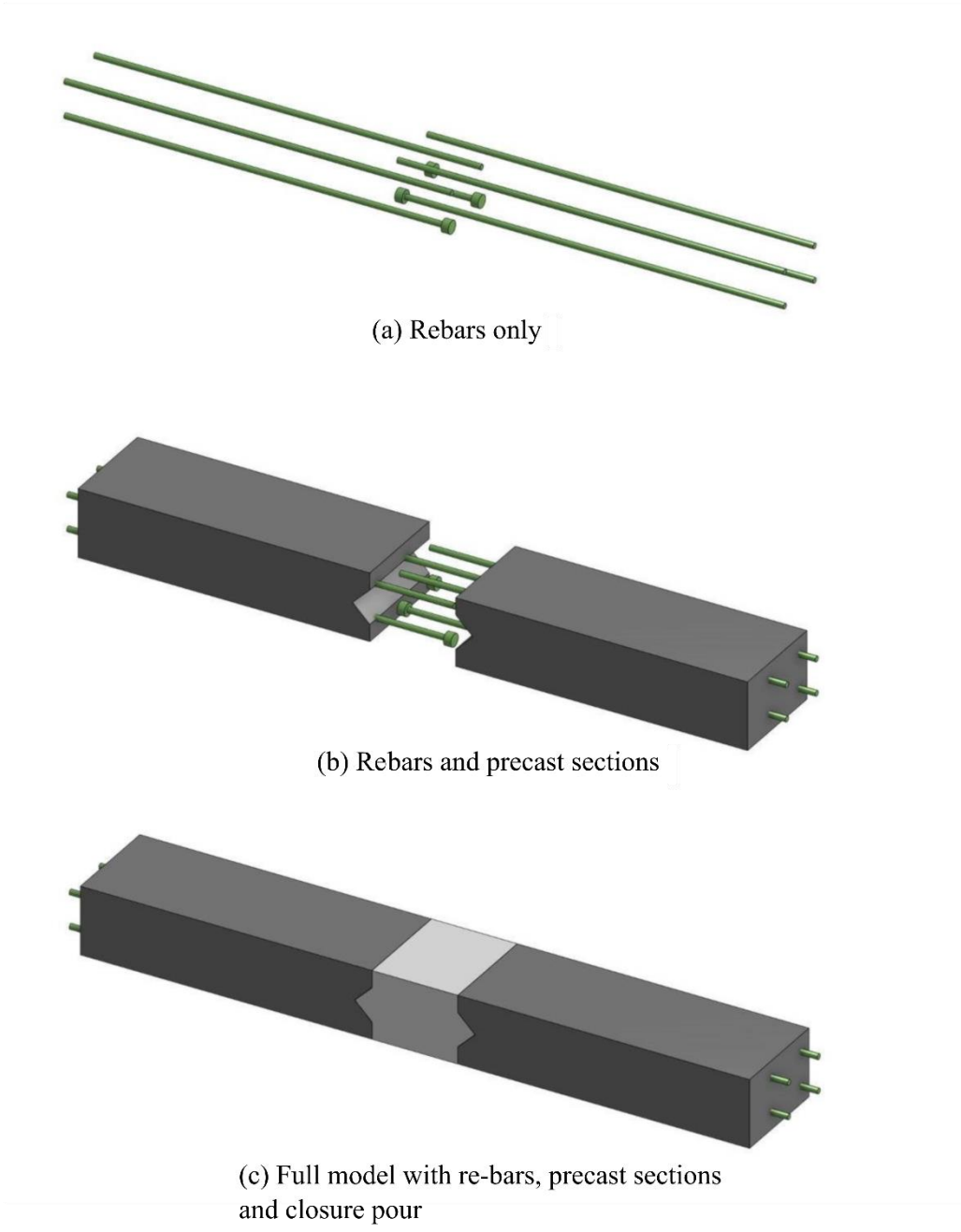

(a) Rebars only

(b) Rebars and precast sections

(c) Full model with re-bars, precast sections and closure pour

Figure 4.7: Different components of the beam 3D model.

4.2.2.2 FE Model with Bond-Slip

In this model, COMBIN39 elements were used to simulate bond-slip. The spring elements were only applied to the bottom bars. As the top portion of the beam is in compression, the upper bars do not take much load. So, their bond-slip was not considered significant and perfect bonding was assumed. The surfaces of the bottom rebars and the surfaces of the voids in concrete that encase the rebars were carefully meshed first so that coincidental nodes could be created between the rebars and the surrounding concrete. For the concrete parts, cracking in tension and plastic yielding in compression were defined using the smeared crack concrete material definition. Figure 4.8 shows the Force vs Displacement curve used for each of the spring elements. The springs were only allowed to move in the direction of the length of the beam. They had no DOF in the other two directions. But this was a bending test. So, if "Large Deflection" was turned on in the ANSYS solution options, it would take the bent shape of the beam into account in each substep. In that case, the displacement of the springs in the other two directions would become significant and the assumptions for the spring elements would have become invalid. To avoid this complication, "Large Deflection" option was turned off.

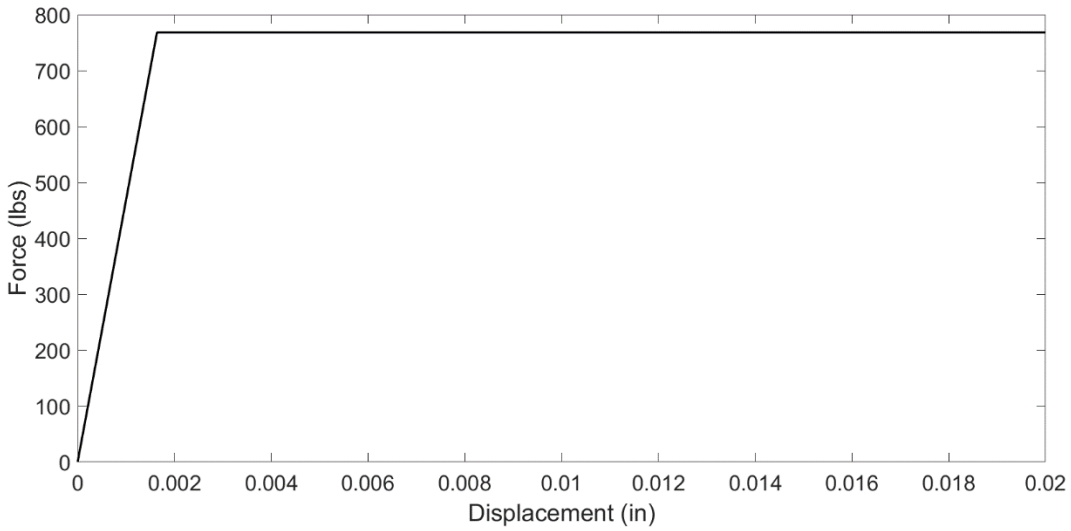

Figure 4.8: Force versus Displacement curve for the springs used in the beam model.

Chapter 5: Results

5.1 Introduction

In this chapter, the results of the models described in Chapter 4 will be presented. The results obtained from the FE models will be compared with the experimental results. Also, the differences in results obtained due to various modeling techniques will be discussed.

5.2 Results of Pullout Tests

Two pullout tests were modeled- one by Delhomme et al. 2016, and another by Casanova 2018. While Delhomme et al. 2016 used PVC sheathing to prevent the bonding between steel and concrete, in the experiments by Casanova 2018, the rebars were bonded to the concrete. Therefore, FE models were developed with perfect bond between steel and concrete, and with bond-slip simulated by nonlinear spring elements for the pullout tests by Casanova 2018.

5.2.1 Test by Delhomme et al. 2016

The displacement at a node at the free end was observed and the total force was found from the support reactions. Then the force versus free end displacement graph was plotted to compare with the experimental results (Figure 5.1).

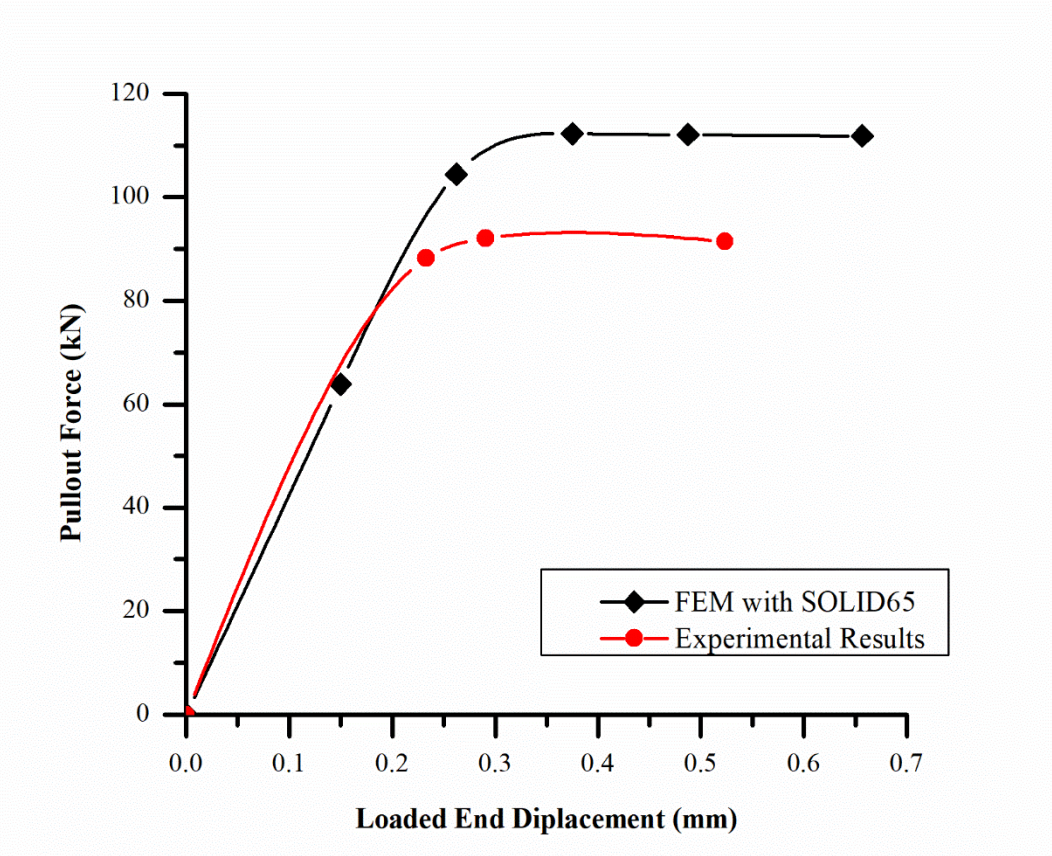

Figure 5.1: Comparison of experimental (Delhomme et al. 2016) and FE model results.

It can be observed from the graph that the finite element model captured the general shape of the curve in a reasonably accurate manner. But it overestimates the ultimate pullout force by about 20%. The crack plot of the model in Figure 5.2, where the cracks are represented by the red circles, shows failure cone near the head at an angle of about 45 degrees, which is in agreement with the observations made by DeVries 1996.

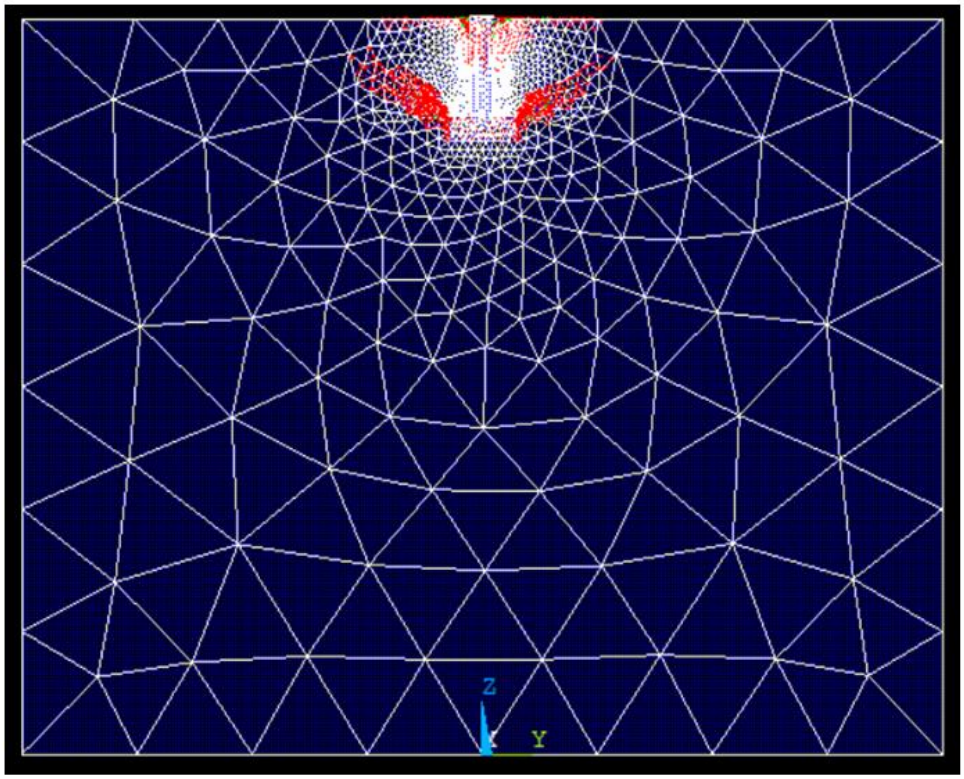

Figure 5.2: Crack plot for the FE model based on experiments by Delhomme et al. 2016.

5.2.2 Tests by Casanova 2018

To compare the effect of bond-slip on the results, the results from the FE model with a thin interface layer and no bond-slip is plotted against the experimental average results in Figure 5.3. It is obvious from the plot that, the FE model shows a stiffer response, especially in the nonlinear region. It is necessary to mention here that, the nonlinearity in this case arises from the tensile cracking of concrete. The pullout failure occurs before the steel yielding. The stiff response in the model with perfect bonding can be explained as a combined effect of two factors:

1. The lack of bond-slip interaction.
2. Interface crack not truly "opening up". The SOLID65 element employs a smeared crack approach. That is, the stiffness is reduced to zero in the direction normal to the crack.

So, this is a “virtual” crack which reduces in strength but does not necessarily show a contact gap.

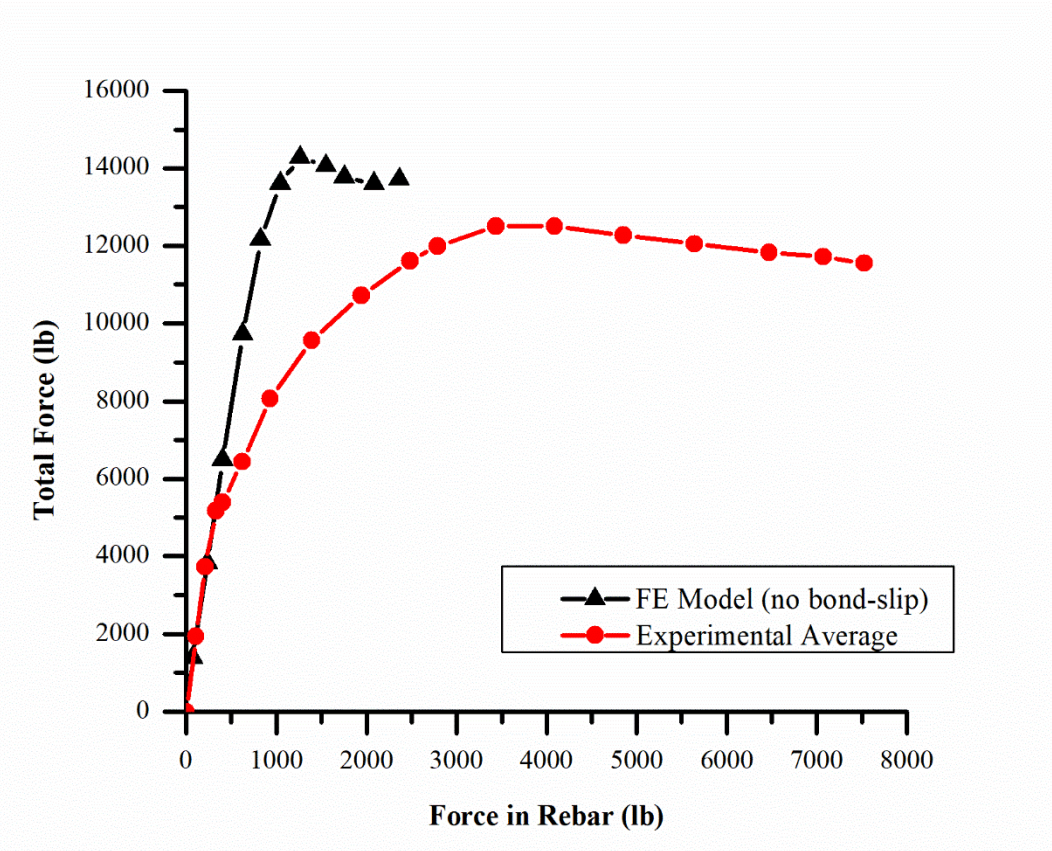

Figure 5.3: Total force versus force in the rebar (FE model with thin interface layer and no bond-slip).

On the other hand, Figure 5.4 shows the improvement in results due to the incorporation of the spring elements and the Cohesive Zone Model. Like other attempts, it is in very good agreement with the experimental results in the linear region. In addition, the nonlinear part also mostly remains inside the spectra of the experimental values.

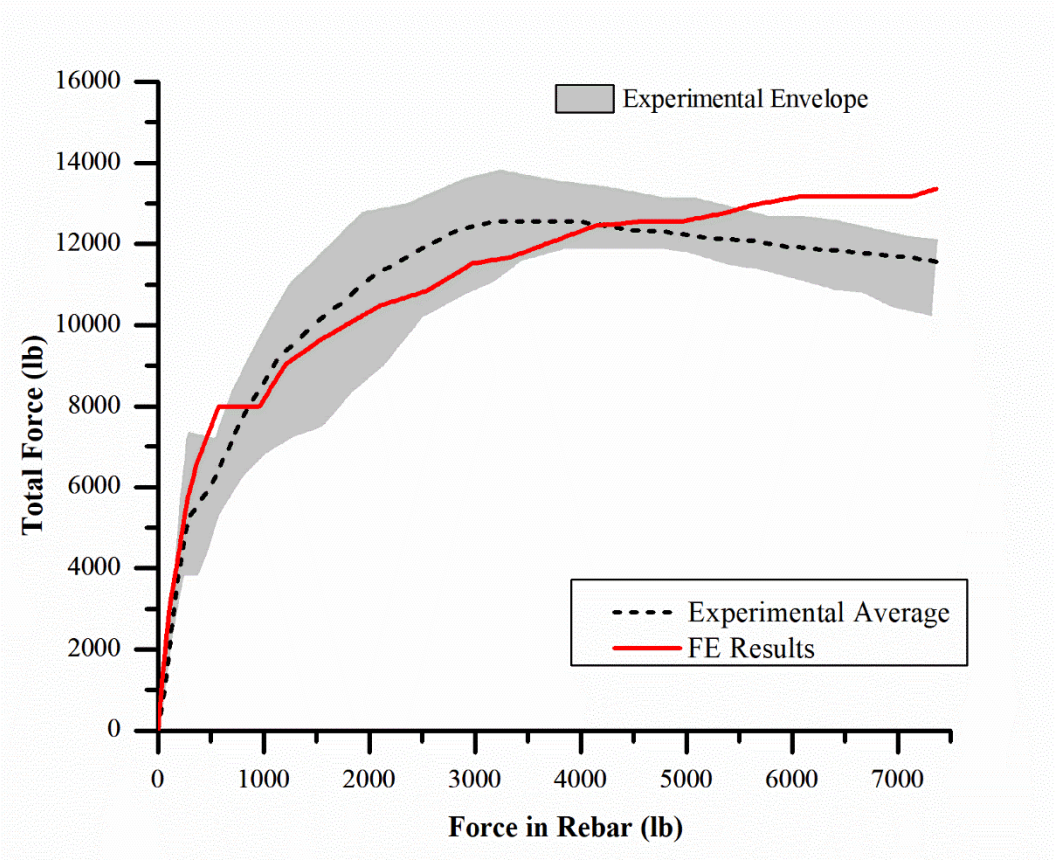

Figure 5.4: Total force versus force in the rebar (FE model with COMBIN39 and CZM).

It can also be noticed from the FE model that, although both the precast and the closure pour concrete crack after reaching their tensile strengths, there is no compressive crushing in concrete. The maximum compressive stress observed in the concrete was 2100 psi, which is significantly less than the compressive strengths of both precast and closure pour. A study of the crack plot shows that it is in agreement with the experimental observations. It can be seen from Figure 5.5 that, a crack started from the top of the specimen near the bar and continued to propagate downward. When the crack reaches the interface, the interface fails quickly, and the previous crack again continues to propagate down towards the head. But the pullout cone cracks near the head were observed in the experiment, which were not found in the FE analysis. In Figure 5.5, the red circles represent primary cracks, while the green and blue circles denote the secondary and tertiary cracks respectively. Also, the orientation planes of the circles

represent the plane of the cracks. The yellow area at the interface zone denotes the failure of the interface at that region. From the figure, it is observed that, the crack propagation is similar and in line with the experimental observation.

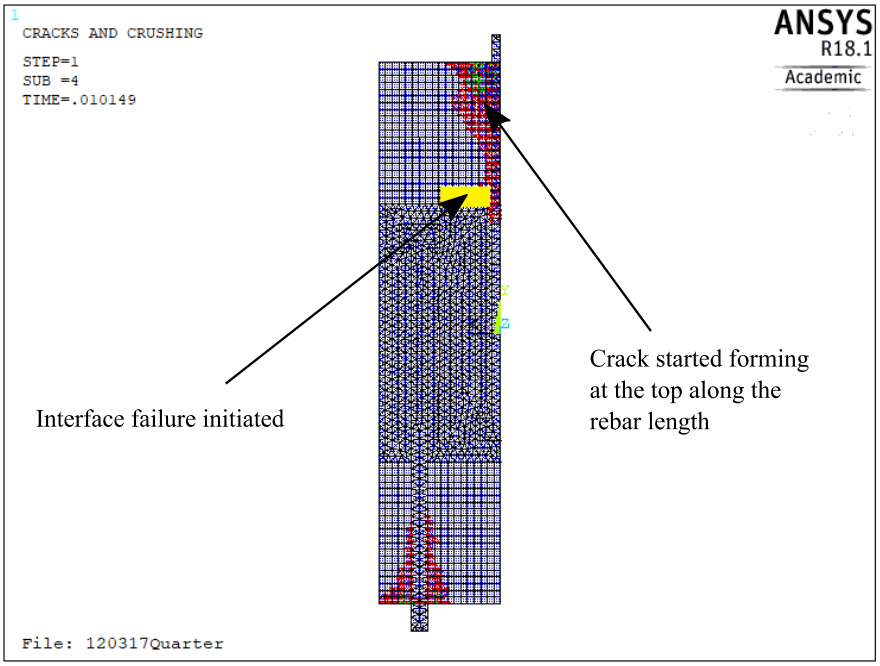

(a) Pullout force= 3,300 lb.

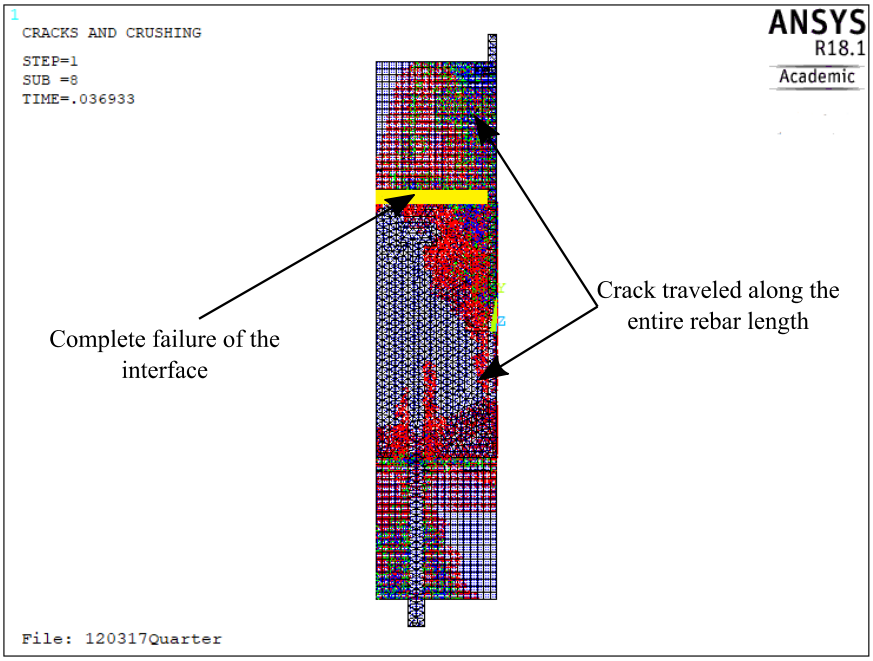

(b) Pullout force= 9,500 lb.

Figure 5.5: Crack propagation in the FE model of the pullout test by Casanova 2018.

5.3 Beam Bending Tests by Casanova 2018

Stresses at two points of the first bottom rebar on the right side were monitored. One of the two points was close to the head, and the other point was right at the interface of precast and closure pour. These stresses were plotted against the moment at the midspan of the beam. When compared to the experimental values, the moment versus rebar stress curves for the model with no bond-slip in Figure 5.6 point to some interesting observations.

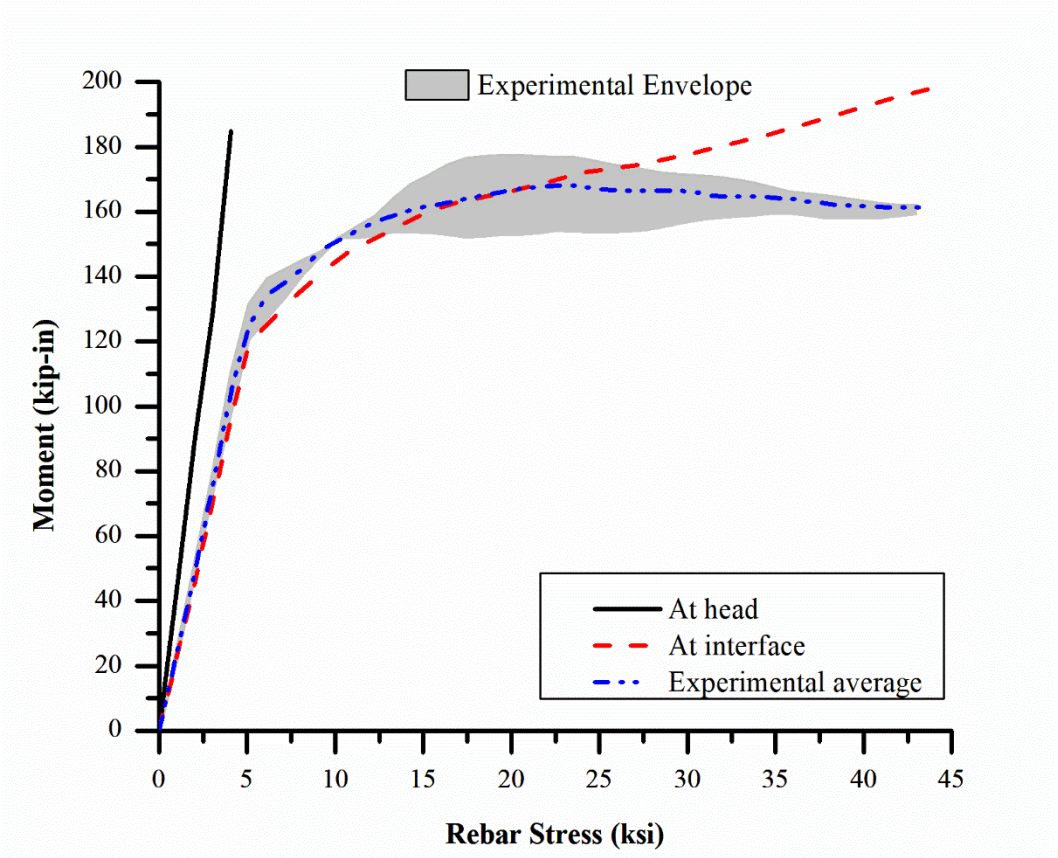

Figure 5.6: Moment vs Rebar stress for three-point bending test (no bond-slip).

Firstly, the stress at the head becomes constant in the FE model after the failure of the interface. This possibly happens due to the perfect bonding between the rebar and the concrete. After the separation of precast and closure pour at the interface, the closure pour section pulls the rebar like a vice. That is why the head does not get a chance to activate its anchoring effect, and no

further stress develops. However, at the interface, the steel is free to stretch and thus start to take more stress. The stress at the interface matches closely with the experimental results. This statement also holds for the four-point bending test, as shown in Figure 5.7. Secondly, the rebar stress at the interface should be greater and more critical. Because after the interface failure, the rebar takes all the load at that region. This is also reflected in Figure 5.6. But these results are not reliable. Because the experimental values were calculated near the head. So, it is evident that, bond-slip behavior plays a crucial part in the beam results.

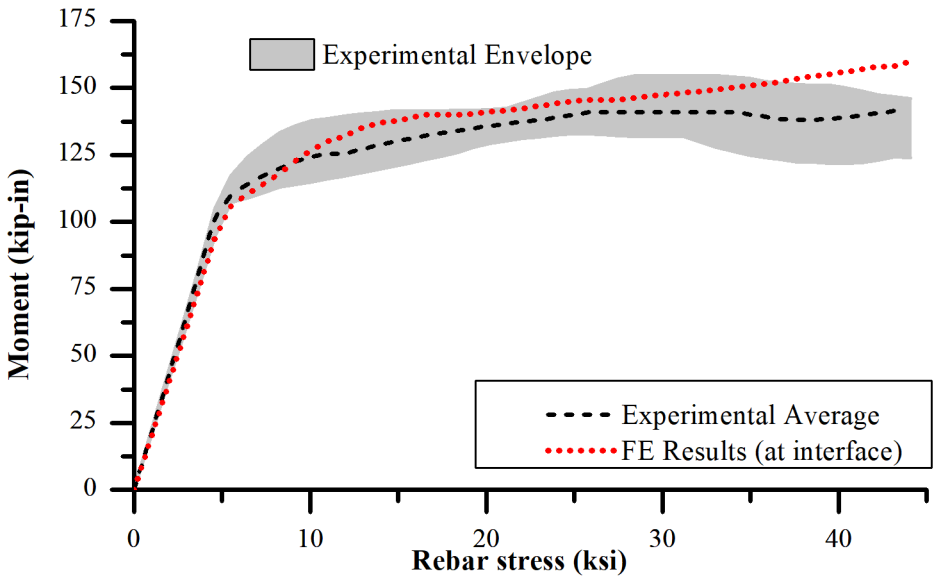

Figure 5.7: Moment vs Rebar stress for four-point bending test (no bond-slip).

Figure 5.8 shows the moment vs rebar stress plot for three-point bending FE model with bond-slip. It can be seen that, the introduction of bond-slip has brought the stress at the head closer to the experimental values. And as expected, the rebar stress at the interface is higher. Similar to the pullout tests, the nonlinearities here are also a combination of geometric and material nonlinearities caused by the interface failure and the cracking of concrete. In the experimental phase, all six specimens cracked at the right-hand side closure to precast interface. Looking at

the crack propagation in the finite element model shown in Figure 5.9, the right-hand side interface opens up more. So, the FE model is in good agreement with the experimental results.

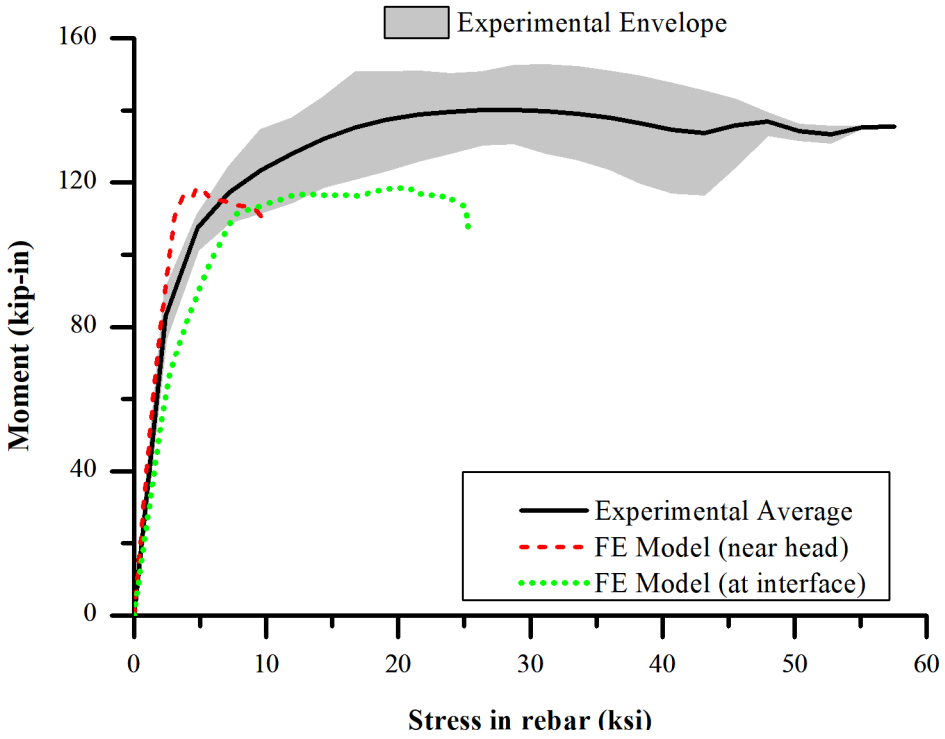

Figure 5.8: Moment versus Rebar stress for three-point bending test (with bond-slip).

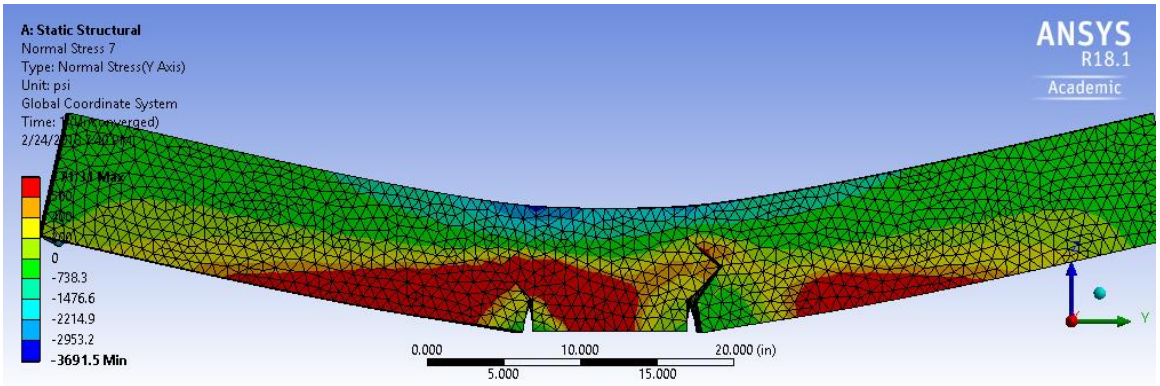

Figure 5.9: Interface crack propagation in the three-point bending test.

The reason why the right-hand side interface cracked every time can be explained by the asymmetric splice configuration of the rebars. In such a short width (12 inches), this

asymmetric condition can create torsion in the beam, which causes the right-hand side interface to crack first. This is also confirmed from Figure 5.10, where it shows that the debonding of the right-hand side interface is occurring first. Furthermore, Figure 5.10 also shows that, after the interface failure in the FE model, concrete cracks form near the shear keys, especially the right-hand side shear key, and travel inwards inside the closure pour. Comparable crack patterns were found in the experiments by Casanova 2018.

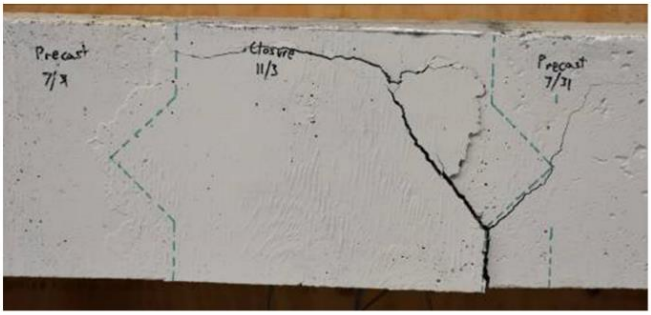

(a) Cracks in the flexural beam test (Casanova 2018)

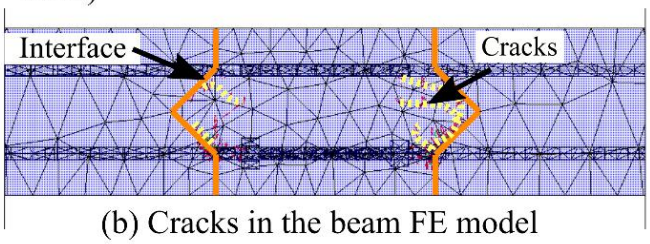

(b) Cracks in the beam FE model

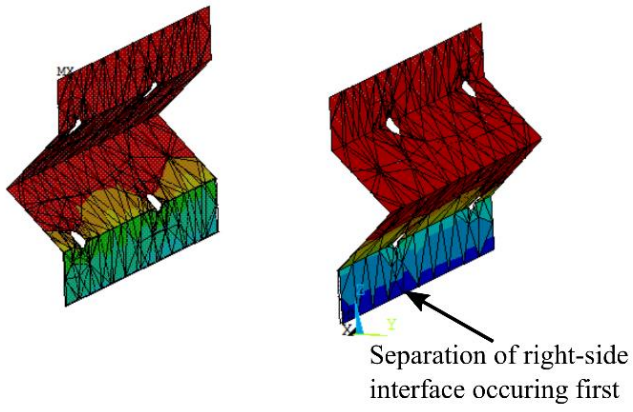

(c) Normal separation of contact elements in the beam FE model

Figure 5.10: Concrete crack patterns in the beam FE model.

Chapter 6: Summary, Conclusions, and Recommendations

6.1 Introduction

A number of modeling options were explored to develop finite element models of pullout of headed rebars in concrete and beam bending tests. Most of the models showed good agreement in the linear region. But there were some issues in the non-linear region of the analysis, especially when the bond-slip response was ignored. These issues and their probable causes are discussed in this chapter. Finally, some recommendations for future studies are made based on the results of the analyses and the issues encountered during the study.

6.2 Summary

- An FE model of the pullout test of headed rebar by Delhomme et al. 2016 was created using the smeared crack approach for concrete. The rebar was not bonded to the concrete. The pullout force versus loaded end displacement curve showed that the FE model matched the experimental results very accurately, especially in the linear region. However, the ultimate pullout force was about 25% higher than the experimental results.
- The pullout test conducted by Casanova 2018 was modeled. First, the FE model was created assuming a perfect bond between the rebar and concrete. While this model was able to replicate the experimental results in the linear region, in the nonlinear region the FE model showed a much stiffer response. Then, the model was improved by using nonlinear spring elements between the rebar and the concrete to simulate the bond-slip response. This improved model showed much better results in the nonlinear region. In both the models, SOLID65 element was used to model concrete. The crack pattern in the FE model was in agreement with the experimental observations. The upper interface

was the first to fail. Another major crack formed at the top of the middle rebar and propagated downwards. The interface was modeled using CZM.

- Finally, FE models were created for the flexural beam tests by Casanova 2018. Like the pullout test, the concrete and the interface were modeled using SOLID65 and CZM respectively. Bond-slip was modeled using COMBIN39 spring elements. The FE results were in good agreement with the experimental ones. The ultimate moment was 15% lower in the FE model than the average ultimate moment found from the experiments. The crack patterns were similar to the experimental observations, where the right interface failed first.

6.3 Discussions on Results

From both pullout models (Delhomme et al., 2016 and ITD Pullout Test) it is evident that the FE models can replicate the linear region very well. The FE model of the ITD pullout test performs even better in the linear region than the FE model of experiments carried out by Delhomme et al., 2016. This is because the material parameters e.g. elastic modulus, Poisson's ratio, tensile and compressive strengths were directly found from experiments, whereas, all the required parameters were not available in the literature for the experiments by Delhomme et al., 2016. This indicates that the linear material models used in the FE models were correct. There were some issues when the FE analyses entered the nonlinear region. The most prominent of these issues was difficulty with convergence. By default, ANSYS employs the Newton-Raphson method to solve non-linear problems. This is an iterative method and ANSYS checks against a force and a displacement criterion in each iteration. Analyses based on displacement convergence criterion only have shown a better performance in terms of convergence. But the stresses in elements can be incorrect in this case as some Newton-Raphson residual forces might remain in the model. Use of contact elements is another key reason for convergence problems. Contact elements increase the node and element count in an

analysis. Moreover, the contact elements themselves have highly non-linear formulation. In comparison, gluing volumes (which merges the coincidental nodes in adjacent volumes) led to better convergence performance. However, gluing volumes results in perfect bonding and does not provide any provision for a bond-slip response. Thus, the head carries less force in the FE model than in the experiment. This is true for both the pullout test and the beam bending test. Again, adding springs to simulate bond-slip means adding more nonlinearity to the model. So careful and novel approaches are necessary in terms of modeling and meshing so that a converged solution can be achieved.

6.4 Recommendations

- Using the splitting tensile strength for all concrete specimens in both the pullout model and the beam model showed a better agreement in terms of the ultimate pullout force. Further studies should be carried out to find which tensile strength is more appropriate to use in the finite element modeling of brittle and granular materials. For ductile materials, it is intuitive to use the direct tensile and compressive strengths. But for materials like concrete, soil etc., it is hard to determine the direct tensile strengths reliably.
- The bond-slip response between steel and concrete can be a significant factor in modeling pullout tests and beam bending tests involving headed reinforcing bars.
- The effect of rib geometry on the bond-slip behavior here were ignored. But from the literature review, it is evident that the rib geometry is one of the main factors that affect the pullout behavior. There were several bond-slip relationships available from the literature that take the effect of bar ribs into account. But the parameters required to use those relationships were not available from the experiments in this case. This is an important issue for future research.

- Observations showed that the brick-shaped element option for SOLID65 produces more accurate results and reduces computation time in comparison to the tetrahedral element option. However, in the regions of high geometric non-linearity, it is very difficult to mesh the volumes with brick-shaped elements. The meshing has to be done carefully so that the maximum number of brick elements can be achieved without making the model too complicated. Using the brick-shaped meshing option whenever it is possible is recommended.
- FE simulations with same modeling parameters but different symmetry conditions in geometry (half model and quarter model) showed no significant variation in results. So, it is viable to take advantage of any symmetry in the specimen to reduce computational effort.
- The flexural beam model performs well in the linear region. It also gives more conservative results in the nonlinear region. Thus, these results can be reasonably used to check against AASHTO Service I and Fatigue I criteria.
- The flexural beam model should be refined and improved to get more accurate results in the nonlinear zone. Modeling the beam FE model for torsional and cyclic loading could be another avenue to explore.
- It is important to bear in mind that, the nonlinearities in the pullout tests and the bending tests arise from the cracking of concrete and the failure of the interface, rather than the yielding of the steel. In other words, they are true geometric discontinuities. While the CZM method used for the interfaces can treat the "delamination" or the cracking as true geometric discontinuities, the smeared crack approach used for the concrete cannot. Thus, the models developed here are not suitable for the study of load-deflection behavior or the development of shear degradation models.

References

Abrams, D. A. (1913). “Tests of Bond Between Concrete and Steel.” *Bulletin No. 71, Engineering Experiment Station, University of Illinois, Urbana*.

ACI Committee 318. (2008). *Building Code Requirements for Structural Concrete (ACI 318-08). American Concrete Institute*.

ANSYS Inc. (2013). “Mechanical APDL Theory Reference (Version 14).” Cannonsburg, PA.

ANSYS Inc. (2016). “ANSYS User Manual (Version 18).” ANSYS Inc., Cannonsburg, PA.

Casanova, M. (2018). “Mechanical behavior of high early strength concrete with polypropylene fibers for field-cast connections of bridge precast elements.”, MS Thesis Idaho State University, Pocatello, ID.

Catalano, D. M. (1983). *Concrete fracture--a linear elastic fracture mechanics approach*. Cornell University, January.

Cox, J. V, and Herrmann, L. R. (1998). “Development of a plasticity bond model for steel reinforcement.” *Mechanics of Cohesive-frictional Materials*, 3(2), 155–180.

Dahl, C. L. (1995). *Strekkforbindelse med t-hodestenger*. Trondheim, Norway.

Delhomme, F., Roure, T., Arrieta, B., and Limam, A. (2016). “Pullout behavior of cast-in-place headed and bonded anchors with different embedment depths.” *Materials and Structures/Materiaux et Constructions*.

DeVries, R. A. (1996). “Anchorage of headed reinforcement in concrete.” University of Texas at Austin, TX.

Dinges, D. (1983). *Untersuchung verschiedener Elementsteifigkeitsmatrizen auf ihre Eignung zur Berechnung von Stahlbetonkonstruktionen: dritter Zwischenbericht zum*

Forschungsvorhaben" Nichtlineare Berechnungen im konstruktiven Ingenieurbau. Univ. Kassel, Fachgebiet Massivbau, Darmstadt, Germany.

Doerr, K. (1980). "Ein Beitrag zur Berechnung von Stahlbetonscheiben unter besonderer Berucksichtigung des Verbundverhaltens." Technischeltoch Schale, in Darmstadt, Germany.

Drucker, D. C., and Prager, W. (1952). "Soil mechanics and plastic analysis or limit design." *Quarterly of applied mathematics*, 10(2), 157–165.

Ebrahimpour, A., Mashal, M., Casanova, M., Rashique, U., Clauson, C., and Shokrgozar, A. (2018). *Effectiveness of High-Early Strength Concrete Class 50AF with Polypropylene Fibers as a Cost-Effective Alternative for Field-Cast Connections of Precast Elements in Accelerated Bridge Construction*. Boise, ID.

Eligehausen, R. (1996). *Bericht über Zugversuche mit Deha Kopfbolzen (Report on pull tests on Deha anchor bolts). Institut für Werkstoffe in Bauwesen, University of Stuttgart*. Report No. DE003/01-96/32, September (Research carried out on behalf of Deha Ankersystene, GMBH & Co., Gross-Gerau, Germany), Stuttgart, Germany.

Eligehausen, R., Popov, E. P., and Bertero, V. V. (1982). "Local bond stress-slip relationships of deformed bars under generalized excitations."

Feldman, L. R., and Bartlett, F. M. (2005). "Bond strength variability in pullout specimens with plain reinforcement." *ACI Structural Journal*.

Fynboe, C. C., and Thorenfeldt, E. (1986). *T-Headed Bars, SP1: Static Pullout Tests. SINTEF test report STF65 F86083*, SINTEF, Trondheim, Norway.

Ghali, A., and Youakim, S. A. (2005). "Headed studs in concrete: state of the art." *ACI Structural Journal*, 102(5), 657.

Goto, Y. (1971). “Cracks formed in concrete around deformed tension bars.” *Journal of American Concrete Institute*, 244–251.

Graybeal, B. A. (2014). “Design and Construction of Field-Cast UHPC Connections.” *FHWA*.

Graybeal, B. A. (2017). *Design and construction of field-cast UHPC connections (FHWA-HRT-14-084)*. McLean, VA.

Hertanto, E. (2005). “Seismic assessment of pre-1970s reinforced concrete structure.” University of Canterbury, Christchurch, New Zealand.

Hjelm, H. E. (1994). “Yield surface for grey cast iron under biaxial stress.” *Journal of Engineering Materials and Technology*, American Society of Mechanical Engineers, 116(2), 148–154.

Hong, S.-G., Park, J. M., Kim, T. W., Park, S. K., and Ko, W. J. (2008). “Bond stress-slip relationship in reinforced concrete: new relationship and comparative study.” *33rd Conference on OUR WORLD IN CONCRETE & STRUCTURES*, Singapore.

Hoshino, M. (1974). *Ein Beitrag zur Untersuchung des Spannungszustandes an Arbeitsfugen mit Spanngliedkoppelungen von abschnittsweise in Ortbeton hergestellten Spannbetonbrucken*. Studentenwerk.

Ingraffea, A. R., Gerstk, W. H., Gergely, P., and Saouma, V. (1984). “Fracture mechanics of bond in reinforced concrete.” *Journal of Structural Engineering*, 110(4), 871–890.

Keuser, M., and Mehlhorn, G. (1988). “Finite Element Models for Bond Problems.” *Journal of Structural Engineering*, 113(10), 2160–2173.

Kim, J. J., and Reda Taha, M. (2014). “Experimental and numerical evaluation of direct tension test for cylindrical concrete specimens.” *Advances in Civil Engineering*.

De la Varga, I., and Graybeal, B. A. (2016). *Dimensional Stability of Grout-Type Materials Used as Connections for Prefabricated Bridge Elements (FHWA-HRT-16-008)*. McLean, VA.

De la Varga, I., Haber, J. B., and Graybeal, B. A. (2016). "Performance of grouted connections for prefabricated bridge elements-part I: material-level investigation on shrinkage and bond." *PCI National Bridge Conference*, Nashville, TN.

Leonhardt, F., and Walther, R. (1965). "Welded Wire Mesh as Stirrup Reinforcements–Shear Tests on T-Beams and Anchorage Tests." *Bautechnik*, 42(10).

Lutz, L. A., and Gergely, P. (1967). "Mechanichs of Bond and Slip of Deformed Reinforcement." *ACI Journal*, 711–721.

Martin, H. (1973). "Zusammenhang zwischen Oberflächenbeschaffenheit, Verbund und Sprengwirkung von Bewehrungsstählen unter Kurzzeitbelastung." *Deutscher Ausschuss für Stahlbeton*, (228).

Mathey, R. G., and Watstein, D. (1961). "Investigation of bond in beam and pull-out specimens with high-yield-strength deformed bars." *Journal of American Concrete Institute*, 57(3).

Ngo, D., and Scordelis, A. C. (1967). "Finite element analysis of reinforced concrete beams." *Journal of American Concrete Institute*, 64(3), 152–163.

Nilson, A. H. (1972). "Internal measurement of bond slip." *Journal of American Concrete Institute*, 439–441.

Perry, E. S., and Thompson, J. N. (1966). "Bond Stress Distribution on Reinforcing Steel in Beams and Pullout Specimens." *ACI Journal Proceedings*, 63(8), 865–876.

Petersson, P.-E. (1981). "Crack growth and development of fracture zones in plain concrete and similar materials." Lund Institute of Technology, Skane, Sweden.

Rao, G. A., Pandurangan, K., Sultana, F., and Eligehausen, R. L. B. (2007). "Studies on the pull-out strength of ribbed bars in high-strength concrete." *proceeding, FraMCos-6 conference. International Association of Fracture Mechanics for Concrete and Concrete Structures. Part*, 5–17.

Rehm, G. (1961). "Ueber die Grundlagen des Verbundes zwischen Stahl und Beton. Deutcher Ausschuß für Stahlbeton (DAf St), 138, 1961." German.

Riks, E. (1979). "An incremental approach to the solution of snapping and buckling problems." *International Journal of Solids and Structures*.

Ru-deng, L. U. O. (2008). "Values of shear transfer coefficients of concrete element Solid65 in Ansys [J]." *Journal of Jiangsu University (Natural Science Edition)*, 2, 18.

Schäfer, H. (1975). "A contribution to the solution of contact problems with the aid of bond elements." *Computer methods in applied mechanics and engineering*, 6(3), 335–353.

Shima, H. (1986). "Micro and macro models for bond behavior in reinforced concrete." University of Tokyo, Tokyo, Japan.

Swenty, M. K., and Graybeal, B. A. (2013). *Material characterization of field-cast connection grouts.* United States. Federal Highway Administration. Office of Infrastructure Research and Development.

Tepfers, R. (1979). "Cracking of concrete cover along anchored deformed reinforcing bars." *Magazine of concrete research*, 31(106), 3–12.

Thompson, M. K., Ledesma, A., Jirsa, J. O., and Breen, J. E. (2006). "Lap splices anchored by headed bars." *ACI structural journal*, 103(2), 271.

Willam, K., and Warnke, E. (1975). "Constitutive model for the triaxial behavior of concrete." *International Association for Bridge and Structural Engineering*.

Wright, J. L., and McCabe, S. L. (1997). *The Development Length and Anchorage Behavior of Headed Reinforcing Bars*. University of Kansas Center for Research, Inc.

Xing, G., Zhou, C., Wu, T., and Liu, B. (2015). "Experimental study on bond behavior between plain reinforcing bars and concrete." *Advances in Materials Science and Engineering*, 2015.

Appendix A: Verification of the Concrete Model

A.1 Introduction

The first step for modeling the pullout tests was to decide on suitable modeling techniques. It was deemed convenient to use the SOLID65 element along with the William-Warnke criterion for modeling concrete, because of the element's cracking capability. The next step was to run a simple verification test to see whether the model developed using SOLID65 can produce accurate results.

A.2 Verification Procedure

For the purpose of concrete model verification, at first a solid concrete block was modeled with a 1-inch x 1-inch cross-section and a height of 10 inches. The concrete properties used are given in Table A.1:

Table A.1: Material properties used in the verification model.

Elastic Modulus (psi)	Poisson's Ratio	Compressive Strength (psi)	Tensile Strength (psi)
6.6×10^6	0.2	12000	835

The SOLID65 element needs two additional parameters namely open shear and closed shear transfer coefficients. These two values represent the transfer of shear force between two surfaces of a crack in open and closed conditions. The permissible values are from 0 to 1. The value of 0 means no shear transfer i.e. a perfectly smooth crack. The shear transfer increases with an increasing value meaning rougher crack surfaces. However, previous studies like Ru-deng 2008 and some preliminary simulations led to the observation that a value smaller than 0.2 for open shear transfer coefficient can cause convergence issues. That is why the values for open and closed shear transfer coefficients used were 0.25 and 0.95 respectively. A value of -1 was input for uniaxial crushing strength, which turns off the crushing capability in

compression. This also helps to reduce the difficulties with convergence. Instead, a bilinear elastic-perfectly plastic model was used for compression. However, the tension cracking capabilities were turned on. The bottom of the specimen was fixed and tensile and compressive loads were applied on the top surface in turns. Then the stress and strain at anode at the middle of the specimen were observed. It was found that the model behaved reasonably well in compression. The output stress-strain curve almost exactly matched the input for compressive stress-strain curve. But with tensile cracks being turned on, it was expected that the stress will drop to zero after reaching the tensile strength and stay at that value. But the results showed the stress dropped, but did not reach zero, and also, the stress value did not remain stable after that point, as shown in Figure A.1. A careful analysis of the results showed that there was a stress concentration at the bottom near the support. Concrete at only that region cracked and the concrete at the middle did not get a chance to crack. To overcome this issue, another model was prepared. The model was 30 inches long with cross sections of 1.5 in x 1.5 in at the top and bottom surfaces. The cross sections slowly tapered, and the middle 10 inches became 1 in x 1 in. This model could eliminate the stress concentration at the support and force the cracks to happen at the middle 10 inches. All other parameters for the analysis stayed the same. Figure A.2 shows the crack patterns in the specimen. Each element of SOLID65 can crack in three planes and the primary, secondary and tertiary cracks are represented by red, green and blue circles respectively.

The compressive and tensile stress-strain curves are shown in Figures Figure A.3 and Figure A.4 respectively. It can be seen that the model performed very well in both compression and tension.

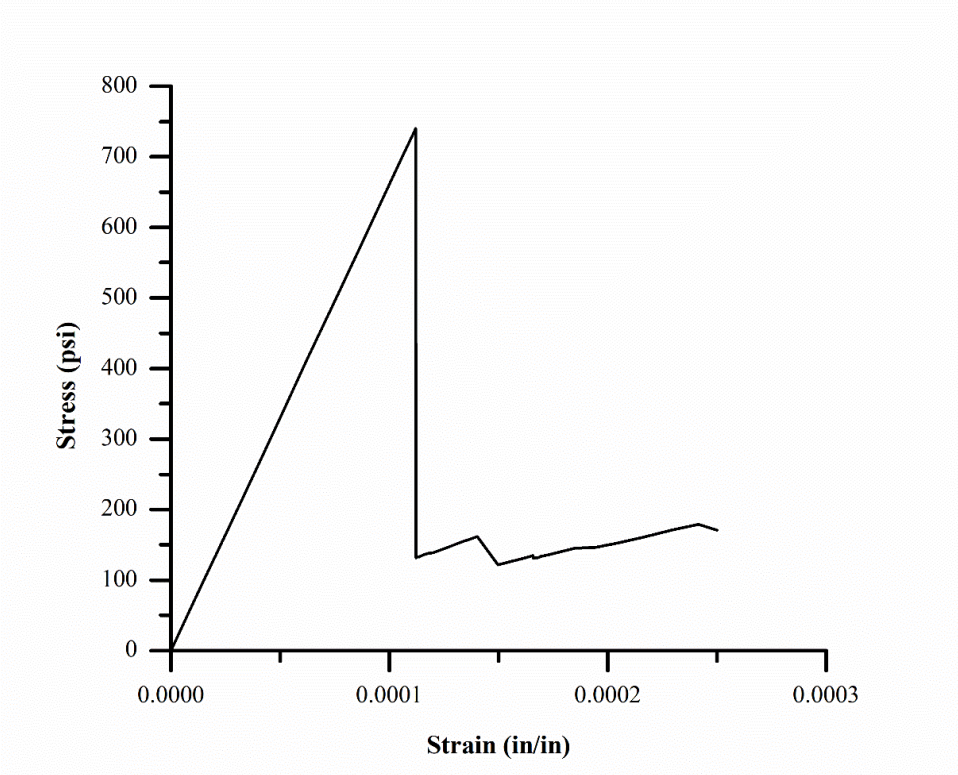

Figure A.1: Tensile stress-strain diagram of the uniform concrete model.

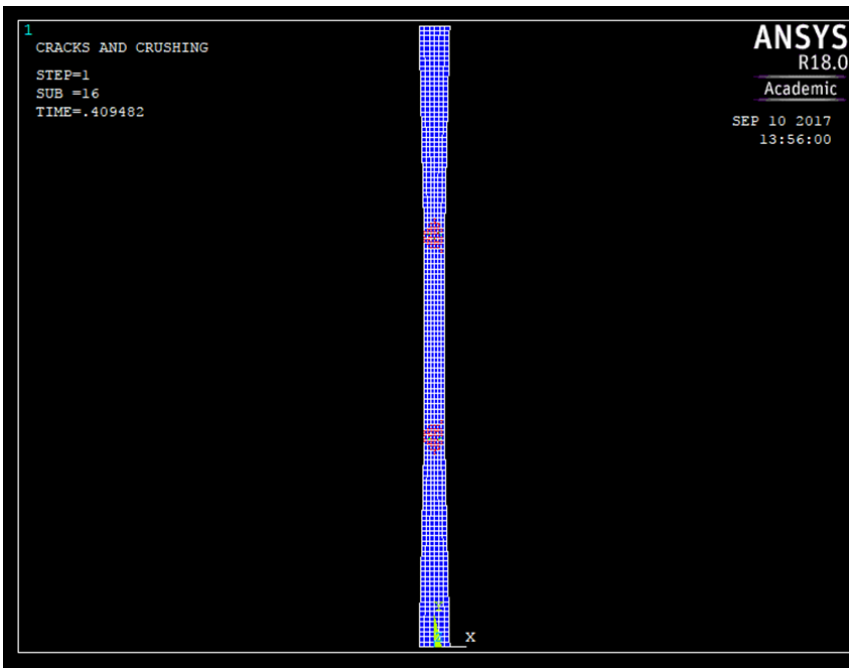

Figure A.2: Crack plot in the tapered concrete model.

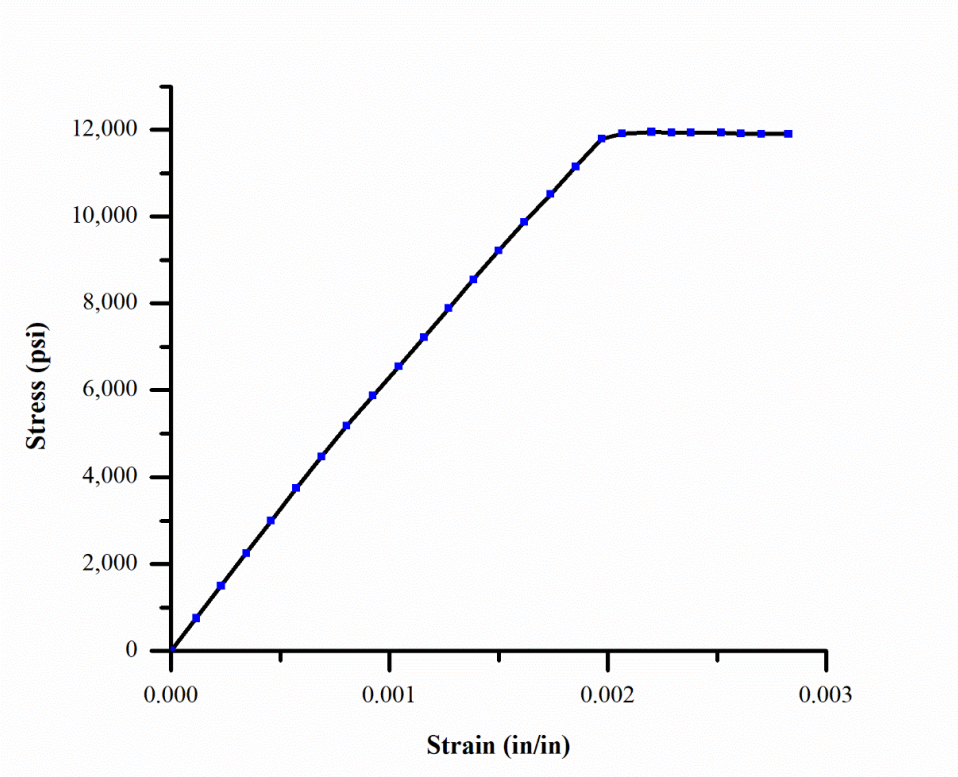

Figure A.3: Compressive stress-strain diagram for the tapered model.

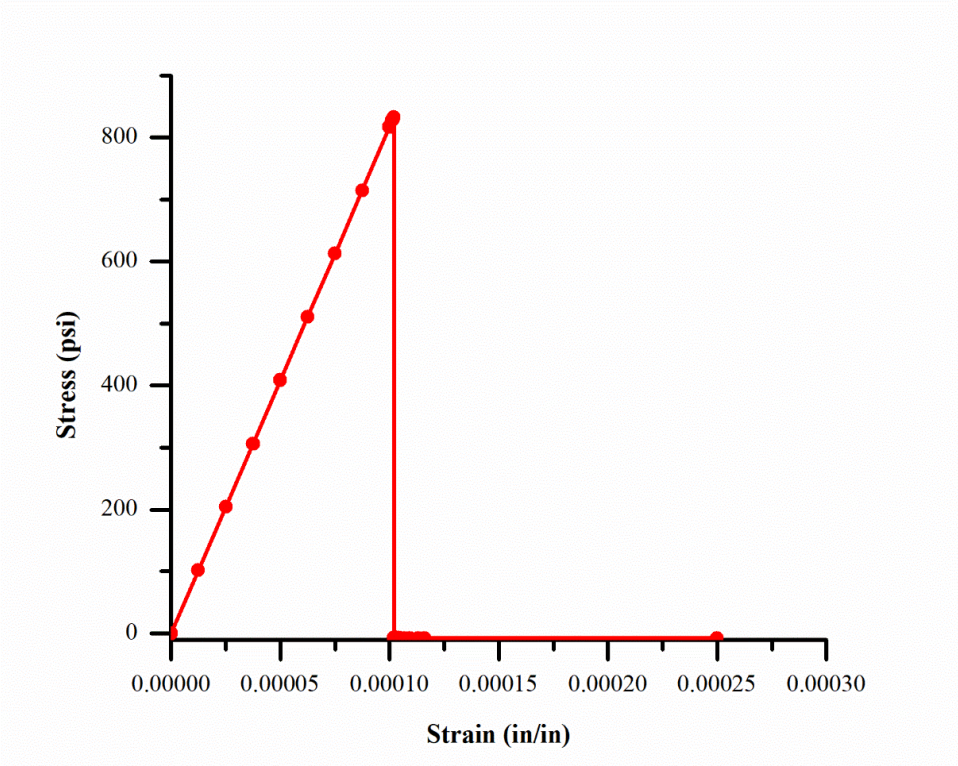

Figure A.4: Tensile stress-strain diagram for the tapered model.

Appendix B: Calibration and Verification of Contacts and Bonds

B.1 Introduction

As numerous factors affect the pullout behavior of rebars in concrete, establishing a precise bond-slip relationship is very difficult without experimental studies on a case-by-case basis. However, attempts have been made to develop mathematical models to represent the steel-concrete bond-slip behavior. For example, Shima 1986 proposed the following bond-slip relationship for long embedment length (more than 25 times the bar diameter):

$$\tau_b = 0.9f'_c[1 - exp - 40(S/d_s)^{0.6}] \quad \textbf{(B.1)}$$

Where, $\tau_b =$ bond shear stress (psi), $f'_c =$ concrete compressive strength (psi), $S =$ slip (in.), and $d_s =$ bar diameter (in.). In this chapter, the bond-slip model will be verified using this equation.

B.2 Steel-Concrete Bond-Slip Model Verification

For the verification of the bond-slip model, the experimental data from the studies conducted by Rao et al. 2007 was used. To define the stiffness of the spring elements that were used to model the interface between the rebar and the concrete, Eq. (B.1) was used. The verification of the bond-slip model consists of two parts:

1. Verification of Eq. (B.1) proposed by Shima 1986.
2. Verification of the FE model.

B.2.1 Verification of Eq. (B.1)

The equation needs two parameters- the compressive strength of the concrete and the bar diameter. Rao et al. 2007 used a 6 in x 6 in x 6 in concrete cube with a compressive strength of

5800 psi, and a #5 rebar at the center with 6 inches bond length. Putting $f'_c = 5800$ psi, and $d_b = 0.625$ inch in Eq. (B.1), the bond stress versus slip diagram was plotted and compared to the experimental results obtained by Rao et al. 2007 in Figure B.1. Note that, the equation cannot capture the softening of bond after reaching the peak bond stress. However, this limitation was observed to have a negligible effect on the results obtained from the FE models of the pullout test and the flexural beam tests. Other than that, the values are in good agreement.

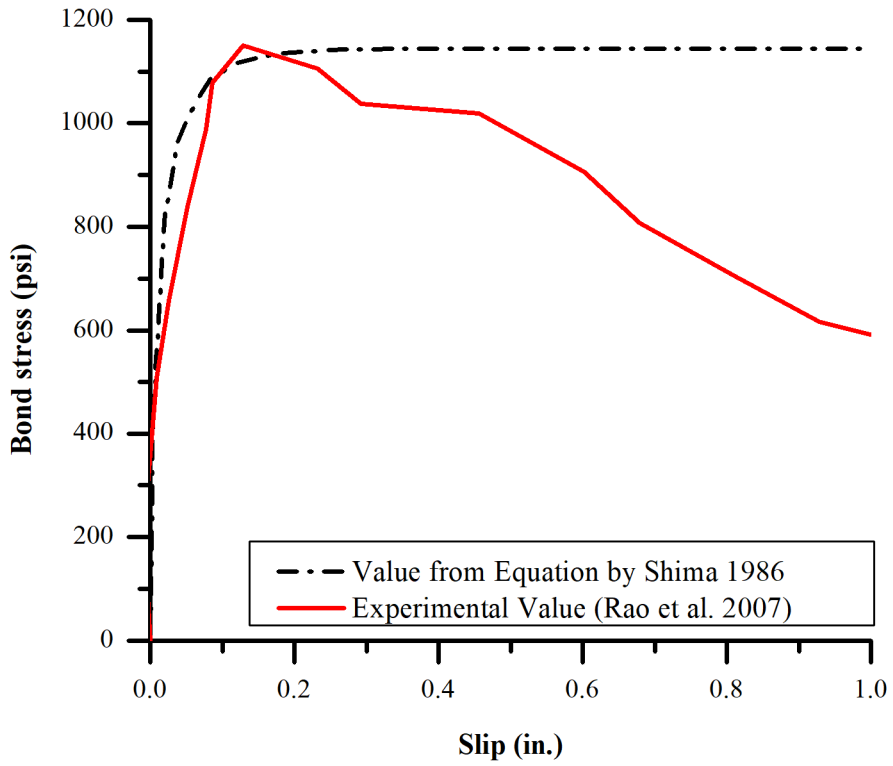

Figure B.1: Verification of the equation by Shima 1986.

B.2.2 Verification of the FE Model

A quarter-model utilizing the symmetry of the test specimen used by Rao et al. 2007 was created, as shown in Figure B.2. 21 spring elements were defined between the rebar and the concrete, i.e., 3 spring elements at 1-inch interval along the 6 inches bond length. The bond

stress versus slip curve was already obtained using Eq. (B.1). The stress values were multiplied by the total bond surface area to get the force values. Finally, the force values were divided by 21 to get the force versus displacement curve for one spring element. This curve was used to define the real constant for the COMBIN39 element. The force versus displacement curve used for each spring element is shown in Figure B.3.

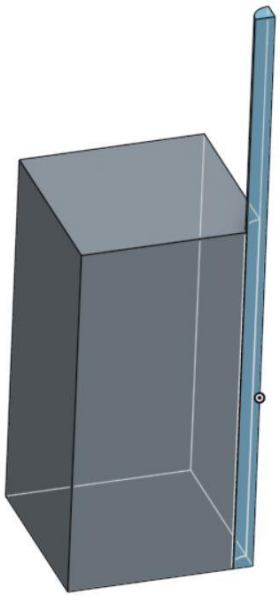

Figure B.2: Quarter FE model of the pullout test by Rao et al. 2007.

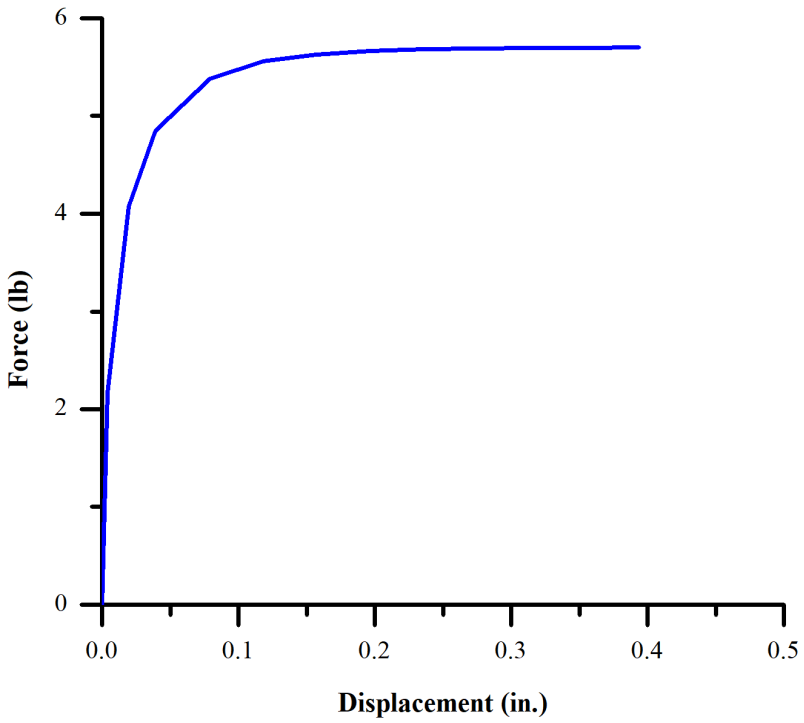

Figure B.3: Force-Displacement relation used for each spring element.

Two top edges that were not part of the two planes of symmetry were fixed, and a ramped displacement of 1.5 inches upward was applied on the top of the bar. Displacements of two nodes, one belonging to the rebar at the top of the embedment, and another belonging to the concrete at the same location were monitored. The difference between the two displacements gave the slip value. The total reaction at the fixed support represented the pullout force. This force values were used to calculate the bond shear stresses. In Figure 2.11, the stress versus slip values obtained from the FE model were compared against the values from Eq. (B.1) and experimental values obtained by Rao et al. 2007. Observe that, although the response from the FE model is a little "softer", it is still in agreement with the experimental data to an agreeable level. Thus, it can be inferred that this modeling technique can be effectively used in the models of the pullout test and the beam bending tests. Furthermore, as no "softening" was defined in

the real constant for the COMBIN39 element, the FE model curve also becomes horizontal after reaching the peak bond stress. However, a slight downward trend can be observed. This is possibly due to the failure of the concrete elements attached to the springs.

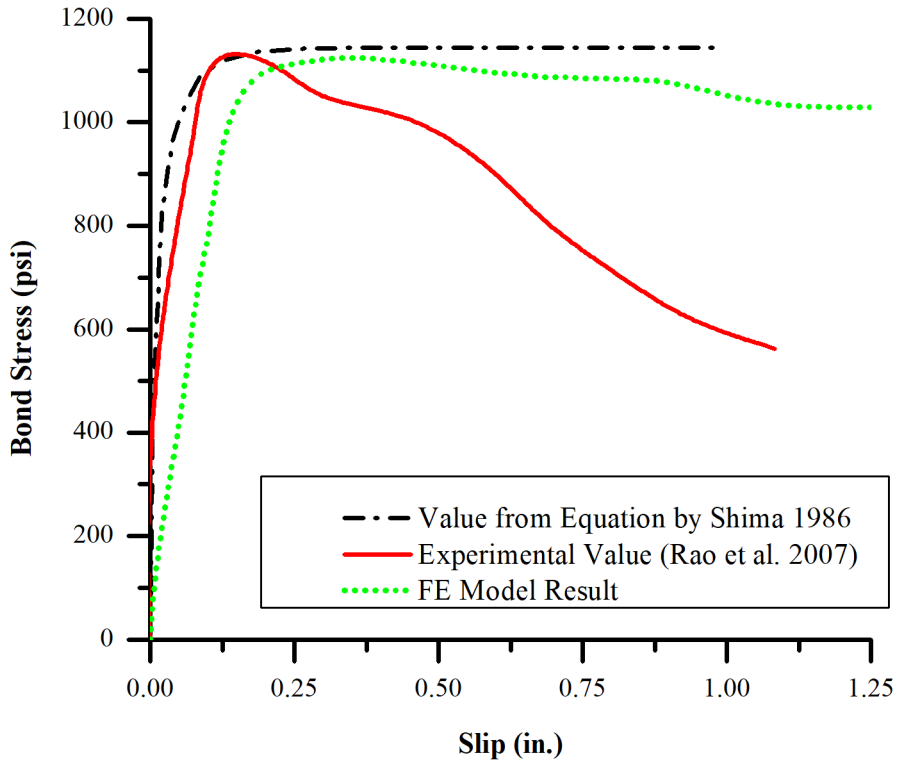

Figure B.4: Verification of the pullout FE model.

B.3 Concrete- Concrete Interface Model Calibration

A full-scale FE model was created based on the experiments done by Casanova 2018 to determine the modulus of rupture of the precast-closure interface. The model was a rectangular beam of 18 inches length and a cross section of 6 inches x 6 inches. The beam was composed of two 9-inch sections- one made of the closure pour material, and the other one made of the precast concrete. The beam was subjected to a 4-point bending test. The schematic of the test is given in Figure 2.15.

Boundary conditions similar to the experiments were applied to the FE model. The load was applied as displacements. For the material properties, the concrete portions were modeled as linear elastic materials. From the experiments, it was evident that the specimens fail at the interface only. No cracks were observed in the concrete matrix. So, in the FE model, only defining the elastic properties should suffice. Separation- Distance based CZM material was defined for the interface. From the experiments, the average modulus of rupture for the interface was found to be 612 psi. From Eqs. (4.1) and (4.2), the splitting tensile strength can be calculated as 438 psi. Now, Mode I CZM was used, that debonds only due to normal stress. For this mode, three inputs are required- maximum normal stress, contact gap at the completion of debonding, and artificial damping coefficient. Artificial damping coefficient has the unit of time and should be smaller than the smallest step size defined in the analysis. In this analysis, a minimum step size of 0.0001 s was used. The damping coefficient was defined as 0.00001 s. Now, the total force required for delamination is a function of the other two parameters. Here, keeping the maximum normal stress constant at 438 psi, the ultimate force found from the FE model for different values of the contact gap are plotted in Figure B.5.

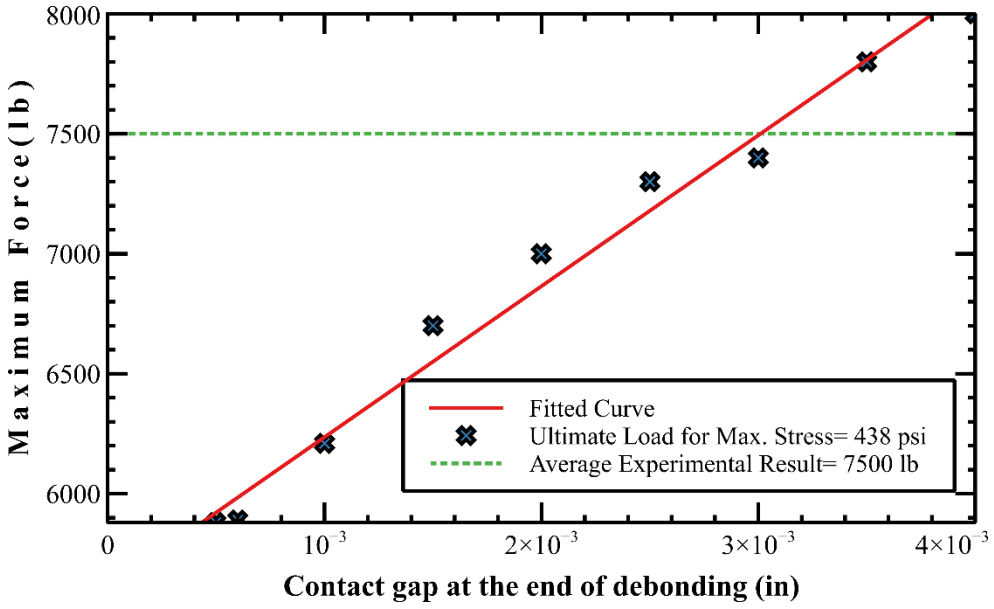

Figure B.5: Maximum load versus contact gap for interface model calibration.

From the experiments, the average ultimate force was found to be 7500 lb. In Figure B.5, the force 7500 lb corresponds to the contact gap of 0.003 inch. Therefore, this value was used for CZM materials in the FE models of the pullout test and the flexural beam test.

Appendix C: 3D Modeling of the Flexural Beam Test

C.1 Introduction

The finite element analysis should be simplified by using truss or beam elements, taking advantage of plane stress/ plane strain conditions, symmetry and axi-symmetry whenever possible. But sometimes, 3D models are absolutely required due to the nature of the projects. Most commercial FE programs come with their native CAD tools for modeling. For example, ANSYS has two CAD modelers- SpaceClaim and DesignModeler. Other than that, many exclusive CAD software are also available. However, generally dedicated CAD programs and FE programs treat the geometries in a slightly different fashion. That is why the best approach is to use the native CAD program included in the FEA distribution. But sometimes, these native CAD programs are not very suitable for large and complex models. In that scenario, using an external CAD software can make the workflow easier. A 3D model created in a dedicated CAD software must be simplified and optimized before using in an FEA program. The commercial CAD packages can be broadly divided into two types- direct, and parametric modelers. Between them, the parametric type is more suitable for FE analysis. Solidworks, Autodesk Inventor, Siemens NX, Creo, and CATIA are some of the most widely used parametric CAD programs used in the industry. In this chapter, 3D model of the flexural beam tests will be created using Onshape. Onshape is a powerful browser-based parametric CAD tool that has an interface similar to that of Solidworks.

C.2 Step-by-Step 3D Modeling

Step 1. Go to the Onshape website (http://cad.onshape.com), create an account, and sign in. In the dashboard, click on the blue “Create” button at the top left corner (under the Onshape logo) and select “Document”. In the dialogue box, type a convenient name for the model and then click OK.

Step 2. At this point, the workspace will open. Click on the button with three horizontal stripes at the top left corner, besides the Onshape logo, and click on “Workspace units”. Change the units to inches.

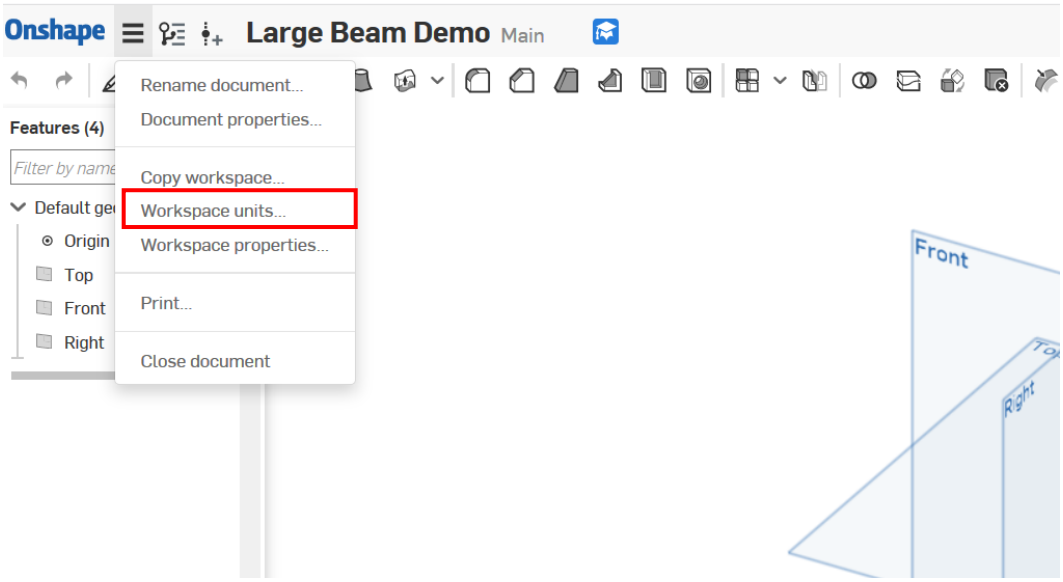

Figure C.1: Changing the units in Onshape.

Step 3. From the top toolbar, click on “Sketch”. A sketch dialogue box should appear beside the Feature Tree. In the dialogue box, while the “sketch plane” is selected (in blue), select a plane from the Feature Tree. Alternatively, a plane can also be selected by clicking that plane in the viewport. For this case, the “Right plane” (YZ plane) will be selected. The View Cube at the top right corner of the viewport can be used to adjust the view. Clicking on any face or corner of the View Cube will orient the view perpendicular to that plane or corner.

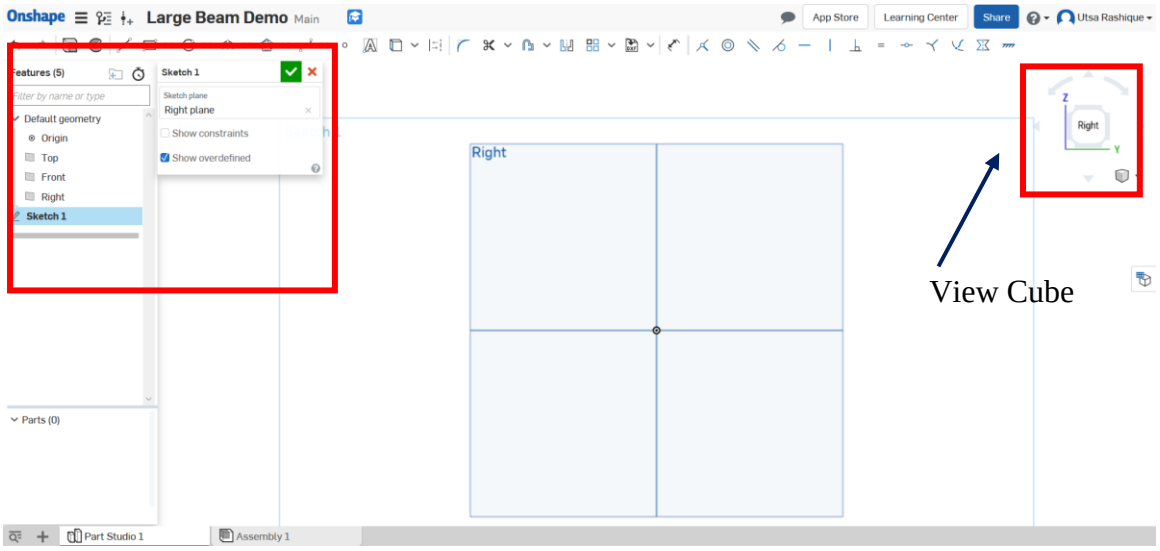

Figure C.2: Creating a new sketch and adjusting the view.

Step 4. Click on the "Corner rectangle" tool from the top toolbar and draw an arbitrary rectangle as shown in Figure C.3. The dimensions are not required to be accurate at this point.

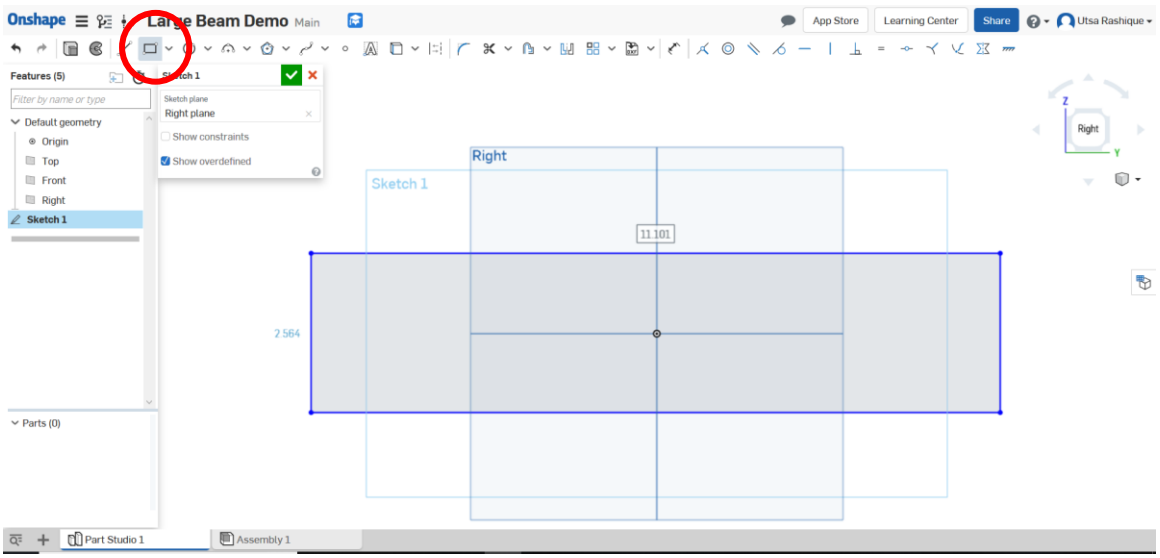

Figure C.3: Drawing a rectangle in sketch mode.

Step 5. Click the "Symmetric" button from the top toolbar. Then click the Y-axis in the viewport, and the two sides parallel to the Y axis subsequently. Do the same for the sides parallel to the Z axis. This will ensure that the dimensions of the rectangle will

always be symmetrical with respect to the two axes, and the parallel sides will be equidistant from the origin.

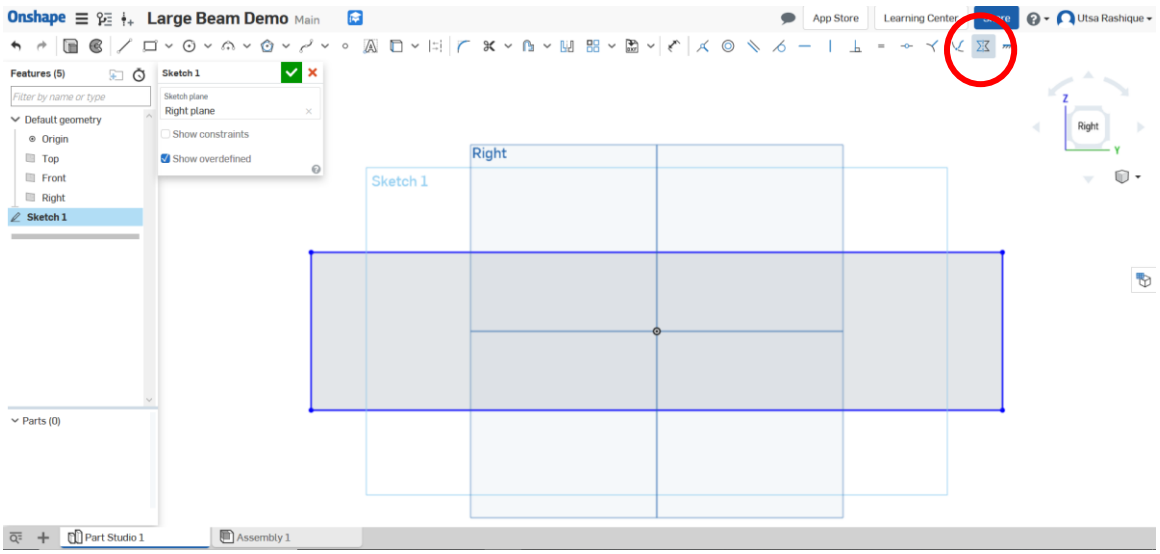

Figure C.4: Defining the symmetry constraint.

Step 6. From the top toolbar, select the "dimension" tool. Click on any of the sides of the rectangle and type the dimension for that side. Do the same for any of the two sides perpendicular to the previous side. In this case, we are using a length of 72 inches, and a height of 8 inches. Note that, "over constraining" the sketch will turn the color of the sketch to red, and further operations like rotation or extrude might not be possible on that sketch. Recurring dimensions can cause "over constrain". For example, by definition, defining the dimension of one side of a rectangle fixes the length of the opposite side. Adding another dimension to that opposite side will "over constrain" the sketch.

Step 7. After defining the dimension, click on the green tick mark in the Sketch 1 dialogue box. This will finalize the sketch and exit the sketch mode.

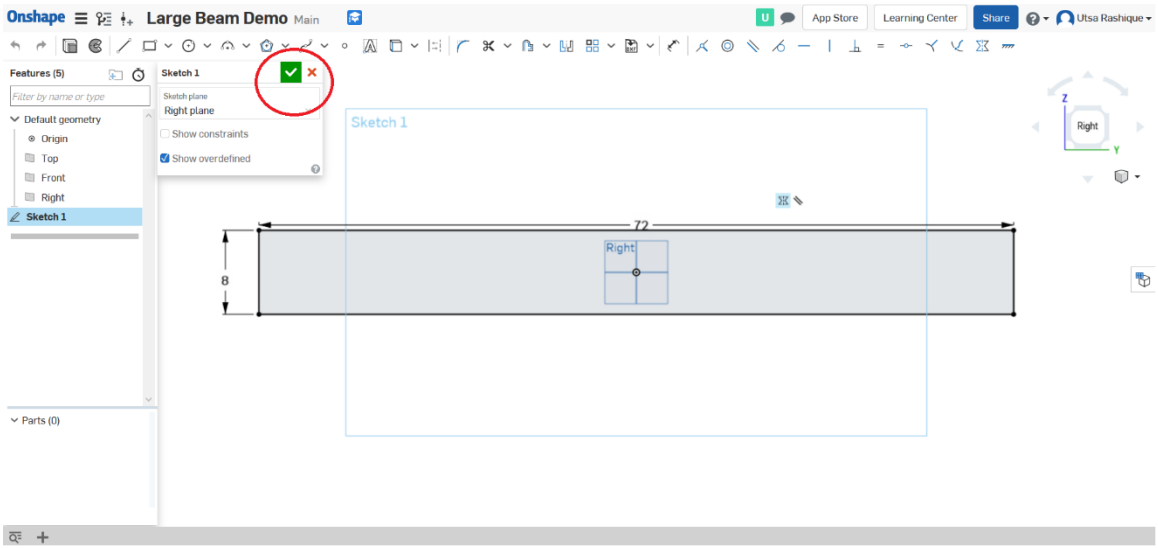

Figure C.5: Defining dimensions.

Step 8. From the top toolbar, click the "Extrude" option. In the appearing extrude dialogue box, click on "Faces or sketch region to extrude" and then click on the sketch created in the previous steps. Make sure that the "Solid" and the "New" tabs are selected. For "End Type", select "Symmetric" and set the "Depth" to 12 inches. Change the view to perspective using the view cube for better visualization. Click the green tick mark in the extrude dialogue box to complete the extrusion process.

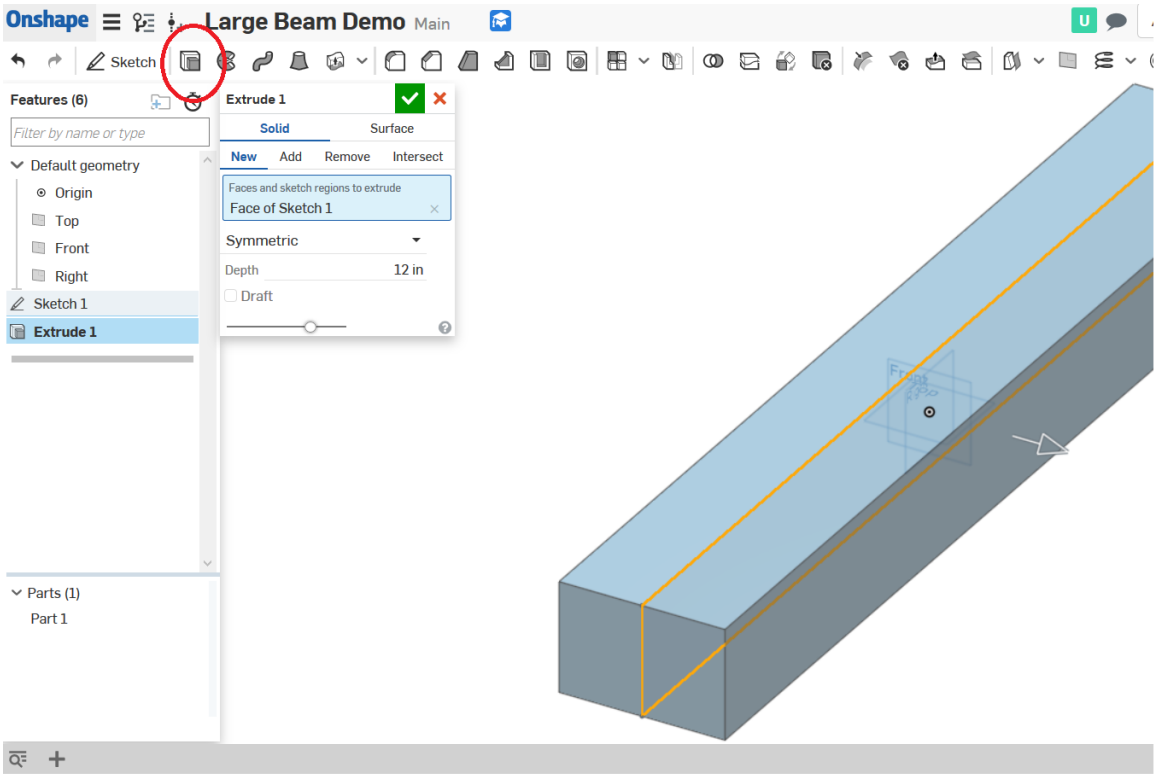

Figure C.6: Extruding a sketch.

Step 9. Note that, in the left-hand side, a new part "Part 1" has been added under the "Parts" tree. This is the solid element created in the previous step, which will be used to model the precast sections eventually. Right click on the name of the part and then rename it using the "Rename…" option. For convenience, here it will be named as "Precast". Now, right click on "Precast" again, and select "Hide…". The solid object will be hidden. This was done to clean up the workspace for drawing a new sketch for the closure pour section.

Step 10. Same as step 3, create another instance of a sketch in the right plane. Change the view necessarily from the view cube. Now, using the "Line" tool from the top toolbar, draw a shape similar to the one shown in Figure C.7 (the dimensions are not needed to be accurate at this point). Now, apply the necessary symmetry constraints and dimensions to the sketch as shown in Figure C.8. (Note: the angular dimension is

defined by selecting the dimension tool and then clicking the two lines forming the angle).

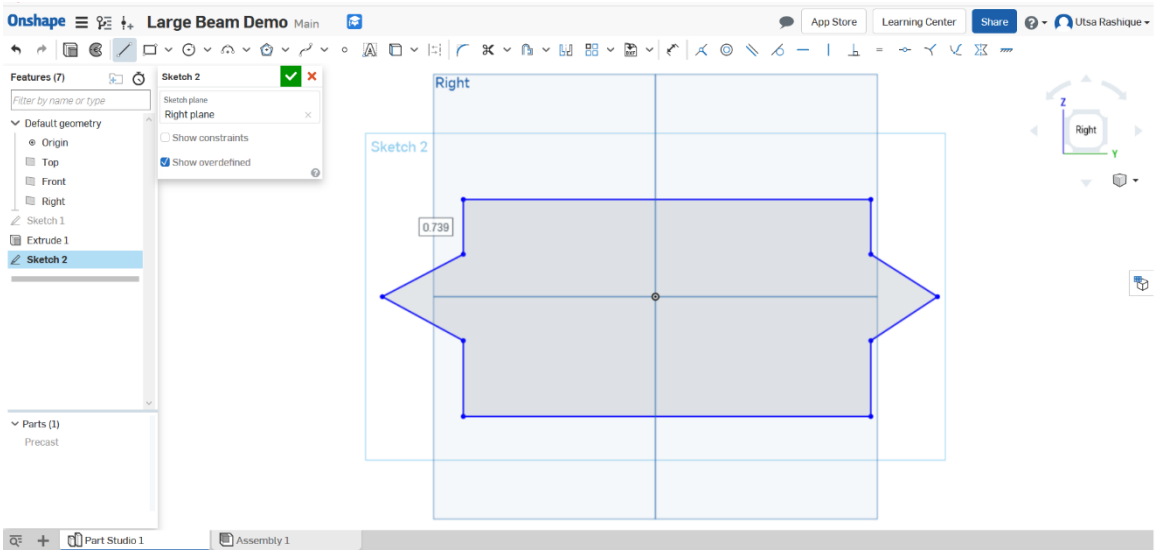

Figure C.7: Sketch for the closure pour section.

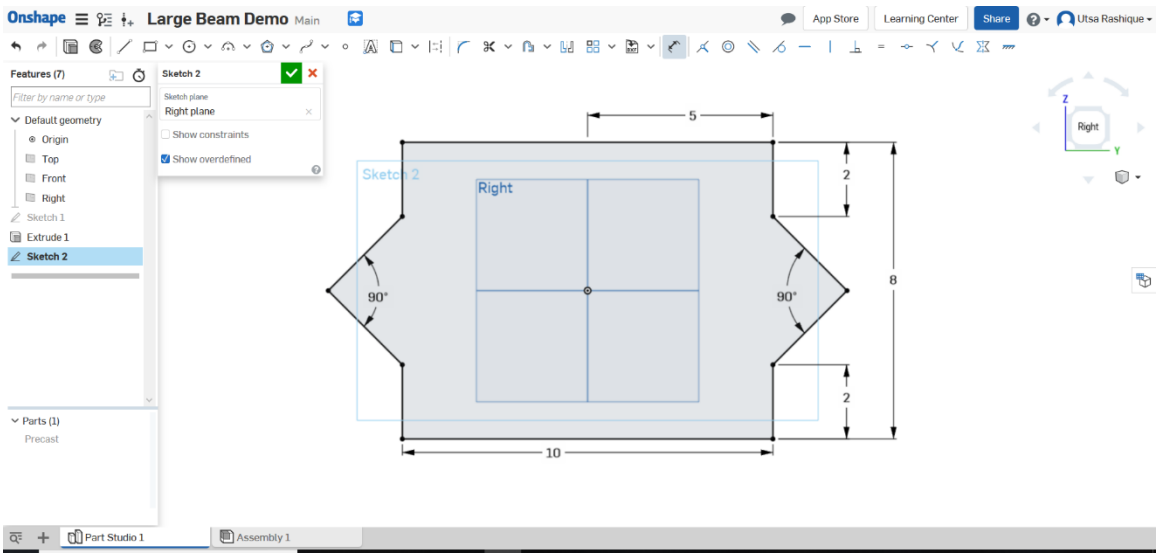

Figure C.8: Adding dimensions and constraints to the sketch.

Step 11. Following the procedure described in step 8, extrude this new sketch symmetrically with a depth of 12 inches. Rename the new part as “Closure”. Unhide the “Precast” part.

Step 12. Note that, the two parts are now overlapping. One way to solve this issue is to use the Boolean function. From the top toolbar, click the “Boolean” tool. In the Boolean dialogue box, select Subtract. Then click on “Tool” and then select “Closure” for the Parts list. Then click on “Target” and select “Precast”. The tool is the body that is subtracted from the target body. Make sure that, the checkbox beside “Keep tools” is selected. Then click the green tick mark. The Boolean operation should now be complete. Hide the “Closure” part to make sure that the operation was completed as intended. Note that, the “Precast” part is no more a continuous body, rather it has been turned into two discrete bodies. That is why two “Precast” parts under the Parts list appear. Rename the two parts to distinguish them. Here, they will be renamed as “Precast 1” and “Precast 2”.

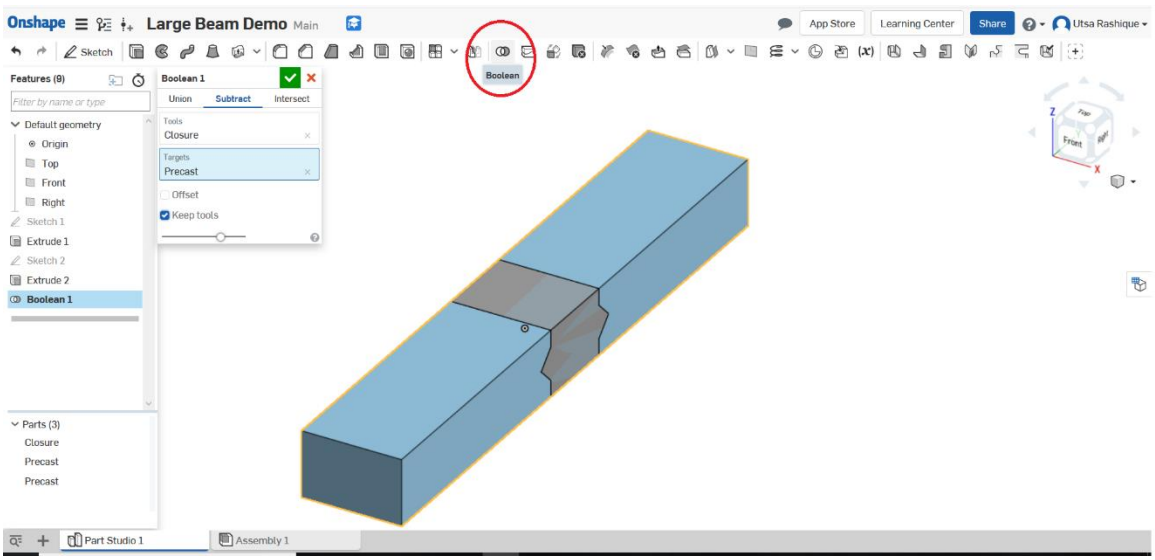

Figure C.9: Boolean subtraction operation on the precast body.

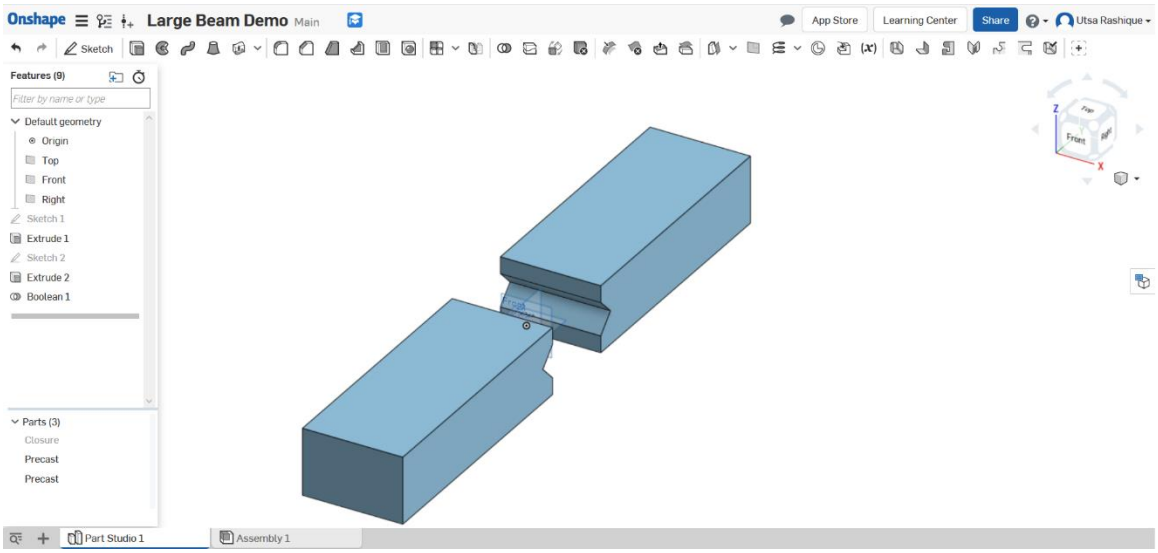

Figure C.10: Result of Boolean subtraction.

Step 13. Hide all the parts. Create a new sketch in "Top plane" For the headed rebar, draw a sketch similar to Figure C.11 and give the necessary dimensions as shown in the figure. Draw another sketch for the second headed rebar and give necessary dimensions as given in Figure C.12.

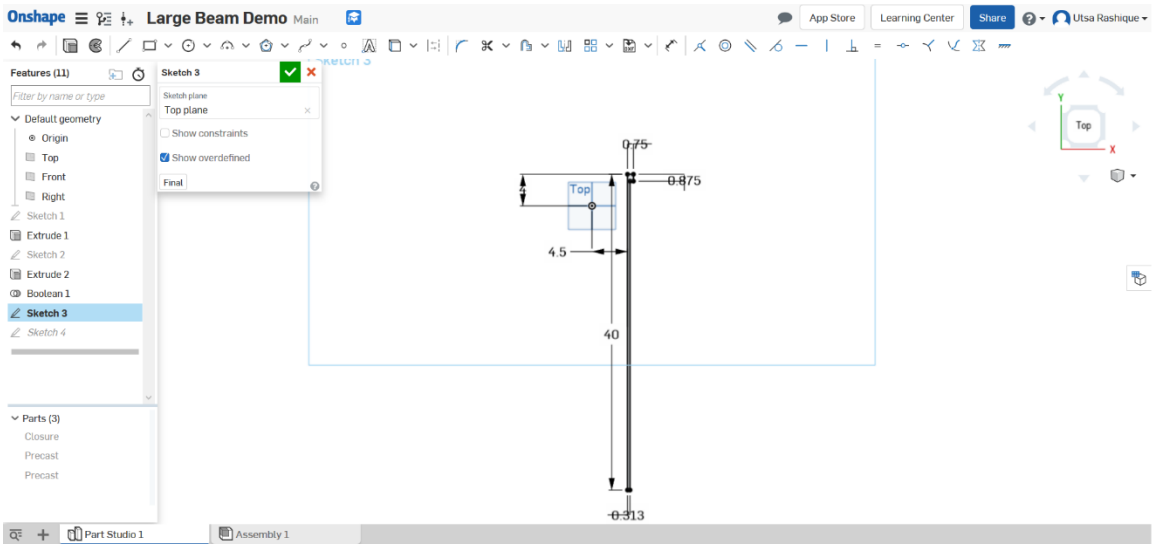

Figure C.11: Sketch for the first headed rebar.

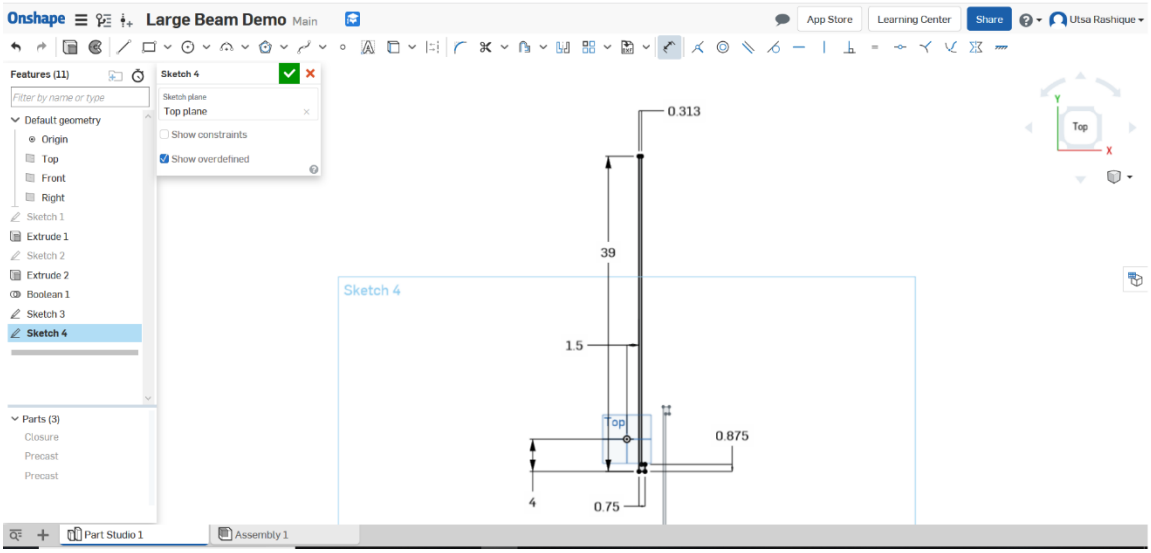

Figure C.12: Sketch for the second headed rebar.

Step 14. Exit from the sketch mode. From the top toolbar, select “Revolve”. In the dialogue box, make sure that “Solid” and “New” tabs are selected. Click on “Faces or sketch regions to revolve” and then select one of the sketches created for the bottom rebars. Then click on “Revolve axis” and select the longest axis line of that sketch (the line that has a dimension of 40 inches). Make sure that, the revolve type is “Full”. Confirm the action. A rebar part will be created. Rename it to “Bottom Bar 1”. Repeat the process for the other sketch and rename the new solid as “Bottom Bar 2”.

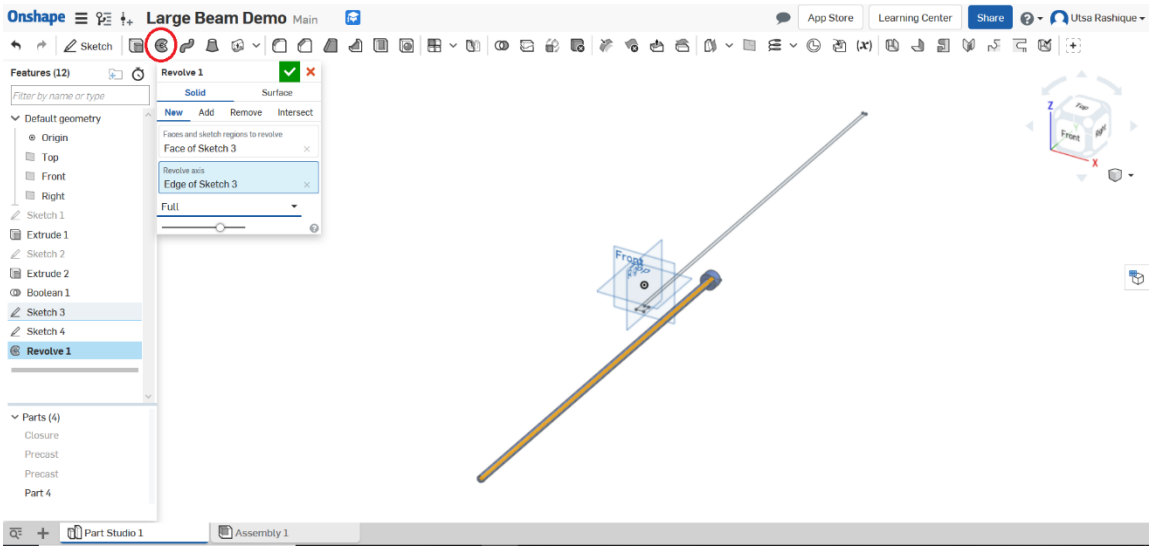

Figure C.13: Revolving the sketch to create rebars.

Step 15. Now, select the "Transform" tool from the top toolbox. For "Entities to transform or copy", select the two headed rebar bodies. For transform type, select "Translate by XYZ". Here, we need to create one more copy for each of the headed bars, and the copies should be on the left side of the existing ones, i.e., along the negative X direction. So, check the box beside "Copy parts" and put a value of -6 for X-axis. Then confirm the operation. Rename the two new parts.

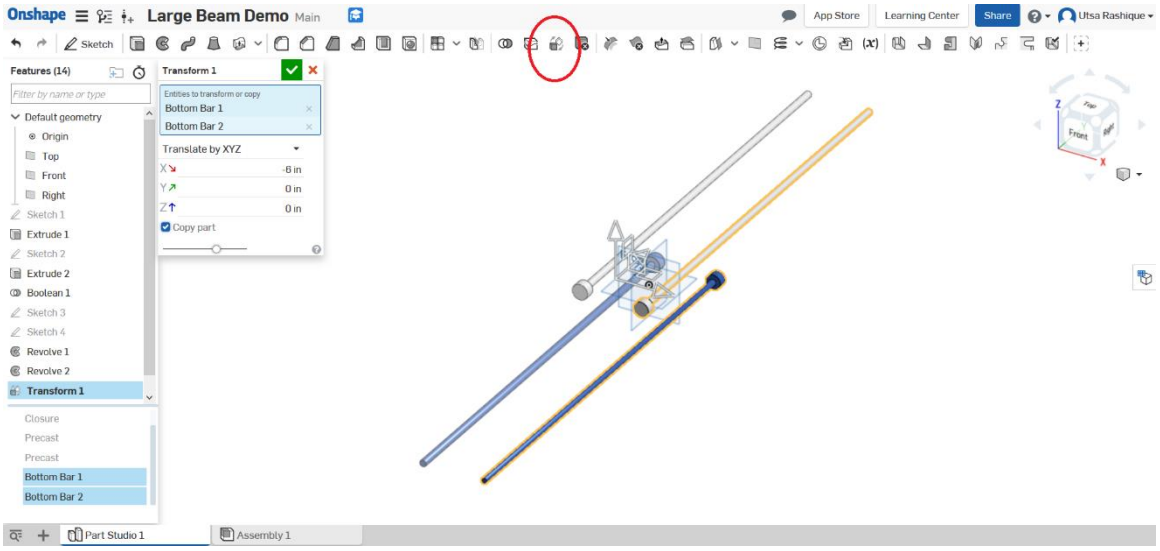

Figure C.14: Using the "transform" tool to create copies.

Step 16. Now, repeat the “Transform” operation once more. This time, select all 4 rebars, do not check the “Copy parts” box, and put a value of -2 for Z-axis while X and Y values remain 0. This operation will bring all four bottom rebars down by 2 inches.

Step 17. Repeat steps 13 to 16 again for the top bars. Note that, the top bars are not headed bars. So for the sketch of a top bar, a simple rectangle will suffice. And finally, after creating all four top bar models, translate them by 2 inches in the positive Z direction. Make all eight bars visible. They should look like Figure C.15.

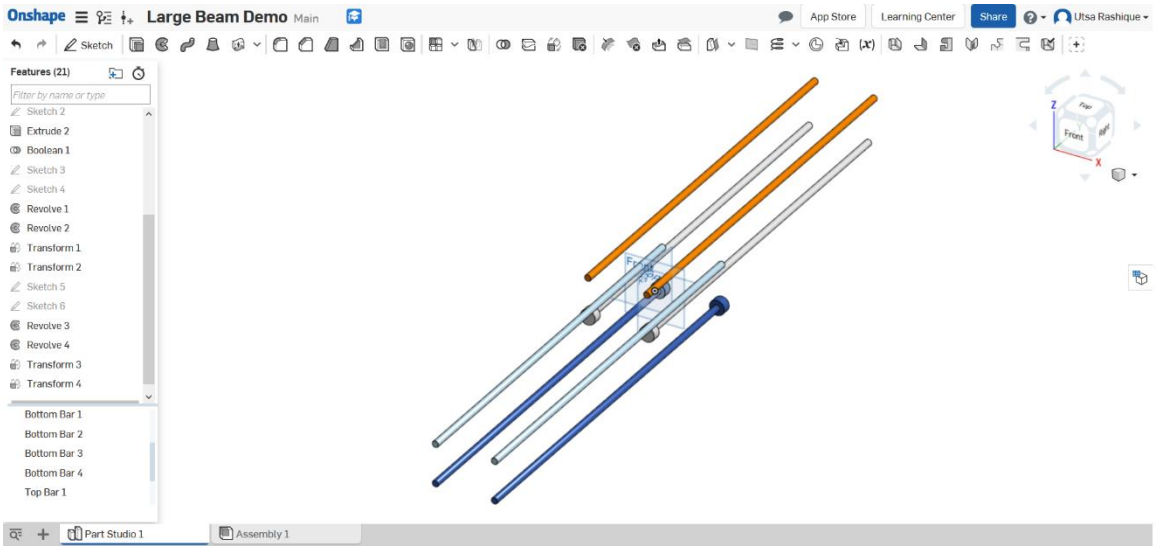

Figure C.15: All eight rebars after "revolve" and "transform" operations.

Step 18. Finally, as the concrete and the rebar models are now overlapping, a final Boolean operation is required. This time, use the eight rebar parts as tools, and the three concrete parts as the targets. Make sure to check the “Keep tools” option. Hide the bars to make sure the shafts have been created from the Boolean subtraction operation. At this point, the model is complete and should look like the one shown in Figure C.16.

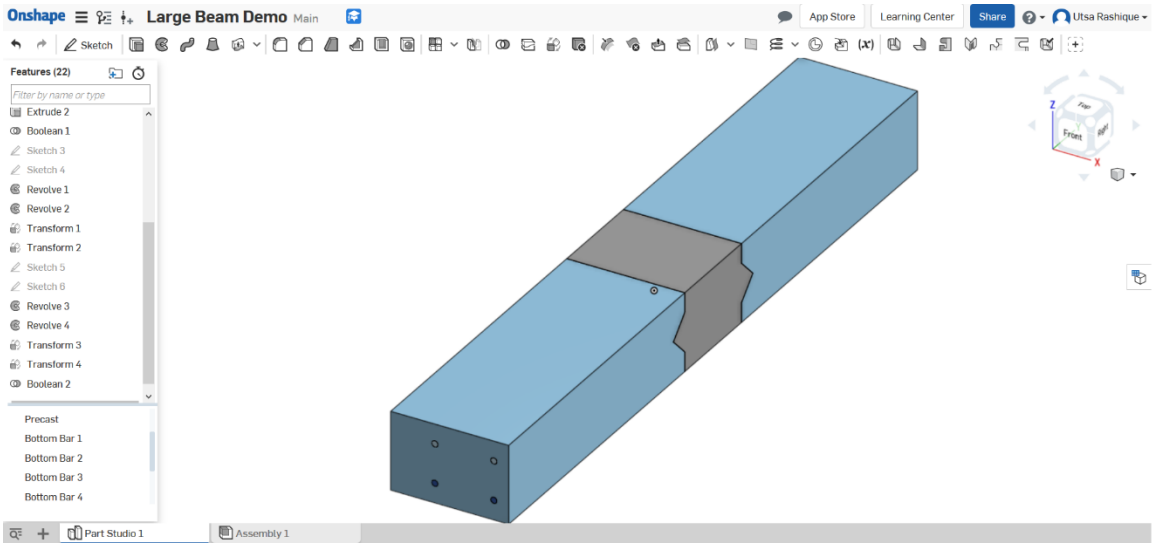

Figure C.16: Subtracting the rebars from the concrete bodies.

Step 19. Now, the 3D model has to be downloaded. Note that, there are two tabs at the bottom of the workspace, namely “Part Studio 1” and “Assembly 1”. Right-click on “Part Studio1”, then click “Export…”. In the dialogue box, give the 3D model file a suitable name. For the “Format”, select a format that is also supported in ANSYS. Onshape allows exporting the 3D model in many formats. Among them, PARASOLID, ACIS, STEP, and IGES formats are also supported by ANSYS. In this study, it was found that the ACIS format provided the most seamless and reliable interchange of 3D models between Onshape and ANSYS. Finally, select OK. The 3D model file will begin downloading within a few seconds. The downloaded file will have the *.sat extension.

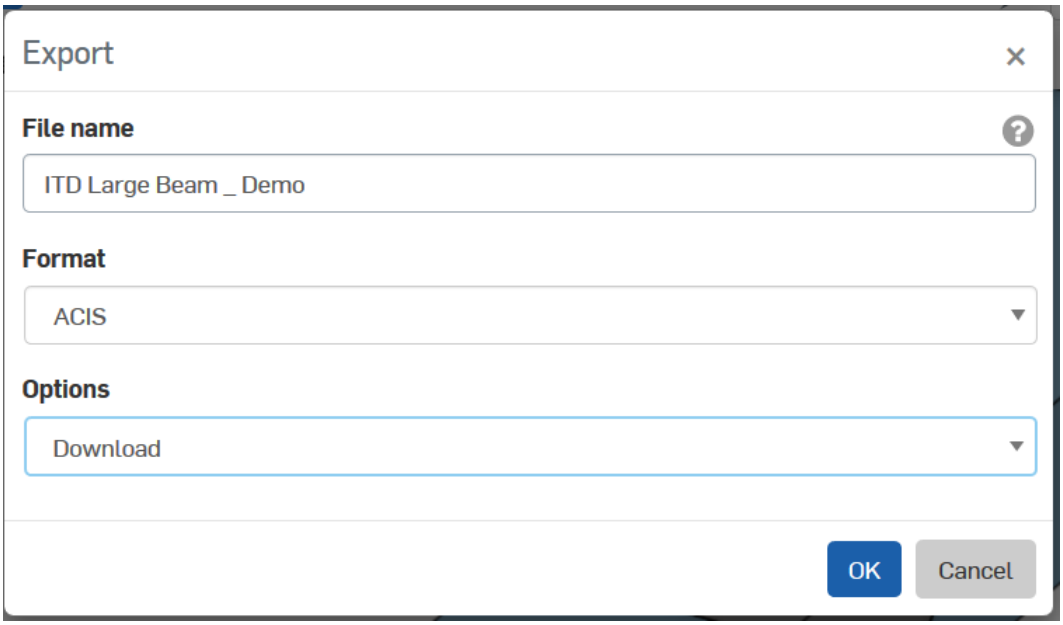

Figure C.17: Exporting and downloading the 3D model.

Appendix D: Step-by-Step FE Modeling of the Flexural Beam Tests

D.1 Introduction

ANSYS APDL is the legacy module of the software that houses all the codes for the preprocessing, solution, and post-processing units of the program. ANSYS Workbench is a relatively modern interface, which is built on top of the traditional APDL. With a nice Graphical User Interface (GUI), the Workbench is generally more intuitive and easier to work with. It also allows the user to combine and connect multiple modules like static and dynamic structural analysis, modal analysis, electromagnetic analysis, and fluid mechanics. The Workbench uses the APDL solver module to analyze the FE model. On the other hand, ANSYS APDL is mostly command based, with some basic GUI features available. Being command based, although it required more advanced skills on the user's part, it is more customizable and powerful when some advanced and complex FE techniques are involved. In the FE modeling of the large beams, both Workbench and APDL will be used to utilize the advantages of both the interfaces.

D.2 FE Modeling of the Three-Point Test

Step 1. Open ANSYS Workbench. From the toolbox panel on the left, drag one "static structural" module to the blank white space in "project schematics".

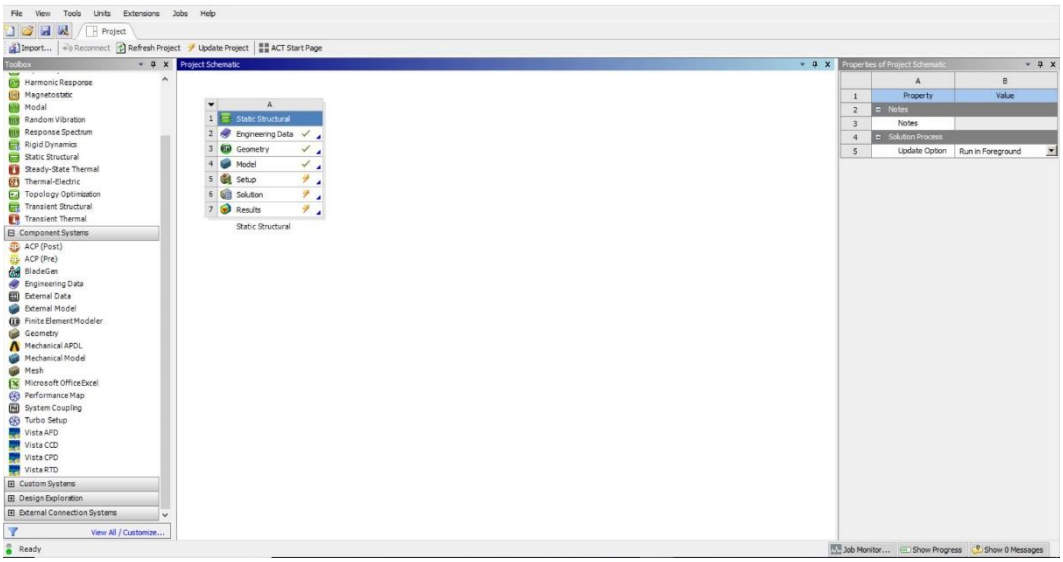

Figure D.1: Creating a new module in ANSYS Workbench.

Step 2. Double-click on “Engineering Data”. Click on “click here to add new material” to type the names of materials to be defined.

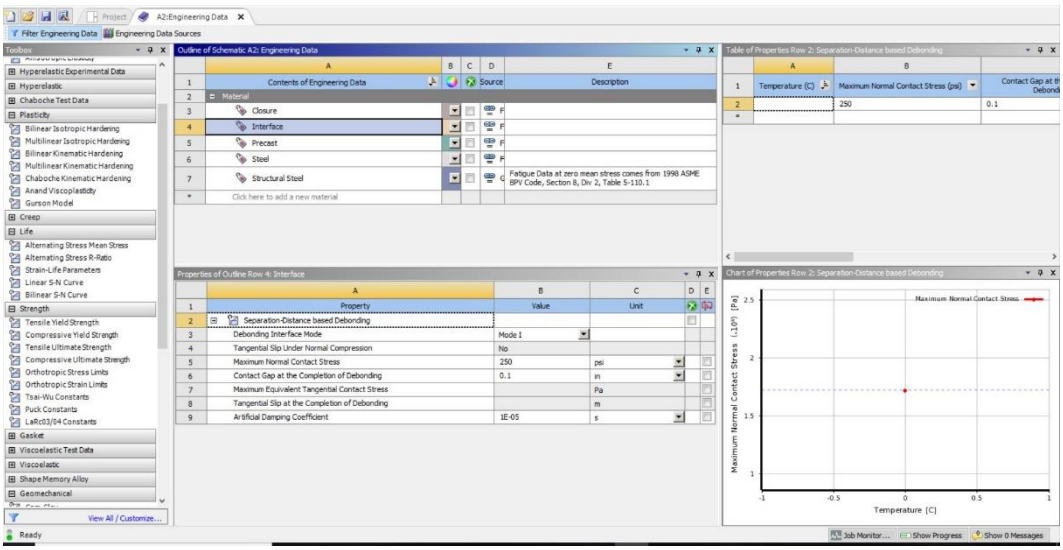

Figure D.2: Defining material properties in "Engineering data".

Step 3. For concrete material, double click on “Linear Elastic> Isotropic Elasticity” from the toolbox panel on the left. Define the elastic modulus and Poisson’s ratio. The units can be changed from the drop-down boxes on the right.

Step 4. For steel material, define isotropic elastic properties. Then double click on “Plasticity> Bilinear Isotropic Hardening”. Define the yield strength and tangent modulus.

Step 5. For the interface model, go to “Cohesive Zone> Separation-Distance Based Debonding”. For the “Debonding Interface Property”, select Mode I. Then define maximum contact stress, contact gap at debonding and artificial damping coefficient.

Step 6. Close engineering data. Right click on “Geometry” in the static structural module. From the context menu, go to “Import geometry> Browse”. Browse to the location of the required geometry file, select it and click OK.

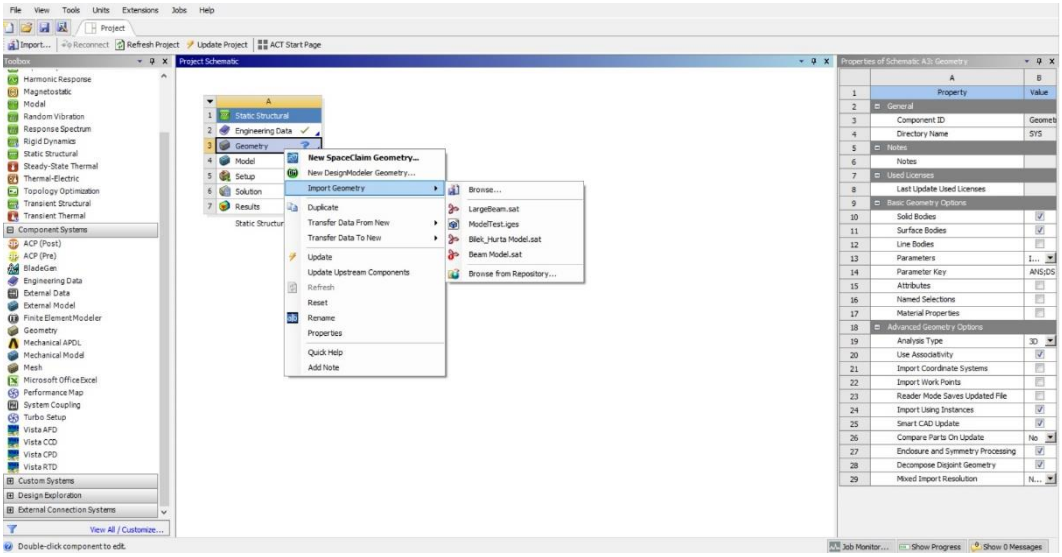

Figure D.3: Importing a geometry into ANSYS.

Step 7. Right click on Geometry again, then click on “Edit in DesignModeler”. When Design Modeler opens, click on “Generate”. The 3D model should be visible.

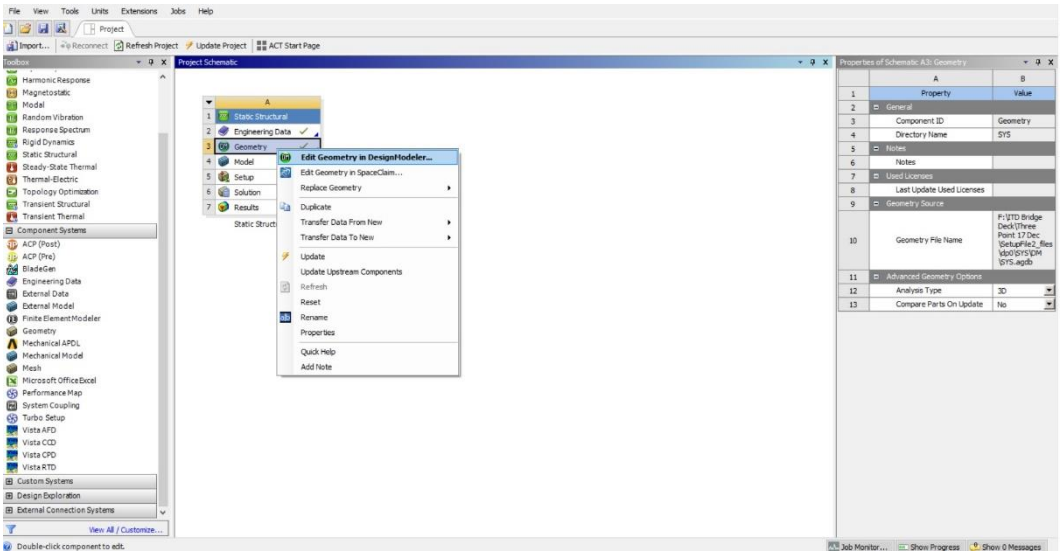

Figure D.4: Opening geometry using DesignModeler.

Step 8. Make sure that the units are in inches. From the top menu, select "Unit>Inch". In the "Tree Outline", click the "+" sign beside "X parts, X bodies" (X representing the number of parts and bodies in the 3D model). The list of parts and bodies will expand. Right clicking on the name of any part or body will open a context menu. From the "rename" option, rename the bodies for convenience.

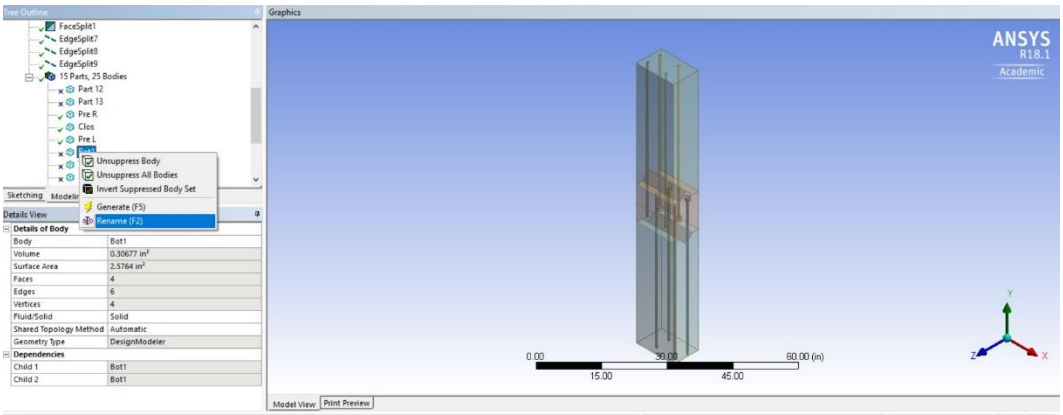

Figure D.5: Renaming the parts in a geometry file.

Step 9. With body selection filter selected, click on the two precast concrete bodies while holding the control button of the keyboard. Both will be selected and appear green. Right-click and select “hide bodies”. Now, only the closure and the rebars should be visible.

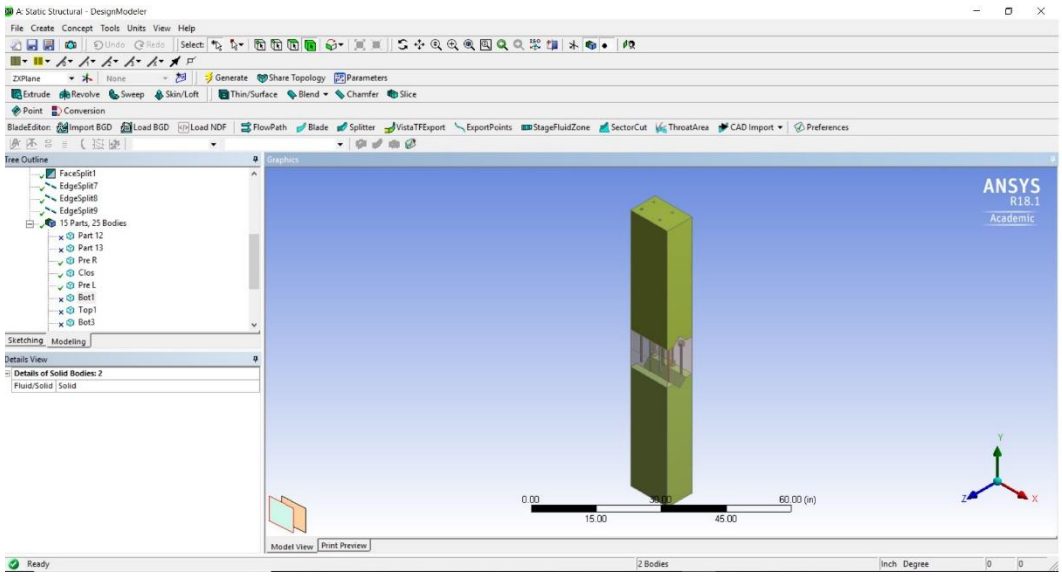

Figure D.6: Hiding bodies in DesignModeler.

Step 10. Go to “Create> Slice”. In the “details view” on the bottom left, select “slice by surface” for Slice Type. Then click on “Target Face”. Activate face selection filter. Click the two vertical faces at the bottom of the closure where the bottom rebars are protruding out from. For “Slice Target”, select “Selected Bodies”. Click on “Bodies”, and select the four bottom rebars, click “Apply”. Click “Generate”. Now, each bottom rebar will be sliced into two divisions.

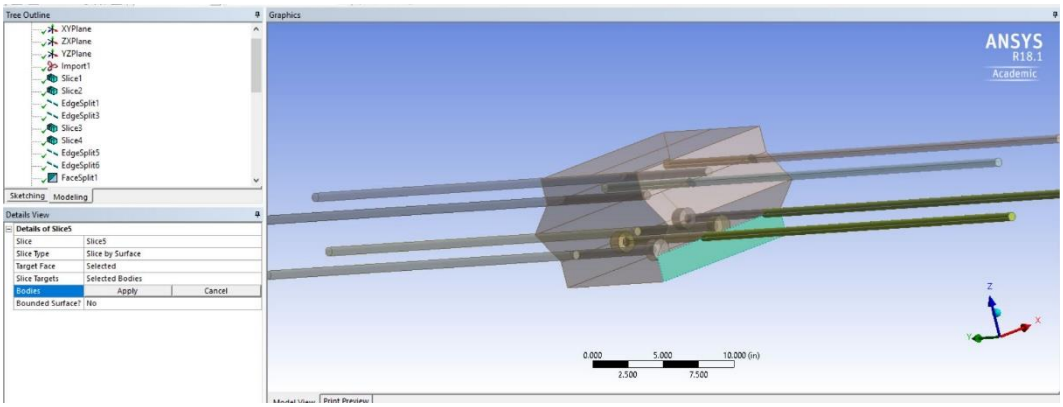

Figure D.7: Slicing the bottom rebars.

Step 11. Now hide everything except the bottom rebars. Zoom in on them. Notice that, there are two lines running along the entire length of one rebar (including the head). The lines are either on the top and bottom of the bar or on the sides. Go to "Concept> Split Edges". In the details view, for split type, select "Split by N". Click on "Edges". Now select the edges along the front parts of the bottom rebars (the parts inside the closure, excluding the heads). Click apply. 8 edges should be selected. Enter 8 for the value of FD4, N. Keep the values of FD2 and FD3 at 0. Then click "Generate". The edges should be divided into 8 parts each.

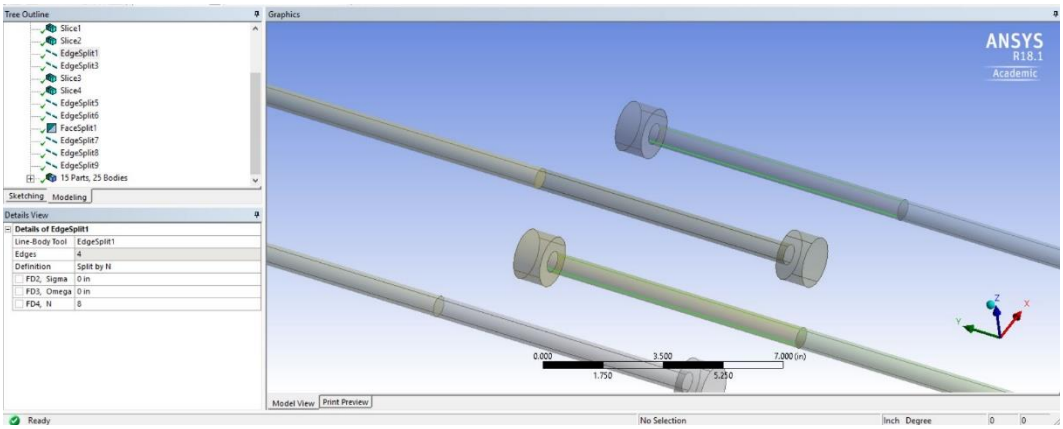

Figure D.8: Splitting the edges by number of divisions.

Step 12. Do the same as the previous step for the edges on the parts of bottom bars that are inside the precast sections. Except for this time, put 31 for FD4.

Step 13. Right-click anywhere on the graphics window and select “Show all bodies”. Now, select the closure portion, right click and select “Hide all other bodies”. Everything except the selected body will be invisible. Now rotate, pan and zoom to inspect the four shafts in the closure that the bottom rebars run through. There are two similar lines for each shaft. Split all eight of them using the method described in steps 10 and 11. Do the same for the shafts in the precast sections, but with FD4= 31.

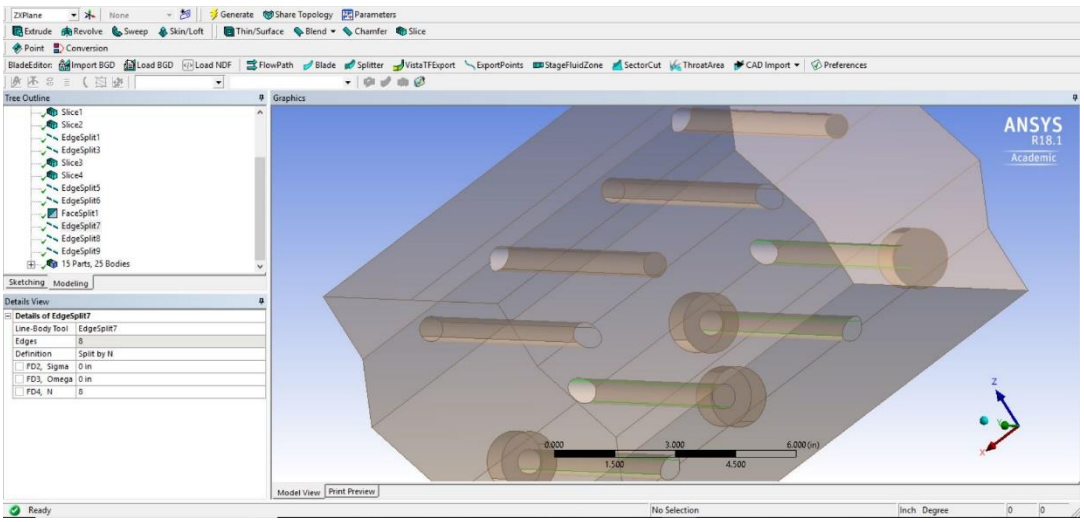

Figure D.9: Only the closure pour body and the shafts for the rebars in it are shown.

Step 14. Click on “Tools> Face Split”. In the details view, make sure that the split type is “by plane”. Click on “Target Face”. Select the face at the top of the closure pour. Click “Apply”. Click on “Tool geometry”. Now go to the Tree Outline and select the plane that runs perpendicular to the selected face along its width (in this case, the ZX plane). Then click “Apply”. The edge that is now splitting the face, will be used later to apply the load in three-point bending.

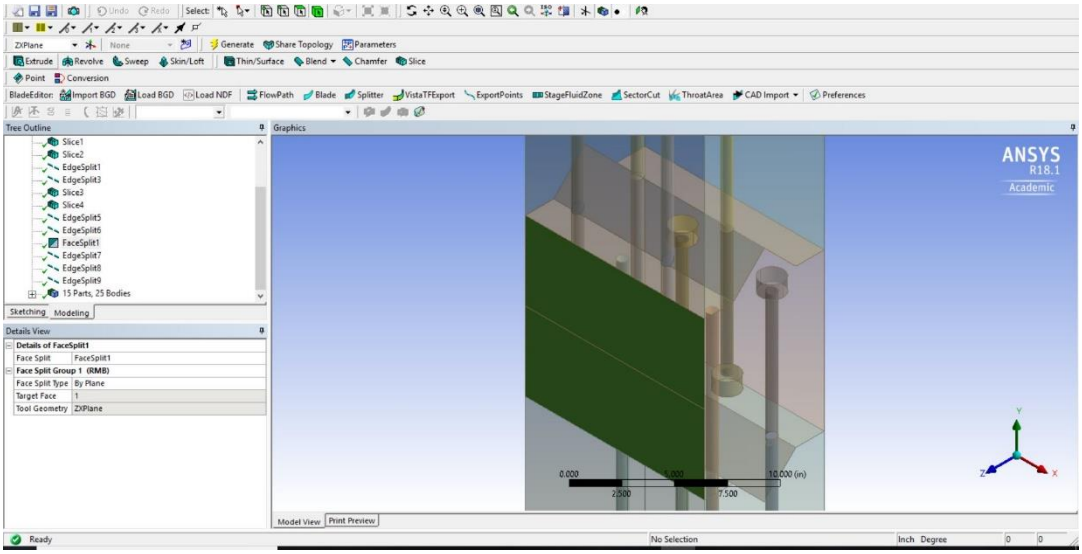

Figure D.10: Splitting a face by a plane.

Step 15. Click the "+" besides "X parts, Y bodies" again. Select the 8 bodies for the bottom rebars, while holding down the control key. Right-click and select "Form new part". Rename the part to convenience. This will treat all the parts of the bottom rebars as a monolith and during meshing, ANSYS will treat all of them as one object. Thus, the meshes will have merged nodes between the two parts of each bar, eliminating the need for defining contact elements between them.

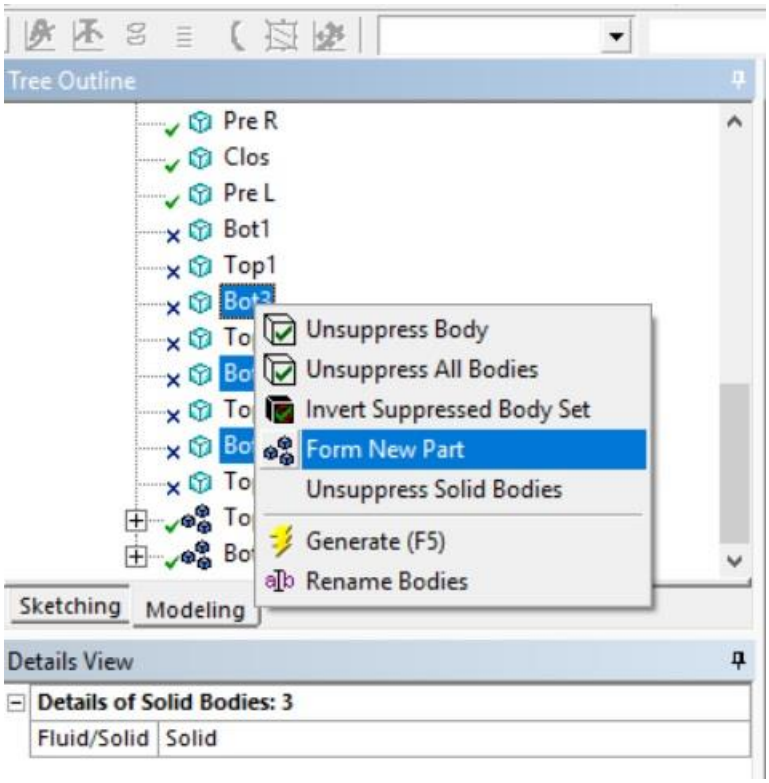

Figure D.11: Combining multiple parts into one part.

Step 16. Close Design Modeler. Double-click on "Model" to open ANSYS Mechanical. After Mechanical attaches the geometry, go to "Units" and select "U.S. Customary (in, lbm, lbf….)".

Step 17. In the outline window on the left, expand the "Geometry" section. Click on each of the part names. In the details window at the bottom left, click on "Assignment" under "Material" section, click on the arrow next to it, and select the corresponding material defined in steps 3, 4 and 5.

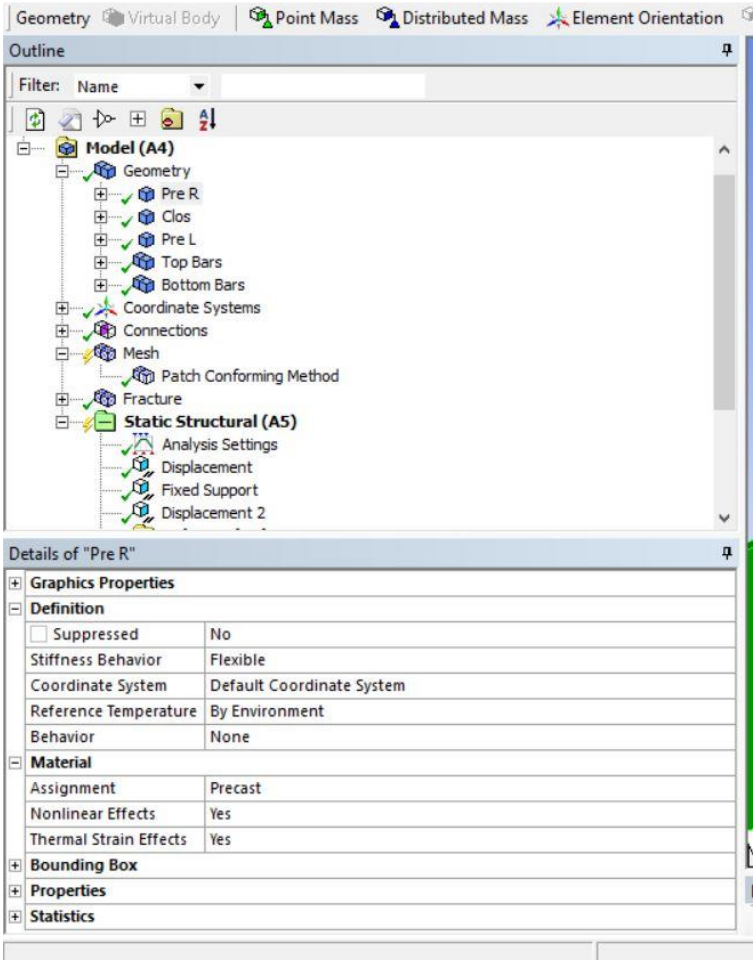

Figure D.12: Assigning materials to bodies.

Step 18. Right click on the name of the closure pour body. Then go to "Insert> Commands". In the command window, write the code for closure pour concrete material given at the end of this appendix. Do the same for the precast bodies.

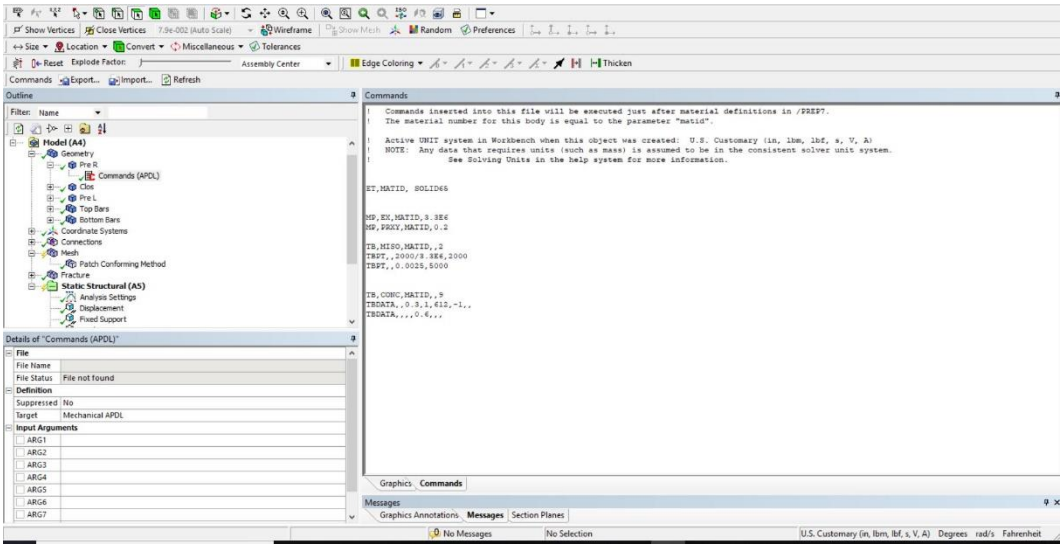

Figure D.13: Defining material properties using the APDL command module.

Step 19. Expand the "Connections> Contacts" tree. ANSYS will detect all the contact surfaces automatically and assign a bonded connection type by default. In the details window, change the contact details according to the following table:

Table D.1: Contact types and formulations.

Contact Between	Type	Formulation
Closure pour and precast	Bonded	Augmented-Lagrange
Top rebar and concrete	Bonded	MPC
Bottom rebar and concrete	No separation	MPC

The Cohesive Zone Model (CZM) only works with bonded contacts with Augmented-Lagrange or Pure Penalty formulation. Other than that, the use of MPC formulation is helpful to reduce the nonlinearity in the model. MPC stands for multi-point constraint and it employs constraint equations to define the relationships between contact and target elements.

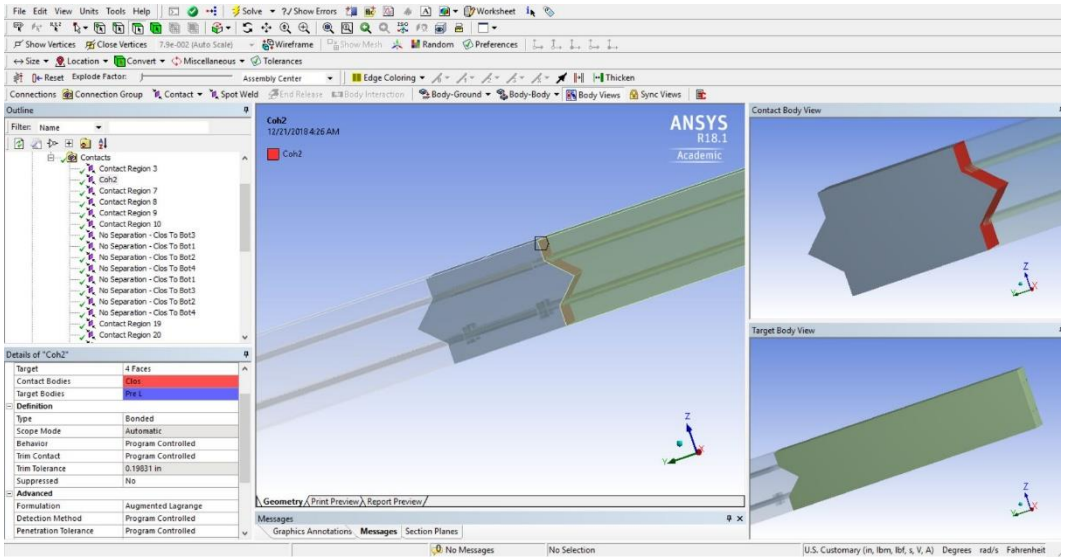

Figure D.14: Defining the contact types and formulations.

Step 20. In the outline tree, right click on “mesh” then go to “Insert> Method”. In the details of the method, make sure that the Scoping Method is “Geometry Selection”. Then click on “Geometry” in the details window and with body selection filter activated, select the three concrete bodies and then click “Apply” in the details window. For “Method”, select “Tetrahedron” and for “Element order”, select “Linear”. This step is necessary because SOLID65 is a linear element with brick or tetrahedral shape. As the bodies are not “sweepable”, the only option is to use tetrahedrons. If the elements are not linear or tetrahedral, ANSYS will not use SOLID65 elements ignoring the commands entered earlier. Right clicking on “Mesh” and then going to “Show> Sweepable bodies” will show the bodies that can be swept to create brick elements.

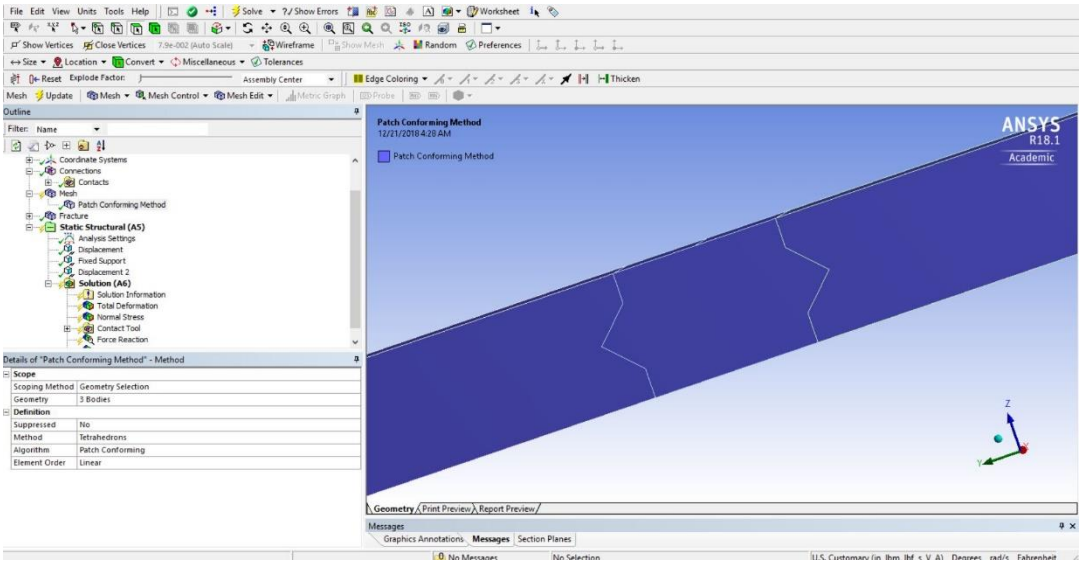

Figure D.15: Assigning mesh sizes and types to bodies.

Step 21. Right click on “Mesh” and click “Generate Mesh”. ANSYS will create mesh automatically. If the meshes seem too coarse, go to the details window, under “Defaults”, set the value of relevance to 10. Then under “sizing”, set the values of “relevance center” and “span angle center” to medium or fine until desired mesh size is achieved. A custom element size can also be defined from “Element Size” option under “Sizing”. But if the defined size is not conforming with the geometry or the changes to the geometry (face or edge split), the meshing could fail.

Step 22. Go to the top of the outline tree and right-click on “Model (A4)”. Go to “Insert> Fracture”. A new item called “Fracture” will be added in the tree under “Mesh”.

Step 23. Right click on “Fracture” and go to “Insert> Contact debonding”. A contact debonding sub-item will appear under the “Fracture” tree item. Select it and make sure that, in the details window, the method is CZM. For “Material”, select the CZM material defined earlier. The drop-down menu beside “Contact region” will show the list of all defined contacts. Select one of the two contacts between the precast and closure sections. Repeat this step for the second contact region.

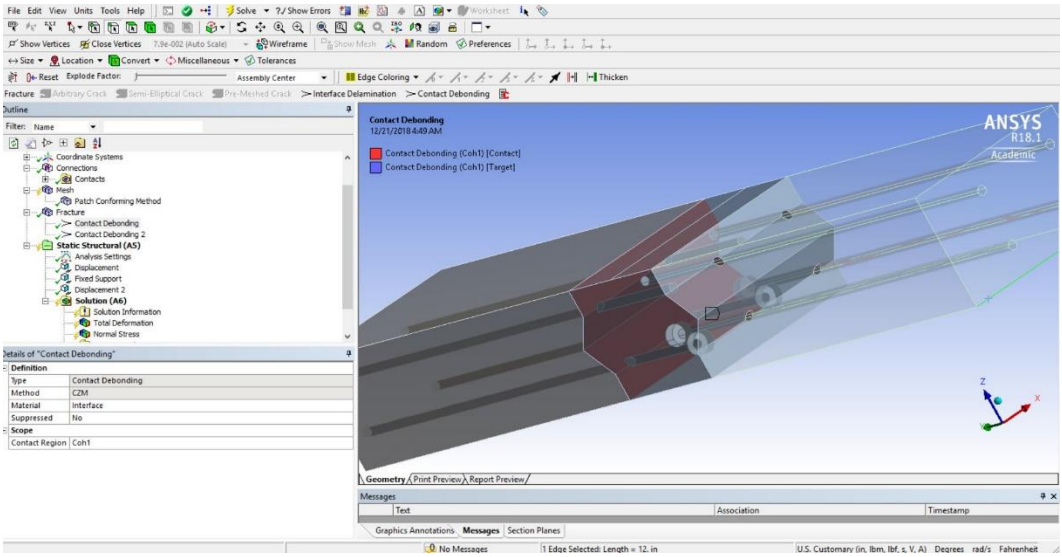

Figure D.16: Defining contact regions using CZM.

Step 24. In the outline tree, click on "Static Structural (A5)" and then activate the edge selection filter. The bottom edges of the right and left faces of the model will be used to define supports. Select the edge on the left, right click on "Static Structural" and then click "Insert> Fixed support". Select the right edge, right click on "Static Structural", go to "Insert> Displacement". In the details window of the Displacement support, enter 0 for the value of "Z Component".

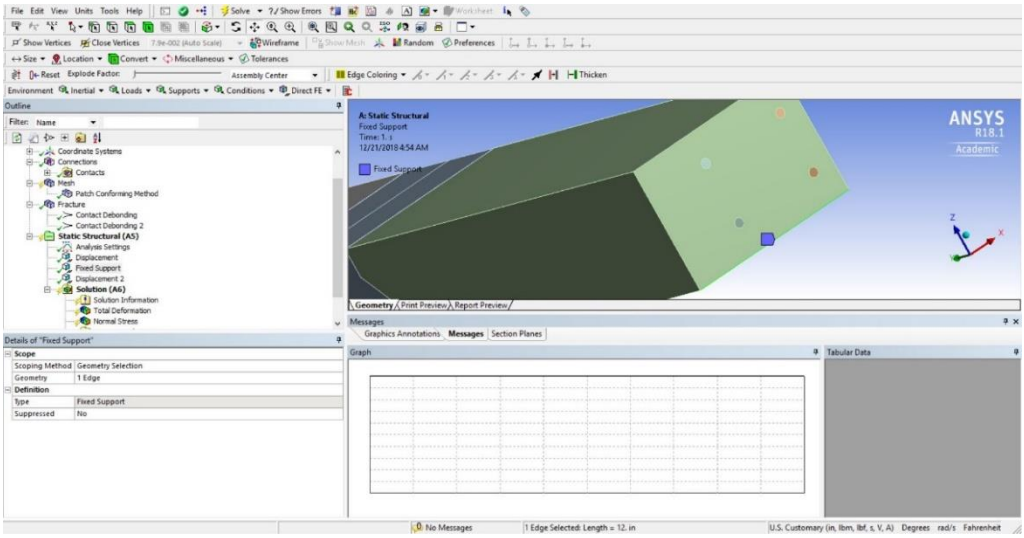

Figure D.17: Adding supports to the model.

Step 25. Select the edge in the middle of the top face of the closure, right click on "Static Structural", select "Insert> Displacement" and in the details window, enter "-0.25" for the value of "Z Component".

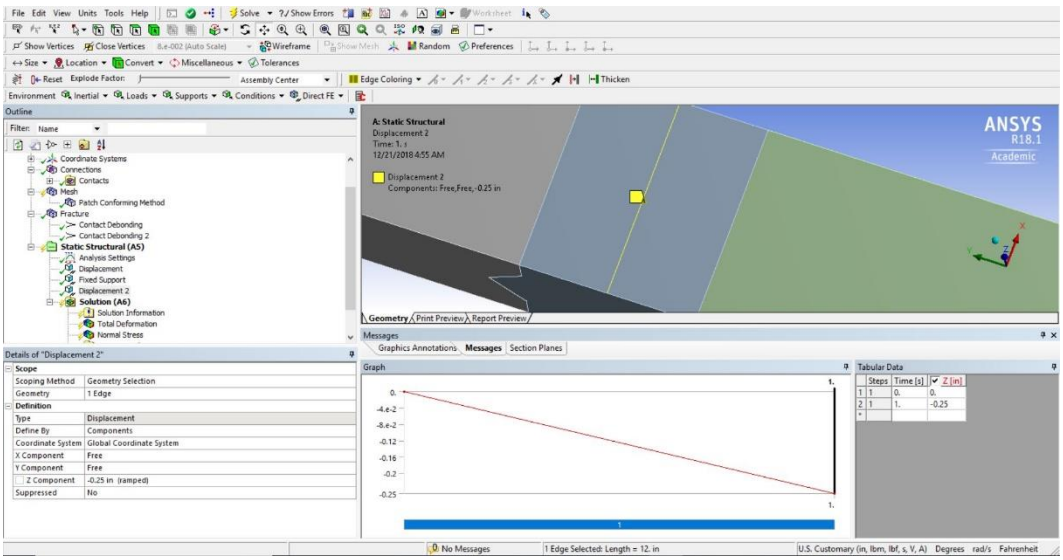

Figure D.18: Assigning displacement-based loading to the model.

Step 26. Now, with the "Static Structural" tree item selected, go to the top menu bar and select "Tools> Write Input File". In the save window, select the desired location for the input file to be saved and give it a suitable name.

Step 27. Close ANSYS Workbench. Make sure the Workbench project is saved. This project will be used later to retrieve the results. Open ANSYS Mechanical APDL. Define a location and a jobname for the APDL project. Click "File> Read input from…" and select the input file created in the previous step. Click OK. Then go to "Plot> Elements". The meshed model will appear.

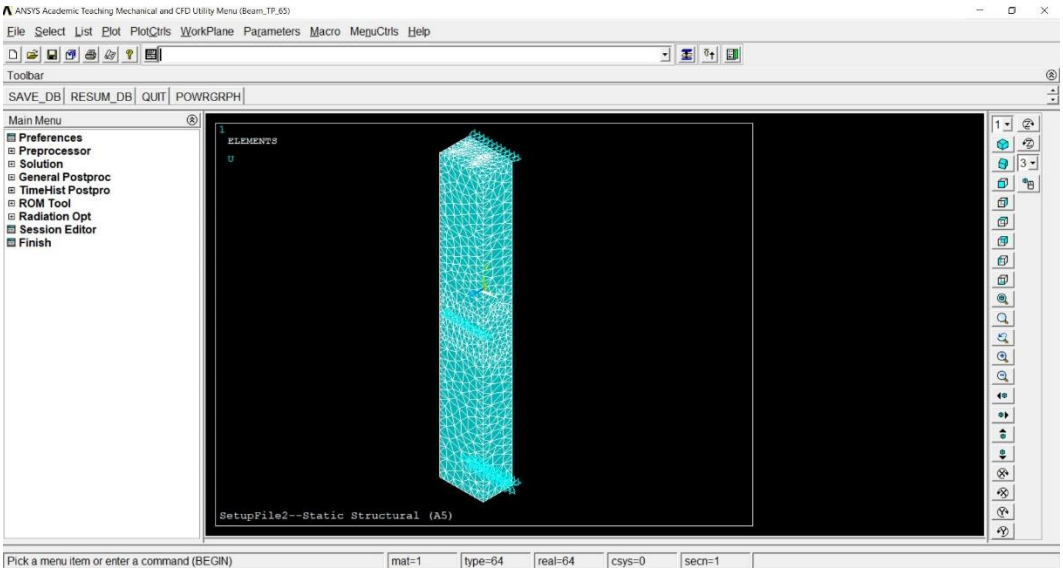

Figure D.19: Importing the input file into APDL.

Step 28. Go to "Preprocessor> Element Type> Add/Edit/Delete". In the Element Type window, click Add. Now, select the COMBIN39 element and click OK. In the Element Type window, select the COMBIN39 element just added and click "Options…". In the options window, select UY for the value of K3. This makes sure that the springs have 1 degree of freedom along the Y-axis. Also, take note of the element type number for the COMBIN39 element. Close the element type window.

Step 29. Go to "Preprocessor> Real Constants>Add/Edit/Delete". In the appearing window, click on Add. In the element type selection window, select the COMBIN39 element and click OK. A real constant definition window will appear. For convenience, make sure that the real constant set number is the same as the element type number for COMBIN39. No need to define the real constants right now. Click OK and close the Real Constants window.

Step 30. Go to "Modeling> Create> Elements> Elem Attributes". In the attribute window, select the element type number and the real constant set number for

COMBIN39 for the values of “[TYPE]” and “[REAL]”. Click OK and close the window.

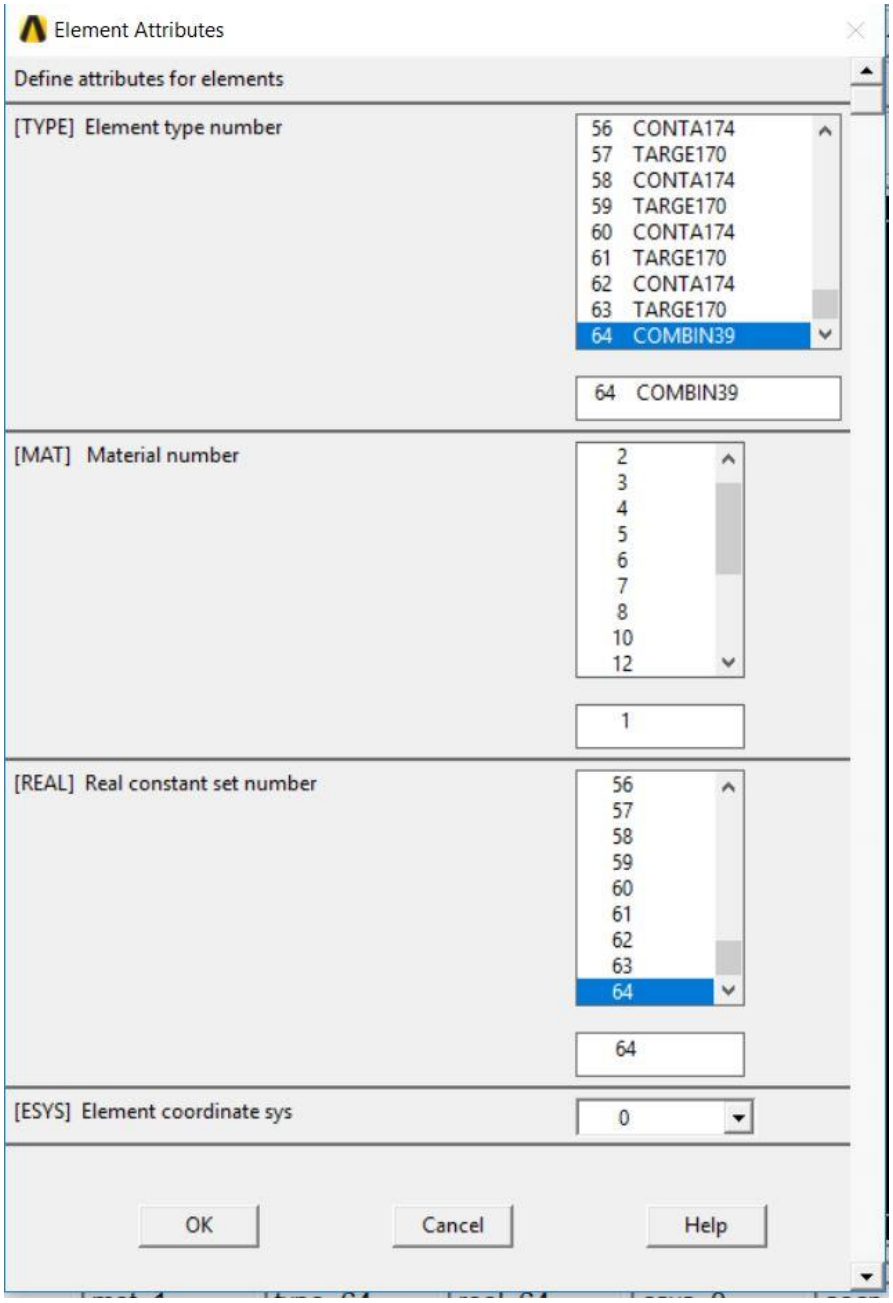

Figure D.20: Defining the attributes for the new elements to be created.

Step 31. Go to “Modeling> Create> Elements> Auto Numbered> At Coincid Nd”. Keep the tolerance value at default and click OK. In the node selection dialogue box, click “Pick All”.

Step 32. Click “Select> Entities”. In the selection window, for the first two items, select “Elements” and “By attribute”. Then select the radio button beside “Elem type num”. Then in the input box, enter the element type number for COMBIN39. Click “Apply” then “Plot”. The spring elements will be displayed. If there are not enough spring elements around the bottom bars, go to “Modeling> Delete> Elements” and from the dialogue box, select selection type as box. Select all spring elements by dragging a box and click OK. Then repeat step 31 but selecting a larger number for the tolerance value. Repeat the process until a satisfactory number of springs can be seen around the bottom bars.

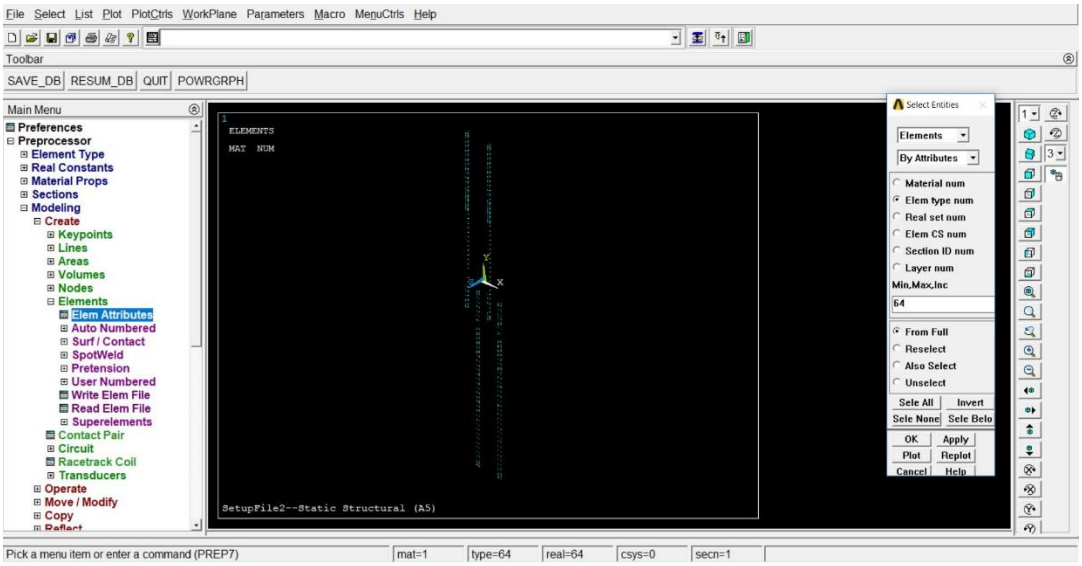

Figure D.21: Viewing only the spring elements.

Step 33. Now, select the spring elements by element type number again, but after hitting Apply, do not click plot. Then go to the Mechanical APDL Output Window. It should show the number of elements selected. Dividing the total number by 4 to get an average number of springs per rebar. Use this number to calculate the force vs. displacement curve for each element. Update the real constant for COMBIN39 elements.

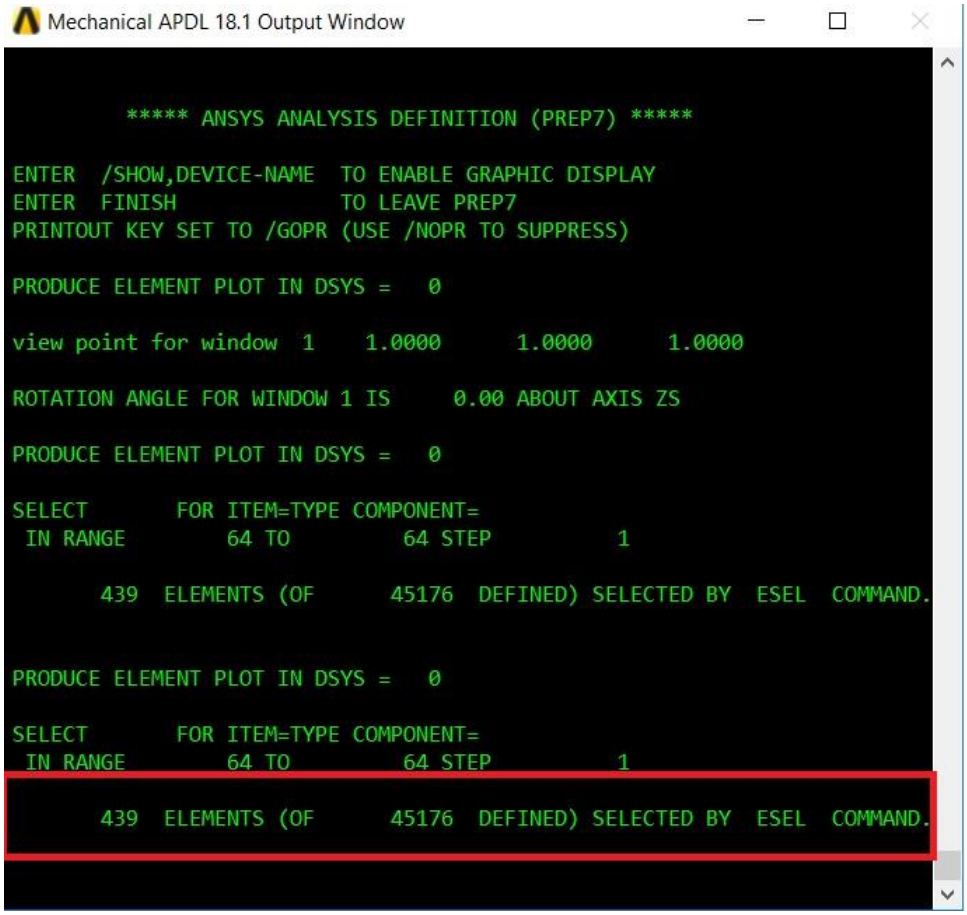

Figure D.22: Number of elements selected shown in the APDL output window.

Step 34. Go to "Solution>Analysis Type>Sol'n Controls" and set the parameters according to the following three figures.

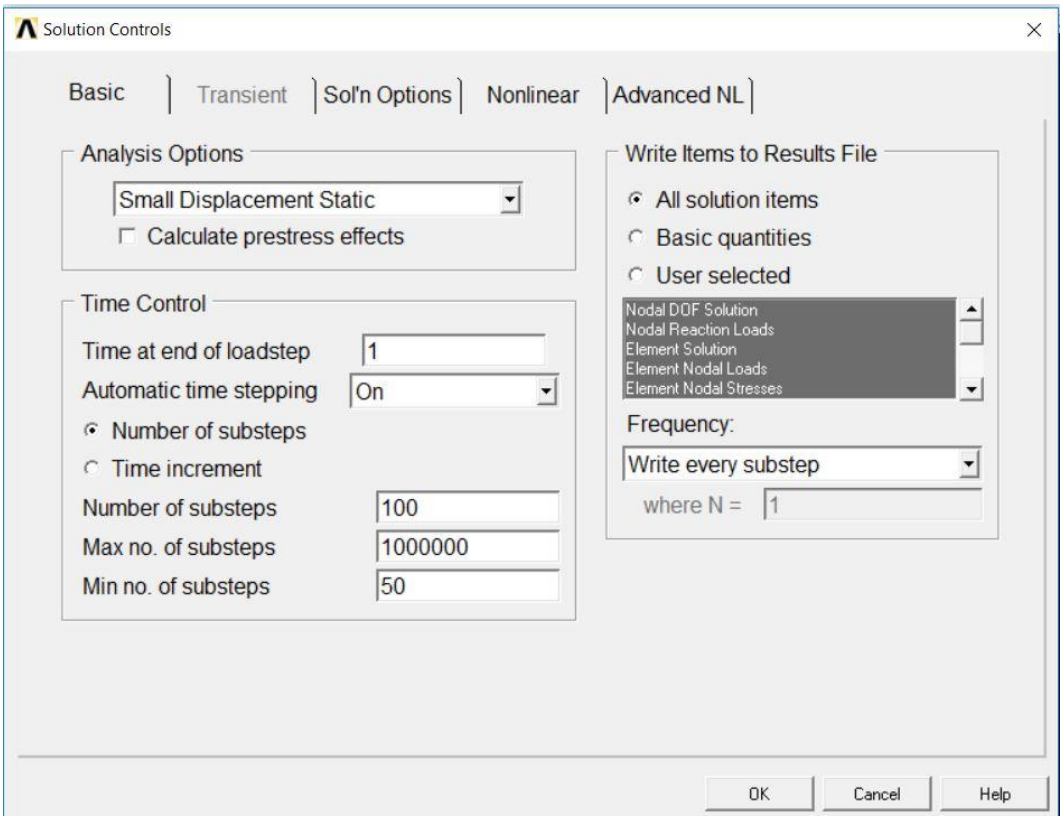
Solution Controls
Basic
Transient
Sol'n Options
Nonlinear
Advanced NL
Analysis Options
Small Displacement Static
Calculate prestress effects
Time Control
Time at end of loadstep
1
Automatic time stepping
On
Number of substeps
Time increment
Number of substeps
100
Max no. of substeps
1000000
Min no. of substeps
50
Write Items to Results File
All solution items
Basic quantities
User selected
Nodal DOF Solution
Nodal Reaction Loads
Element Solution
Element Nodal Loads
Element Nodal Stresses
Frequency:
Write every substep
where N =
1
OK
Cancel
Help

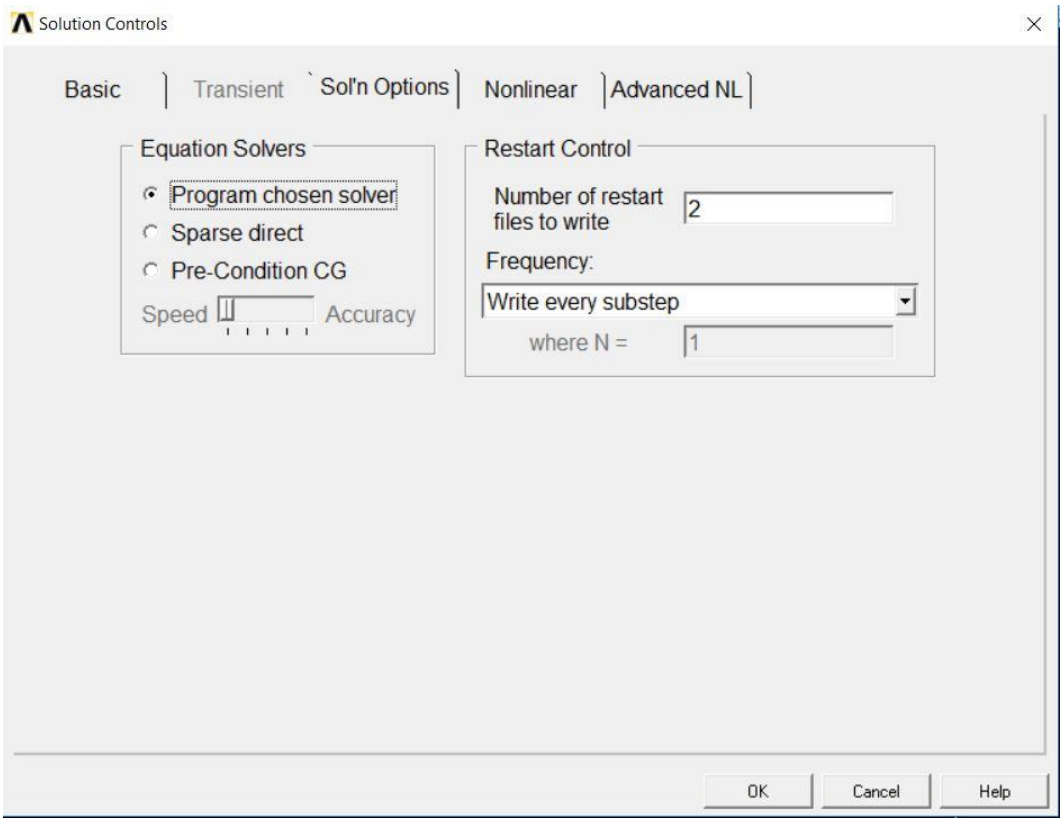
Solution Controls
Basic
Transient
Sol'n Options
Nonlinear
Advanced NL
Equation Solvers
Program chosen solver
Sparse direct
Pre-Condition CG
Speed
Accuracy
Restart Control
Number of restart files to write
2
Frequency:
Write every substep
where N =
1
OK
Cancel
Help

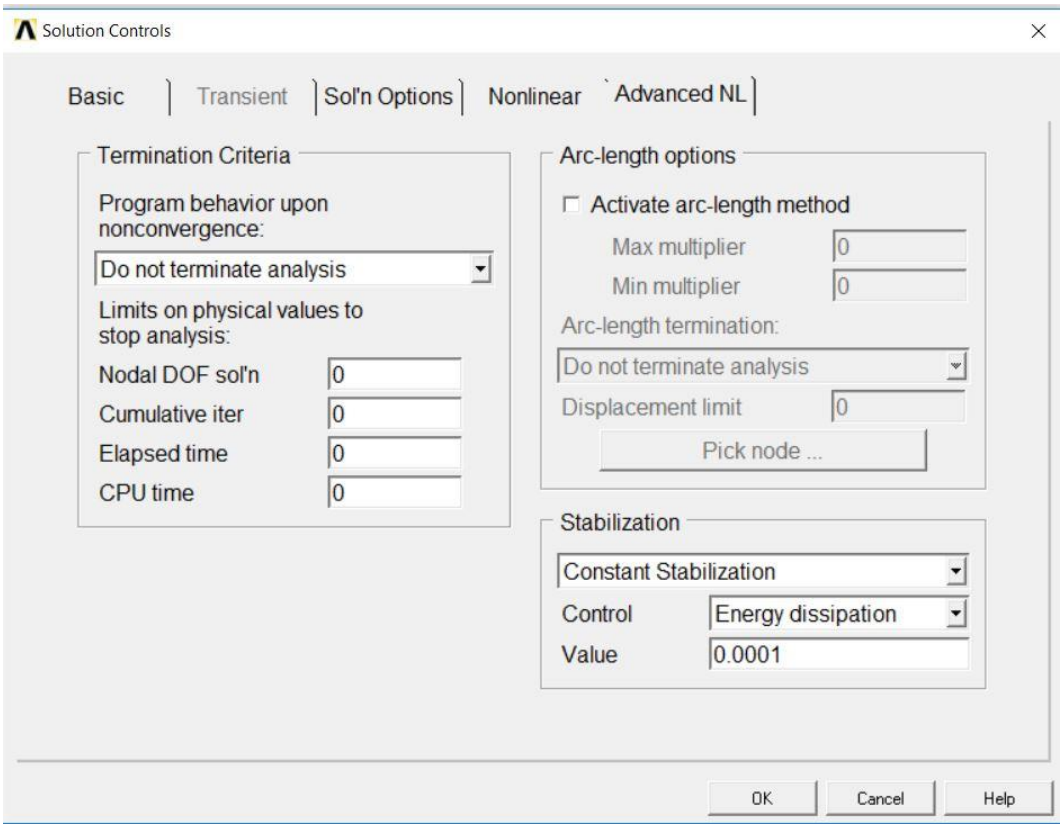

Figure D.23: Settings for the analysis.

Step 35. Click "Solution>Solve>Current LS". Click OK if any dialogue box appears. The solution process will start.

Step 36. After the solution process in APDL is over, save and close APDL. Open the Workbench project file created earlier and open "Model".

Step 37. With "Solution" selected in the outline tree, go to "Tools>Read Results File" and select the result file produced by APDL. The file should be in the folder where the APDL project was created and will have a name of "filename.rst", where "filename" is the jobname defined at the start of the APDL model.

Step 38. The results file should take a few minutes to load. After it is loaded, all the results can be obtained using the Workbench project as if it were a Workbench model.

D.3 Step by Step Modeling of Four-Point Bending Tests

Step 1. Follow steps 1 to 13 for the modeling of three-point bending. At step 14, hide the two precast bodies. Click on the "New Plane" icon at the top-left corner. In the details window, select "From face" as type. Select the top-right face of the closure pour body as "Base face". For "Transform 1 (RMB)", select "Offset Global Y". For "FD1", put a value of 7 inches. Click Generate. A new plane will be generated.

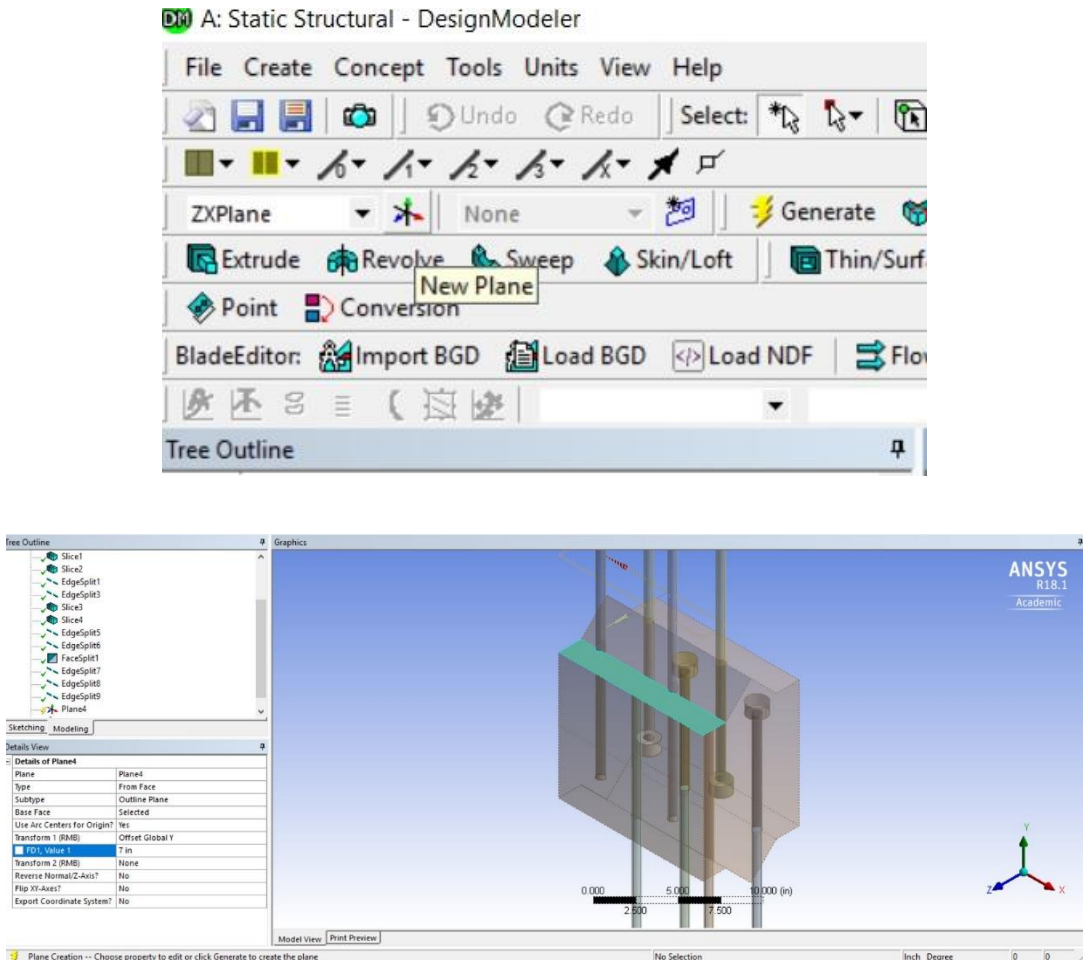

Figure D.24: Defining a new plane from a face.

Step 2. Do the same for the other side. This time, FD1 should be -7 inches. Now, there are 2 newly created planes. Now using the "Face Split" option, split the two top faces

of the two closure pour sections with the help of the two newly created planes. These two edges will be used to define the loads in step 25.

Step 3. Follow steps 15 to 38 for modeling of three-point bending tests.

D.4 APDL Code for Defining Closure Pour Material Properties

```
/PREP7
!*
ET,MATID,65
!*
KEYOPT, MATID,1,0
KEYOPT, MATID,3,0
KEYOPT, MATID,5,0
KEYOPT, MATID,6,0
KEYOPT, MATID,7,1
KEYOPT, MATID,8,1
!*
!*
MPTEMP,,,,,,,,
MPTEMP, MATID,0
MPDATA,EX, MATID,,4.4e6
MPDATA,PRXY, MATID,,0.19
TB,MISO, MATID,1,3,0
TBTEMP,0
TBPT,,3380/4.4E6,3380
TBPT,,0.0025,8450
TBPT,,0.003,8450
TB,CONC, MATID,1,9,
TBTEMP,0
TBDATA,,0.15,0.95,768,-1,,
TBDATA,,,,0.5,,,
```

D.5 APDL Code for Defining Precast Material Properties

```
/PREP7
!*
ET,MATID,65
!*
KEYOPT, MATID,1,0
KEYOPT, MATID,3,0
KEYOPT, MATID,5,0
KEYOPT, MATID,6,0
```

```
KEYOPT, MATID,7,1
KEYOPT, MATID,8,1
!*
!*
MPTEMP,,,,,,,,
MPTEMP, MATID,0
MPDATA,EX, MATID,,3.3E6
MPDATA,PRXY, MATID,,0.17
TB,MISO, MATID,1,3,0
TBTEMP,0
TBPT,,2100/4.4E6,2100
TBPT,,0.0025,5250
TBPT,,0.003,5250
TB,CONC, MATID,1,9,
TBTEMP,0
TBDATA,,0.15,0.95,614,-1,,
TBDATA,,,,0.5,,,
```